

# Effect of the Magnetospheric Plasma Interaction and Solar Illumination on Ion Sputtering of Europa's Surface Ice

Peter Addison<sup>1</sup>, Lucas Liuzzo<sup>2</sup>, and Sven Simon<sup>1</sup>

<sup>1</sup>School of Earth and Atmospheric Sciences, Georgia Institute of Technology, Atlanta, GA, USA

<sup>2</sup>Space Sciences Laboratory, University of California, Berkeley, CA, USA

## Key Points:

- Magnetic field-line draping partially protects Europa's upstream hemisphere from ion erosion, but causes substantial sputtering downstream
- If Europa's oxygen-bearing surface layer is thin compared to the ion penetration depth, maximum sputtering occurs near the upstream apex
- For a thick oxygen-bearing layer, two oxygen sputtering maxima form: one near the sub-solar point, and a weaker one near the upstream apex

---

Corresponding author: Peter Addison, [paddison6@gatech.edu](mailto:paddison6@gatech.edu)

## Abstract

For the entire ion energy range observed at Europa, we calculate spatially-resolved maps of the surface sputtering rates of  $\text{H}_2\text{O}$ ,  $\text{O}_2$ , and  $\text{H}_2$  from impacts by magnetospheric ions. We use the perturbed electromagnetic fields from a hybrid model of Europa’s plasma interaction, along with a particle-tracing tool, to calculate the trajectories of magnetospheric ions impinging onto the surface and their resultant sputtering yields. We examine how the distribution of the sputtering rates depends on the electromagnetic field perturbations, the angle between the solar radiation and the corotating plasma flow, and the thickness of the oxygen-bearing layer within Europa’s surface. Our major findings are: (a) Magnetic field-line draping partially diverts the impinging ions around Europa, reducing the sputtering rates on the upstream hemisphere, but allowing for substantial sputtering from the downstream hemisphere. In contrast, zero sputtering occurs in much of the downstream hemisphere with uniform electromagnetic fields. (b) If the oxygen-bearing surface layer is thin compared to the penetration depth of magnetospheric ions, thermal ions dominate the  $\text{O}_2$  sputtering rates, and the region of strongest sputtering is persistently located near the upstream apex. However, if the oxygen-bearing layer is thick compared to the penetration depth, energetic ions sputter the most  $\text{O}_2$ , and the location of maximum sputtering follows the sub-solar point as Europa orbits Jupiter. (c) The global production rate of  $\text{O}_2$  from Europa’s surface varies by a factor of three depending upon the moon’s orbital position, with the maximum particle release occurring when Europa’s sun-lit and upstream hemispheres coincide.

## 1 Introduction

The icy moon Europa (radius  $R_E = 1560.8$  km) is the smallest of the four Galilean moons of Jupiter, and possesses one of the youngest surfaces of any solar system object (about 50 million years, e.g., Bierhaus et al., 2009). The youth of Europa’s surface is the result of continuous resurfacing processes, such as past tectonic activity (e.g., Kattenhorn & Hurford, 2009), meteorite impacts (e.g., Schenk et al., 2007), and sputtering by magnetospheric particles (e.g., Johnson et al., 2009). Neutral particles ejected from Europa’s surface via sputtering form a dilute exosphere surrounding the moon (e.g., Hall et al., 1995; Johnson et al., 2009; Plainaki et al., 2018). Radiolysis via charged particle impacts is also hypothesized to be the source of the non-uniform coloration and brightness patterns across the moon’s surface ice (McEwen, 1986; Hendrix et al., 2011). Eu-

ropa’s differentiated structure includes a subsurface liquid water ocean (Kivelson et al., 2000), which may interact with the surface through plume activity (Roth et al., 2014; Jia et al., 2018; Arnold et al., 2019; Paganini et al., 2020).

Europa’s orbital distance of  $9.4 R_J$  (Jupiter radius  $R_J = 71,492$  km) places the moon in the giant planet’s inner magnetosphere. As such, it is exposed to a dynamic environment of strong electromagnetic fields and dense magnetospheric plasma. The  $9.6^\circ$  tilt between Jupiter’s rotational and magnetic axes causes periodic variations in the strength and direction of the Jovian magnetic field as well as the plasma density at Europa’s orbit (e.g., Kivelson et al., 1999; Seufert et al., 2011; Bagenal & Dols, 2020). This oscillation induces currents in Europa’s conducting subsurface ocean, which in turn generate a secondary, quasi-dipolar magnetic field outside the moon (Kivelson et al., 2000; Zimmer et al., 2000; Vance et al., 2021). Such an induction signal has been detected by the Galileo spacecraft during several targeted flybys of Europa (e.g., Kivelson et al., 2000).

Europa’s location within the inner magnetosphere also portends that the moon is exposed to a diverse range of plasma species. Neutral matter emitted by Europa’s volcanically active neighbor, Io, is ionized via electron impacts and photoionization (Saur et al., 2003), and transported radially outward to Europa’s orbit, forming a plasma sheet centered near the Jovian magnetic equator (e.g., Bagenal et al., 2016; Pensionerov et al., 2019). The thermal ion population in this sheet consists mainly of hydrogen, oxygen, and sulfur ions with energies of approximately 1 keV, and follows a Maxwellian distribution (Bagenal & Delamere, 2011; Bagenal & Dols, 2020; Kim et al., 2020). Since Jupiter’s rotation period is only one-eighth of Europa’s orbital period, the sub-alfvénic, (partially) corotating plasma overtakes the moon with a relative velocity of  $\approx 100$  km/s (Kivelson et al., 2009). As the magnetospheric plasma impinges onto Europa, electrons ionize neutral gas in the exosphere, creating an ionosphere that envelops the moon (Saur et al., 1998). The injection of slow-moving, newly-generated ionospheric ions into the magnetospheric flow drains momentum from the upstream plasma, causing it to slow and accumulate above the moon’s upstream face. The magnetic field, which is frozen into the plasma, piles up in this region of enhanced plasma density and drapes around the moon (e.g., Rubin et al., 2015; Arnold, Liuzzo, & Simon, 2020).

The ion population near Europa also features a high-energy component, containing ions with energies  $E$  from several keV to tens of MeV (e.g., Cooper et al., 2001; Mauk

et al., 2004; Paranicas et al., 2009; Clark et al., 2020). The high energies of these ions allow them to travel along Jupiter’s magnetic field lines all the way to the planet’s poles, where they are mirrored back toward Europa’s orbital plane. As such, energetic ions continually intercept the moon’s orbit. Europa does not possess a sufficiently dense gas envelope for collisions to protect its surface from ion irradiation (Shematovich et al., 2005; Coustenis et al., 2010). Most magnetospheric ions can penetrate directly to the surface without encountering an exospheric molecule, although recent studies by Huybrighs et al. (2020) and Addison et al. (2021) suggest that charge exchange with exospheric neutrals may partially shield the moon’s surface from low energy ( $E \leq 200$  keV) proton bombardment. However, charge exchange reactions produce energetic neutral atoms (ENAs), which may still impact and erode the surface. As such, Europa’s surface ice is continually abraded by corotating thermal ions ( $E \approx 1$  keV), fast-moving energetic ions ( $5 \text{ keV} < E < 10 \text{ MeV}$ ), and (to a minor extent) ENAs. Slow-moving ionospheric ions weather the surface, however their contribution to erosion is several orders of magnitude weaker than that of magnetospheric ions (Saur et al., 1998). The surface also faces irradiation by galactic cosmic rays, but their influx is dwarfed by magnetospheric ions in the upper reaches of the ice (first  $\sim$  tens of centimeters, Nordheim et al., 2019), the realm typically sampled by optical instruments. In addition, thermal and energetic electrons contribute to surface modification (e.g., Vorburger & Wurz, 2018; Davis et al., 2021). However, this study focuses on the irradiation of the surface by magnetospheric ions only.

Magnetospheric ion irradiation has been identified as a critical agent in the weathering of Europa’s surface (Cassidy et al., 2013; Dalton et al., 2013; Breer et al., 2019; Addison et al., 2021). The Photopolarimeter-Radiometer (PPR) aboard Galileo observed the upstream/orbital trailing hemisphere of Europa to be noticeably dark, with a bolometric albedo roughly thirty percent lower than that of the downstream hemisphere (Rathbun et al., 2010). Several studies have hypothesized that this hemispheric darkening is due to the presence of sulfur-containing compounds, which are formed when magnetospheric sulfur ions implant into surface ice (McEwen, 1986; Hendrix et al., 2011; Dalton et al., 2013). Measurements by the Galileo Near-Infrared Mapping Spectrometer (NIMS) also indicate a “bullseye” distribution of the sulfuric acid concentration on the surface, i.e., the sulfuric acid concentration maximizes near the upstream apex, and decreases with distance away from it (Carlson et al., 2005). Such a bullseye-like pattern is consistent with the spatial distribution of sulfur ion flux predicted by some models (Cassidy et al.,

2013; Dalton et al., 2013), reinforcing the idea that ion influx is the mechanism behind surface darkening.

Magnetospheric ions that impact Europa’s surface may directly eject H<sub>2</sub>O from the ice, or radiolytically dissociate H<sub>2</sub>O into H<sub>2</sub>, O<sub>2</sub>, and a number of other trace species, which can then be ejected by further particle impacts (Plainaki et al., 2013; Teolis et al., 2017; Vorburger & Wurz, 2018). The Jeans parameter, i.e., the ratio between a particle’s gravitational potential energy and its kinetic energy, is 0.25 for sputtered H<sub>2</sub> (Roth et al., 2017), while for sputtered O<sub>2</sub> and H<sub>2</sub>O it is approximately 10 (Saur et al., 1998). Therefore, O<sub>2</sub> and H<sub>2</sub>O remain gravitationally bound to Europa, while a large fraction of the sputtered H<sub>2</sub> molecules are transported outward and escape Europa’s Hill sphere, populating the neutral torus along Europa’s orbit (see, e.g., Lagg et al., 2003; Kollmann et al., 2016). This escaping hydrogen has been detected by both the Hubble Space Telescope (HST) in the form of a global H<sub>2</sub> corona (Roth et al., 2017) and by the Galileo Energetic Particles Detector (EPD, see Nénon & André, 2019). Since both O<sub>2</sub> and H<sub>2</sub>O remain gravitationally bound to Europa, molecules of both types may re-encounter Europa’s surface. The sticking coefficient (the likelihood that a molecule will re-freeze to Europa’s surface upon contact) of H<sub>2</sub>O is approximately 1, while for O<sub>2</sub> it is approximately 10<sup>−3</sup> (Eviatar et al., 1985). Refreezing therefore removes much of the sputtered H<sub>2</sub>O from the exosphere, but does not constitute a significant loss mechanism for O<sub>2</sub>. Despite this, a persistent, highly-localized H<sub>2</sub>O exosphere has recently been detected above Europa’s upstream apex (Roth, 2021), suggesting that H<sub>2</sub>O is not entirely lost to refreezing. Molecular oxygen is removed from the exosphere mainly through ionization, with a minor contribution from plasma-neutral collisions that eject molecules (Saur et al., 1998). These two loss processes, along with O<sub>2</sub> production via ion impacts and radiolysis, allow O<sub>2</sub> to maintain mass balance within a near-surface exosphere approximately 300 km in height (e.g., Vorburger & Wurz, 2018). Sputtering of neutral ice particles is therefore the main source of Europa’s predominantly O<sub>2</sub> exosphere (Plainaki et al., 2013; Teolis et al., 2017), with an additional, minor contribution from sublimation.

The amount of neutral matter produced per area and time via ion sputtering at a given surface location is dependent upon two factors: the differential ion surface flux  $j(E, \theta)$  reaching that location, i.e., how many ions of a specific energy  $E$  and incidence angle  $\theta$  hit a given surface area per unit time, and the sputtering yield  $Y(E, \theta, T)$ , i.e., how many neutral particles are released from a surface element of temperature  $T$  by each

impinging ion. The total sputtering *rate* of a given ion species,  $R$ , is the number of surface particles ejected at that location per unit area per unit time. The sputtering rate is determined by multiplying the differential ion flux  $j(E, \theta)$  with the sputtering yield  $Y(E, \theta, T)$  at each incident ion energy and impact angle, and integrating over the entire energy range and all impact angles. In sections 1.1 and 1.2, the current state of knowledge on the ion surface fluxes at Europa and sputtering yields is discussed.

### 1.1 Ion Surface Fluxes

The spatial distribution of the ion flux incident on Europa's surface has been investigated by a number of previous studies. Pospieszalska and Johnson (1989) modeled the trajectories of 30-140 keV sulfur ions near Europa and found that the surface flux of these ions maximizes near the moon's orbital trailing (upstream to the plasma flow) apex. These authors also found that sulfur ions at higher energies ( $E \geq 140$  keV), which possess a gyroradius of roughly  $0.25 R_E$ , can reach almost all locations on Europa's surface. Therefore, even the moon's downstream hemisphere is not entirely protected from ion irradiation at energies above approximately 100 keV. Cassidy et al. (2013) calculated the surface fluxes of hydrogen, oxygen, and sulfur ions from 1 keV to 10 MeV, thereby covering the energy range where Galileo detected significant ion fluxes outside of Europa's interaction region (e.g., Paranicas et al., 2009). Cassidy et al. (2013) found that the total ion flux onto Europa (taking into account all species and energies) is distributed in a bullseye-like pattern centered at the trailing hemisphere apex, consistent with the distribution of surface sulfuric acid concentration measured by the NIMS instrument (Carlson et al., 2005). Ions with energies above 100 keV were found to impact primarily Europa's polar regions, a result of high field-aligned (i.e., north-south) velocities relative to the corotation velocity. However, both Pospieszalska and Johnson (1989) and Cassidy et al. (2013) treated the electromagnetic fields near Europa as uniform, that is, the perturbations to the fields introduced by the induced dipole and the sub-Alfvénic plasma interaction were not taken into account. We note that the presence of the induced field was not known at the time of the Pospieszalska and Johnson (1989) study.

All eight targeted flybys of Europa performed by the Galileo spacecraft showed perturbations to the local magnetic field components of up to 100% of their background values (see review by Kivelson et al., 2009). Magnetometer data from several flybys (most notably E4 and E11) even revealed a local reversal in the sign of the horizontal (i.e., par-

allel to Europa’s orbital plane) field components compared to their measured upstream values. Investigations of induction at Europa (e.g., Zimmer et al., 2000; Vance et al., 2021) have shown that the induced field alone may reach a strength near the moon’s surface of approximately half ( $\approx 210$  nT) of the Jovian background field ( $\approx 400 - 450$  nT). Numerous modeling studies (e.g., Rubin et al., 2015; Arnold et al., 2019; Arnold, Liuzzo, & Simon, 2020; Harris et al., 2021) have reproduced the observed magnetic signatures by simulating the interaction between the upstream magnetospheric plasma, Europa’s exosphere, and the moon’s induced field. The draping and pileup of the magnetospheric field, as well as the non-linear coupling of the induced field to the sub-alfvénic interaction (Neubauer, 1999), significantly modify ion trajectories in Europa’s vicinity (Breer et al., 2019; Addison et al., 2021). Accurate modeling of the ion fluxes incident upon Europa’s surface therefore requires inclusion of the field perturbations generated by the plasma interaction with Europa’s exosphere and induced field.

Several recent studies have modeled the spatial distribution ion flux onto Europa while including the deformation of the local electromagnetic fields by magnetospheric plasma deflection and induction. Breer et al. (2019) used the AIKEF hybrid model (kinetic ions, fluid electrons) to compute the perturbations to the electromagnetic fields near Europa. They then calculated spatially resolved maps of the accessibility—defined as the percentage of upstream ions that reach a given surface location—of Europa’s surface to upstream magnetospheric ions. On the basis of Galileo measurements of the ion species and energies present near Europa, these authors traced  $H^+$ ,  $O^{2+}$ , and  $S^{3+}$  ions at discrete energies ranging from 1 keV to 5 MeV. To establish a “baseline” for the identification of modifications in the accessibility patterns caused by the field perturbations, they also calculated maps of the ion irradiation of Europa’s surface for uniform fields (similar to Pospieszalska and Johnson (1989) and Cassidy et al. (2013)). For the case of uniform fields, Breer et al. (2019) showed that Europa’s surface is highly accessible to upstream ions of all energies, with accessibilities near 90% in all regions except for a narrow “belt” near the moon’s equator, where the accessibility drops to 0-40% for ion energies below 1 MeV. This equatorial depletion belt results from the tendency of ions following magnetic field lines near Europa to gyrate into the moon’s surface at high northern and southern latitudes before reaching the equatorial region. At MeV energies, even the protection of Europa’s equatorial region from magnetospheric ions was found to largely

disappear, since MeV ions possess gyroradii of roughly  $1 R_E$ , and can therefore gyrate around Europa and impact any point on the surface.

However, Breer et al. (2019) also found that the draping and pileup of the magnetic field near Europa deflect a significant portion of the impinging ions around the moon, reducing the accessibility by up nearly a factor of two at almost all surface locations. At ion energies below 100 keV, only several small “islands”, located mainly on the anti-Jovian hemisphere, were found to remain accessible to more than 80% of upstream ions. Only at MeV energies does the pattern of surface accessibility become qualitatively similar to that produced with uniform electromagnetic fields, although the accessibility was still five times smaller. Even the inclusion of the induced dipole field alone was found to make the surface accessibilities five to ten times smaller at most energies. Thus, Breer et al. (2019) found the perturbations to the electromagnetic fields near Europa to be critical in modifying ion dynamics near the moon at all energies. Therefore, the plasma interaction must be taken into account by any reasonable model of ion surface fluxes.

A synodic rotation period of Jupiter at Europa is approximately ten hours, and on this time scale both the Jovian magnetic equator and the magnetospheric plasma sheet continuously sweep over the moon. Therefore, both the Jovian background field and the ambient plasma density near Europa periodically vary. Not only does this variation affect the strength and orientation of the moon’s induced secondary field, but it also continually changes the Alfvénic Mach number  $M_A$  of the upstream flow, altering the tilt of the Alfvén wings and the strength of the plasma interaction (Neubauer, 1980, 1998). This oscillation results in drastically different magnitudes and spatial distributions of ion flux onto Europa’s surface at different locations along a synodic rotation, as magnetospheric ions navigate starkly different electromagnetic field configurations. Breer et al. (2019) calculated the accessibility of Europa’s surface to magnetospheric ions for a few select sets of ambient electromagnetic field conditions, placing emphasis on the role of water vapor plumes in locally protecting the surface from ion irradiation. However, these authors did not systematically examine the evolution of these accessibility patterns as Jupiter completes a synodic rotation; only several “snapshots” along a rotation were investigated. Furthermore, their study did not quantify ion surface *fluxes* based on the energy-dependent upstream ion distributions measured by the Galileo spacecraft, but only the accessibility of Europa’s surface to upstream ions. In other words, the ion macroparticles—conglomerate particles, representative of many actual ions, but with the same mass-to-



charge ratio—in the model of Breer et al. (2019) were all weighted equally, regardless of their energy. Their approach did not take into account that, for the energetic ion distributions measured near Europa by Galileo (Paranicas et al., 2009), modeled ion macroparticles at energies in the keV regime represent *several orders of magnitude* more real-world particles than in the MeV regime. Converting surface accessibilities into realistic ion surface flux maps requires taking into account the dependence of the upstream ion distribution on ion energy and pitch angle, as observed by the Galileo EPD (Paranicas et al., 2002; N  non & Andr  , 2019). The surface fluxes from such an approach may then be applied to inform studies of surface modification and sputtering.

Building upon the model of Breer et al. (2019), Addison et al. (2021) recently constrained the magnitude and spatial distribution of ion surface flux at Europa for different sets of magnetospheric conditions encompassing an entire synodic rotation of Jupiter: namely when Europa is located at the center of the Jovian plasma sheet, as well as at maximum elongation north or south of the sheet. At each location, the AIKEF hybrid code was used to calculate the moon’s perturbed electromagnetic environment. Addison et al. (2021) then combined a particle-tracing tool with the upstream energy and pitch angle distributions of the ions, as measured by Galileo, to calculate ion surface fluxes. Their model incorporated upstream plasma densities and temperatures derived from Galileo observations (Paranicas et al., 2002; Kivelson et al., 2009; Bagenal & Delamere, 2011), as well as the latest information on energetic ion charge states obtained by the Juno spacecraft (Clark et al., 2020; Kim et al., 2020). By averaging the flux maps obtained for the three distances between Europa and the center of the Jovian plasma sheet, Addison et al. (2021) then obtained average surface flux maps of magnetospheric oxygen, sulfur and hydrogen ions over an entire synodic rotation. Their averaged flux maps consider contributions of ions from the entire energy range (5 keV up to 10 MeV) where significant ambient fluxes were observed near Europa.

The study of Addison et al. (2021) found that inclusion of the plasma interaction results in drastically different patterns of ion surface flux compared to the case of uniform electromagnetic fields. Although the total ion flux in their model still maximizes near the upstream apex, deflection of thermal ions around Europa’s Alfv  n wings was shown to reduce ion flux onto the upstream hemisphere by two orders of magnitude compared to predictions for uniform fields. Most surprisingly, the draped field geometry near the moon was found to divert thermal ions from the “edges” of the Maxwellian distri-

bution onto Europa’s polar regions, as well as onto its *downstream* hemisphere, resulting in a flux there of only one order of magnitude less than in the upstream hemisphere. Using a fluid model and considering the forces generated by local pressure gradients, Harris et al. (2021) identified a similar flow pattern in the thermal ion population near Europa. In contrast to this, without plasma currents the thermal ion fluxes are zero in large segments of the downstream hemisphere.

Addison et al. (2021) showed the surface flux pattern of energetic ions ( $E \geq 5$  keV) to be considerably modified by the plasma interaction. A large, quasi-elliptical depletion region was found to form around the upstream apex and extend approximately  $\pm 60^\circ$  in both latitude and longitude. The field draping enhances the distance that an ion traveling along a magnetic field line is within one gyroradius of the moon’s surface. This mechanism causes a significant fraction of the incoming energetic ions to gyrate into the moon’s surface at high latitudes before they can reach the upstream apex, resulting in this elliptical depletion region. This “inverted bullseye” feature is not predicted by a model that treats the fields as uniform. The results of Addison et al. (2021) therefore show that the inclusion of the sub-alfvénic plasma interaction is imperative to explain a number of observations from both in-situ spacecraft and ground-based telescope observations, such as the non-uniform surface distribution of sulfuric acid concentrations (Ligier et al., 2016), and a drop in the upstream ion flux seen during several close Galileo flybys of Europa (Paranicas et al., 2000).

## 1.2 Sputtering Yields

Once a magnetospheric ion impacts Europa’s surface, the amount of neutral matter ejected is determined by the ion’s sputtering yield  $Y(E, \theta, T)$ . Many laboratory experiments have measured sputtering yields from water ice (see reviews by Johnson (1996), Johnson et al. (2009), and references therein). Surface particles may be released from the ice at any depth to which an impinging ion penetrates ( $\approx 10^1 - 10^7 \text{ \AA}$ , e.g., Teolis et al., 2017). However, the greater the depth at which a neutral particle is ejected, the larger the chance that it will stick to another surface grain before escaping into the exosphere (Cassidy & Johnson, 2005).

For projectile ion energies below approximately 100 keV, molecules are directly ejected from the surface ice via momentum transfer (elastic) collisions (Sigmund, 1969). At higher

projectile energies, incident ions excite electrons in surface molecules, breaking covalent bonds and causing the dissociation of constituent species, thereby facilitating neutral matter release from the surface (Brown et al., 1978; Sieger et al., 1998). Laboratory data has shown that sputtering yields from water ice increase with energy in the momentum-transfer regime, then rapidly grow in the electronic excitation regime, before dropping off at extremely high projectile energies (Johnson et al., 2009). The sputtering yields of the dominant ion species at Europa (hydrogen, oxygen, and sulfur ions) therefore reach a maximum in the  $E \approx 100$  keV–5 MeV range (depending upon the projectile species), and then drop precipitously at higher energies. This non-monotonic energy dependence of the sputtering yield seen in laboratory experiments has been fit with analytical forms by, e.g., Famá et al. (2008). Their fits have shown that, due to their large masses and atomic numbers, oxygen and sulfur ions possess the greatest sputtering yields: up to 5000 neutral particles are released per incident projectile. The analysis of laboratory data by Famá et al. (2008) also revealed that ions which impact the surface at grazing angles  $\theta \approx 90^\circ$  against the surface normal sputter up to 100 times more neutral particles than ions which impact normal to the surface ( $\theta \approx 0^\circ$ ), since grazing projectiles deposit more energy at shallower depths.

In addition to projectile properties, sputtering yields also depend on the properties of the surface that is impacted. The porosity of Europa’s surface regolith may limit sputtering yields to 25% of their values measured in the laboratory using “smooth” surfaces, as particles that are initially ejected may hit and stick to other grains rather than escape into the exosphere (Cassidy & Johnson, 2005). Furthermore, sputtering yields increase monotonically with temperature (Brown et al., 1982) in the range of surface temperatures observed at Europa ( $\approx 60 - 140$  K, Spencer et al., 1999). This temperature dependence mainly affects the sputtering yields of  $O_2$ , which is radiolytically dissociated from ice within the first  $\approx 28$  Å of the surface (Teolis et al., 2005, 2017). Increased surface temperature facilitates the transformation of dissociated oxygen radicals into stable  $O_2$  (Teolis et al., 2017), which may be sputtered by subsequent projectile impacts. The surface temperature profile at Europa is determined by its orientation with respect to the Sun, as well as the thermal inertia of its surface ice. Therefore, sputtering rates may vary over the course of a European rotation as the sub-solar point moves along the equator relative to the upstream apex, where the influx of magnetospheric ions peaks (Addison et al., 2021).

The effect of solar orientation relative to the plasma flow direction on sputtering rates at Europa has been studied by Plainaki et al. (2013), who modeled the generation of the exosphere at four different locations of the moon relative to the Sun: with the sub-solar point located at the sub-Jovian, downstream, anti-Jovian, and upstream apices (0:00, 6:00, 12:00, 18:00 local time (LT), respectively). These authors characterized the ion influx pattern with an analytical profile, which combined a spatially homogeneous component—representing an assumed isotropic influx of energetic ions—with a bullseye-like enhancement centered at the upstream apex and suggested to be representative of the thermal ion contribution. They then modeled the sputtering rates and subsequent exospheric dynamics for different orientations between the incoming solar radiation and the corotational plasma flow. Plainaki et al. (2013) found that the exospheric column density is greater by a factor of three when the sub-solar point and upstream apex are colocated, compared to when the sub-solar point is located at the downstream apex. These authors also suggested that the region where the largest amount of neutral matter is sputtered follows the sub-solar point as it moves across Europa’s surface, and does not remain fixed at the upstream apex. However, laboratory measurements indicate that  $\text{O}_2$  sputtering from an icy surface has a delayed response to changes in surface temperature (Teolis et al., 2005) as surface radicals require time to accumulate into  $\text{O}_2$ . Since this delay is potentially comparable to a European day, the sputtering rate of  $\text{O}_2$  may not have time to adjust to changes in surface temperature following Europa’s orbital motion (Teolis et al., 2017).

In contrast to Plainaki et al. (2013)—who used an analytical profile to describe ion surface flux—the study of Cassidy et al. (2013) combined *modeled* ion surface fluxes, fits to laboratory data of sputtering yields, and a thermophysical surface temperature model (Spencer et al., 1989) to calculate the spatial distribution of ion sputtering rates at Europa. Adopting the notion of a delayed  $\text{O}_2$  sputtering response to changes in surface temperature (Teolis et al., 2005), Cassidy et al. (2013) applied a diurnally-averaged (i.e., averaged over a full orbit) profile of Europa’s surface temperature. These authors found that Europa’s surface is preferentially sputtered on the upstream hemisphere, with the neutral production in that region exceeding that of the downstream hemisphere by a factor of three. Neutral particles ejected by thermal oxygen ions and energetic sulfur ions were found to dominate the sputtering rate. The strong contribution of the thermal oxygen ions in the model of Cassidy et al. (2013) arose from their high surface flux, which

was found to exceed that of any other species by roughly an order of magnitude. We note that the modeled surface fluxes of Cassidy et al. (2013) are not consistent with those of Addison et al. (2021), who found that—when field line draping is taken into account—magnetospheric hydrogen (*not* oxygen) makes the largest contribution of any ion species to surface flux. The large contribution of energetic sulfur ions to the sputtering rate calculated by Cassidy et al. (2013) arose mainly from their respective sputtering yield, which is roughly a factor of five greater than that of oxygen in the energetic regime, and orders of magnitude greater than the sputtering yield of hydrogen at all energies. Cassidy et al. (2013) found that nearly zero  $O_2$  is produced on the downstream hemisphere, since in their model  $O_2$  is sputtered almost entirely by the thermal heavy ions. Under the assumption of uniform fields, these ions only precipitate onto the upstream hemisphere. Vorburger and Wurz (2018) utilized a spatially homogeneous magnetospheric ion flux across Europa’s surface in their calculation of sputtering rates, although they did approximate the deflection of thermal upstream ions in the perturbed fields near Europa by uniformly reducing their respective flux by a factor of 5. These authors confirmed that thermal oxygen and energetic sulfur ions are the most significant contributors to ion sputtering at Europa.

Although Plainaki et al. (2013), Cassidy et al. (2013), and Vorburger and Wurz (2018) have modeled neutral production via magnetospheric ion sputtering at Europa, no study to date has investigated how the spatial distribution of surface sputtering is modified when a realistic model of incident ion deflection in the draped electromagnetic fields is taken into account. The ion-tracing model of Cassidy et al. (2013) assumed the fields to be spatially uniform, an assumption also implicit in the ion influx pattern utilized by Plainaki et al. (2013). Vorburger and Wurz (2018) treated the ion influx as uniform at all points on Europa’s surface.

However, (Addison et al., 2021) found not only that the shielding of Europa’s upstream hemisphere from magnetospheric ion impacts due to field line draping is orders of magnitude stronger than assumed by Vorburger and Wurz (2018), but that it varies strongly with surface latitude and longitude. In addition, Addison et al. (2021) demonstrated that the downstream hemisphere of Europa receives only an order of magnitude less thermal ion flux than the upstream hemisphere. They also showed that, in draped fields, the influx of energetic ions *minimizes* near the upstream apex, exactly opposite to what is predicted for uniform fields. None of the available sputtering rate models take

into account these important aspects of ion precipitation onto Europa. Therefore, ion sputtering rates at Europa must be reexamined with the influence of the field perturbations included.

This study is the first to model the sputtering of Europa’s surface ice via magnetospheric ion impacts while incorporating a realistic picture of the field perturbations generated by the moon’s sub-alfvénic plasma interaction. We use the AIKEF hybrid model (e.g., Arnold et al., 2019; Arnold, Liuzzo, & Simon, 2020; Arnold, Simon, & Liuzzo, 2020) to calculate the perturbations to Europa’s local electromagnetic environment. The electromagnetic fields from AIKEF are combined with the GENTOO particle-tracing tool (e.g., Addison et al., 2021) to calculate the trajectories of magnetospheric ions in Europa’s perturbed electromagnetic environment, from the thermal energy regime up to 10 MeV. We then use established fits to laboratory data of ion sputtering yields to obtain spatially resolved maps of ion sputtering rates across Europa’s surface. We examine the influence of projectile species, energy, incidence angle, as well as the orientation of the Sun relative to the plasma flow direction and the electromagnetic field perturbations on surface sputtering rates.

A description of the AIKEF and GENTOO models, as well as all input parameters, is provided in section 2. The modeled electromagnetic field configuration, as calculated by the AIKEF model, is presented in section 3.1. The corresponding modeled ion surface fluxes from GENTOO along with our modeled H<sub>2</sub>O sputtering rate maps for uniform and perturbed fields are presented in 3.2. In section 3.3 we calculate maps of the O<sub>2</sub> and H<sub>2</sub> sputtering rates, while examining the role of Europa’s orbital position and the thickness of the oxygen-bearing surface layer in modifying O<sub>2</sub> sputtering. The paper concludes with a summary of our main findings in section 4.

## 2 Model Description

We use a multifaceted approach in order to calculate maps of the magnetospheric ion sputtering rates at Europa. First, we model the perturbed electromagnetic environment near the moon using the AIKEF hybrid code. The AIKEF model has been extensively applied to Europa in five preceding publications (Arnold et al., 2019; Arnold, Liuzzo, & Simon, 2020; Arnold, Simon, & Liuzzo, 2020; Breer et al., 2019; Addison et al., 2021), as well as the Jovian moon Callisto (Liuzzo et al., 2015, 2016, 2017, 2018, 2019a,

2019b). In addition, AIKEF has been used to study plasma interactions at the terrestrial Moon (Wiehle et al., 2011; Liuzzo, Poppe, et al., 2021), the Saturnian moons Titan (e.g., Regoli et al., 2016; Feyerabend et al., 2015, 2016), Tethys (Simon et al., 2009), Rhea (Simon et al., 2012), and Dione (Krupp et al., 2020), as well as Neptune’s moon Triton (Liuzzo, Paty, et al., 2021; Simon et al., 2022).

Secondly, we calculate the spatial distribution of ion flux onto Europa’s surface with the GENTOO particle tracing code, which solves the equations of motion for ions moving through the draped fields near Europa. GENTOO has been applied to Europa in two preceding studies (Breer et al., 2019; Addison et al., 2021), as well as to Callisto (Liuzzo et al., 2019a, 2019b), and Ganymede (Liuzzo et al., 2020). Finally, we combine our modeled ion surface flux patterns with empirical models of the sputtering yields from water ice (Johnson et al., 2004; Famá et al., 2008; Teolis et al., 2017), along with a thermophysical model for Europa’s surface temperature profile (Spencer et al., 1989, 1999). In this way, we calculate spatially resolved maps of the surface sputtering rate at Europa. The AIKEF and GENTOO models have been extensively described in our previous publications. We therefore provide only a brief discussion of these two models here, and refer the reader to these prior publications for more information.

## 2.1 Model of Europa’s Electromagnetic Environment

To calculate the three-dimensional structure of the perturbed magnetospheric environment near Europa, we apply the AIKEF hybrid model (kinetic ions, fluid electrons) originally developed by Müller et al. (2011). Unlike a single-fluid MHD model (e.g., Kabin et al., 1999), the hybrid approach is able to capture the dynamics of individual ion macroparticles, some of which possess velocity vectors far from the peak of the Maxwellian upstream distribution. Such ions impinge onto Europa along highly inclined trajectories (with respect to the corotation direction) and substantially contribute to the irradiation of the moon’s polar caps and downstream hemisphere (Addison et al., 2021). AIKEF has achieved excellent quantitative agreement with the magnetic field signatures measured near Europa during the E26 flyby of Galileo (Arnold et al., 2019), as well as plasma and magnetic field observations from several Callisto flybys (Liuzzo et al., 2015, 2016, 2017). Thus, AIKEF is highly suited for our study of magnetospheric ion sputtering of Europa’s surface.

Throughout this paper we will use the Cartesian, Europa-centered “EPhIO” coordinate system. In this system, the  $x$  axis points in the direction of corotation, the  $z$  axis points northward (i.e., parallel to Jupiter’s spin axis), and the  $y$  axis completes the right-handed system, pointing toward the giant planet. The basis vectors along these three axes are denoted  $\hat{\mathbf{x}}$ ,  $\hat{\mathbf{y}}$ , and  $\hat{\mathbf{z}}$ , respectively. In agreement with Galileo plasma observations (e.g., Kivelson et al., 2009; Bagenal et al., 2015; Bagenal & Dols, 2020), for the AIKEF model we assume the corotating, thermal plasma to consist of a singly-charged, composite species of mass  $m_0 = 18.5$  amu, with ion and electron temperatures  $k_B T_0 = 100$  eV, and bulk velocity  $\mathbf{u}_0 = 100$  km/s  $\hat{\mathbf{x}}$ . Galileo Plasma Subsystem (PLS) measurements have also shown the bulk plasma velocity to have radial (i.e., in the  $\pm y$  direction) and polar (i.e., in the  $\pm z$  direction) components near Europa’s orbit (Bagenal et al., 2016). However, these components are, at most,  $\approx 5\%$  of the azimuthal (corotational, i.e., along  $+x$ ) component. The radial and polar components also have been observed to have different directions during different crossings of Europa’s orbit, revealing that there is no consistent behavior of the radial or polar flow components near Europa (see Figure 7b of Bagenal et al., 2016). However, such weak radial and polar plasma velocity components would only cause a very subtle rotation of our surface flux patterns around the  $z$  and  $y$  axes, respectively, and as such we do not consider them here.

Europa’s exosphere is treated as consisting entirely of  $\text{O}_2$  (Plainaki et al., 2018), with a scale height of 100 km (Arnold et al., 2019; Arnold, Liuzzo, & Simon, 2020). Similar to Rubin et al. (2015), Arnold et al. (2019), and Harris et al. (2021), the exosphere in our model possesses an upstream-downstream asymmetry. In the moon’s orbital leading (downstream) hemisphere ( $x > 0$ ), the exospheric density depends only on the radial distance to the surface and includes no latitudinal or longitudinal variations. Above the moon’s orbital trailing (upstream) hemisphere, the exospheric density profile is axisymmetric around the  $x$  axis and decreases with radial distance to the surface. However, it also drops with angular distance from the moon’s upstream apex (see equation (2) of Arnold, Liuzzo, & Simon, 2020). The exosphere is mainly ionized through electron impacts, which dominate the ionization rate at Europa by over an order of magnitude compared to photoionization (Saur et al., 1998). The AIKEF simulation domain covers the volume bounded by  $-9R_E \leq x \leq 21R_E$ ,  $-10R_E \leq y \leq 10R_E$ , and  $-30R_E \leq z \leq 30R_E$ . In order to achieve a high resolution near the moon, AIKEF uses a hier-



archical Cartesian grid, with a cell size of  $0.02 R_E$  for the domain  $|x|, |y|, |z| \leq 1.5 R_E$ ,  
 $0.04 R_E$  for  $1.5 R_E < |x|, |y|, |z| \leq 3 R_E$ , and  $0.08 R_E$  for  $|x|, |y|, |z| > 3 R_E$ .

While the southward ( $B_{0,z} < 0$ ) component of the Jovian background magnetic field  $\mathbf{B}_0$  near Europa remains nearly constant as the plasma sheet sweeps over the moon (Kivelson et al., 1999), the  $B_{0,x}$  and  $B_{0,y}$  components exhibit oscillations in their strength and orientation on the scales of 20% and 50% of the background field magnitude, respectively (e.g., Schilling et al., 2007). Sweepback of the magnetic field lines within the plasma sheet causes the magnetic field to bulge toward upstream (Khurana & Kivelson, 1993). Therefore, the  $B_{0,x}$  component oscillates near Europa as the center of the sheet passes above and below the moon. The oscillation in the  $B_{0,y}$  component arises from Europa's excursions away from Jupiter's magnetic equator. North of the magnetic equator, the Jovian magnetic field lines point away from Jupiter (i.e., in the  $-y$  direction), whereas south of the magnetic equator the field lines point toward Jupiter ( $+y$  direction). Since the plasma number density within the sheet follows a Gaussian profile with distance to the sheet's center (Hill & Michel, 1976; Bagenal & Delamere, 2011), the thermal plasma impinging onto Europa periodically varies in density over a synodic rotation. The plasma density is maximized at the center of the sheet, while at maximum elongation north or south the plasma is more dilute by a factor of  $\sim 5$  (Bagenal & Delamere, 2011; Roth et al., 2014). Data from the Galileo PLS show no significant variation in plasma sheet density at Europa's orbit with local time (see Figure 1 of Bagenal & Delamere, 2011). The magnetopause of Jupiter is located more than  $40 R_J$  outside of Europa's orbit, so the plasma density at Europa is not significantly affected by the moon's orbital position with respect to the magnetopause. For this reason, the empirical models of the plasma density along Europa's orbit provided by, e.g., Bagenal et al. (2015), include only dependencies on the radial distance to Jupiter and vertical distance to the center of the sheet, but not on local time. The number density of the thermal plasma within the sheet does exhibit a local time dependence. However, this dependence becomes important only at radial distances far outside the orbit of Europa (Bagenal et al., 2016).

Addison et al. (2021) calculated the structure of the perturbed electromagnetic fields near Europa at three equally-spaced points in time along a synodic rotation, namely when the moon is located at (1) the center, (2) maximum elongation north, and (3) maximum elongation south of the plasma sheet. They then determined the spatial distribution of magnetospheric ion flux onto Europa's surface at each of these three locations. Finally,

Addison et al. (2021) averaged these three flux maps across a synodic rotation, and compared the resulting map to the spatial distribution of ion flux calculated at the center of the plasma sheet (case (1)). These authors showed that the surface flux patterns from both scenarios possessed significant similarities. In both cases, the distribution of the total flux onto the surface was dominated by the contribution of the thermal ions, which were able to reach nearly every location on the surface, with the highest irradiation occurring near the upstream apex (see Figures 4(g) and 8(f) of Addison et al., 2021). Only in a narrow band near Europa’s geographic equator was the thermal ion flux reduced by 3–4 orders of magnitude compared to the poles or the upstream apex. The surface flux pattern of energetic ions was also nearly identical in both scenarios (Figures 4(h) and 8(e), Addison et al., 2021). While the spatial distribution of energetic ion influx was more uniform across the surface than that of the thermal ions, the energetic ions were found to preferentially impact Europa’s high-latitude regions. In both cases, a circular depletion in the energetic ion flux by roughly an order of magnitude was identified near Europa’s upstream apex. At no location on Europa’s surface was the ion flux averaged over an entire synodic rotation different by more than a factor of five from the ion flux calculated near the center of the plasma sheet. Addison et al. (2021) therefore concluded that the distribution of ion surface flux onto Europa near the center of the plasma sheet is an excellent approximation of the averaged ion flux pattern onto the moon over an entire synodic rotation.

Therefore, our study of surface sputtering is based on a single configuration of the ambient environment near Europa, namely one that is representative of the magnetospheric conditions near the center of the plasma sheet. The Jovian background magnetic field  $\mathbf{B}_0$  for this model setup is determined by averaging the time-dependent magnetospheric field at Europa’s position (given in equation (17) of Schilling et al., 2007) over an entire synodic period, which yields a background magnetic field of  $\mathbf{B}_0 = -410 \text{ nT } \hat{\mathbf{z}}$ . We note that, with such a purely southward magnetic field, the induced dipole moment at Europa disappears (Zimmer et al., 2000). We set the upstream plasma density to  $n_0 = 200 \text{ cm}^{-3}$ , the same value utilized by Addison et al. (2021) to simulate Europa’s conditions near the center of the plasma sheet. This value is in agreement with the upstream plasma density near the center of the plasma sheet as measured by the Galileo Plasma Wave Subsystem (PWS), see Roth et al. (2014). Such a density is also approximately in the middle of the range of densities derived by Bagenal et al. (2015), based upon com-

prehensive analysis of PWS data from Europa’s orbit. The Alfvén speed  $v_{A,0} = \frac{|\mathbf{B}_0|}{\sqrt{\mu_0 n_0 m_0}}$  in this configuration is 147 km/s, and the Alfvénic Mach number of the upstream plasma  $M_{A,0} = \frac{|\mathbf{u}_0|}{v_{A,0}}$  is approximately 0.68. The choice of this single electromagnetic field configuration facilitates the analysis of the influence of other important variables on surface sputtering rates. The role of factors such as the impact angles of impinging ions and the time-varying surface temperature profile can be studied in isolation from the changing electromagnetic fields.

## 2.2 Model of Magnetospheric Ion Surface Flux

To calculate the spatial distribution of the magnetospheric ion flux onto Europa’s surface, we use the GENTOO particle-tracing code (Liuzzo et al., 2019a, 2019b; Addison et al., 2021). GENTOO calculates the trajectories of individual macroparticles when moving through the perturbed electromagnetic fields from AIKEF. The GENTOO model utilizes a backtracing approach, that is, ion macroparticles are initialized on a grid across Europa’s surface (which is equidistant in latitude and longitude) and traced *backwards* in time (model time step  $\Delta t < 0$ ). At each grid point on the surface, particles are launched at equal angular increments across a half-sphere in velocity space, thereby encompassing all possible incident velocity vectors. Backtraced macroparticles whose trajectories re-intersect Europa’s surface after launch are deleted from the simulation. In a forward-tracing approach, such an ion would have to pass through Europa’s solid body in order to reach its starting location on the moon’s surface. Macroparticles whose trajectories do not re-encounter Europa’s surface, but reach the unperturbed magnetospheric environment, are considered to have “allowed” trajectories. Since the bounce times of magnetospheric ions are larger than the convection time of the plasma through Europa’s interaction region, an ion with an allowed trajectory cannot make a second attempt to impact Europa’s surface and become forbidden (Breer et al., 2019; Addison et al., 2021). In the forward-tracing picture, allowed particles are able to precipitate from Jupiter’s magnetosphere onto Europa’s surface, and thus contribute to surface flux.

We initialize ions on Europa’s surface at discrete energies ranging from  $E = \frac{1}{2}m(u_0 - v_{th})^2$  to  $E = 10$  MeV. Here  $m$  is the mass of each ion,  $u_0 = |\mathbf{u}_0|$  denotes the corotation speed, and  $v_{th} = \sqrt{2k_B T/m}$  (where  $k_B T$ : ion temperature) is the thermal speed of the respective ion species. We choose intermediate energies at  $E = \frac{1}{2}mu_0^2$ ,  $\frac{1}{2}m(u_0 + v_{th})^2$ , 5 keV, 10 keV, 50 keV, 100 keV, 500 keV, 1 MeV, and 5 MeV. The three lowest

energies allow adequate coverage of the thermal ion regime, where the upstream distribution changes rapidly as a function of energy (see Figure 2 of Addison et al., 2021). In agreement with, e.g., Mauk et al. (2004), ions traced by the GENTOO model are considered test particles, that is, they do not alter their local electromagnetic environment.

We calculate the trajectories of thermal and energetic sulfur, oxygen, and hydrogen ions, the dominant ion species near Europa as measured by the Galileo and Juno spacecraft (Cooper et al., 2001; Mauk et al., 2004; Kim et al., 2020; Clark et al., 2020). While the surface flux of the thermal plasma could in principle be calculated with the AIKEF hybrid code, this approach would yield maps with a four times lower resolution than the GENTOO model. The currents carried by the thermal ions (and their influence on the electromagnetic fields) are already taken into account in the AIKEF model and in the resulting field cubes provided to GENTOO. Therefore, the feedback of the thermal ions onto the fields does not need to be taken into account (a second time) in GENTOO. Each ion with an allowed trajectory in GENTOO possesses a counterpart within the framework of the hybrid model. Similar to Addison et al. (2021), the thermal plasma is modeled as consisting of  $H^+$ ,  $O^+$ , and  $S^{2+}$ , while the energetic plasma is modeled as consisting of  $H^+$ ,  $O^{2+}$ , and  $S^{3+}$ . This approach is in agreement with data on charge states gathered by the Juno spacecraft (Kim et al., 2020; Clark et al., 2020). The thermal hydrogen has a temperature  $k_B T_H = 20$  eV (Paterson et al., 1999; Bagenal et al., 2015), while the thermal oxygen and sulfur ions have a temperature of  $k_B T_{O,S} = 100$  eV (Kivelson et al., 2009; Bagenal et al., 2015). Thus, the thermal velocities of the three ion species read  $v_{th,H^+} = 63$  km/s,  $v_{th,O^+} = 34$  km/s, and  $v_{th,S^{2+}} = 24$  km/s for hydrogen, oxygen, and sulfur ions, respectively. The total thermal plasma density of  $n_0 = 200$  cm $^{-3}$  is divided amongst the three species (hydrogen, oxygen, and sulfur) using mixing ratios derived by Bagenal et al. (2015). The resulting densities of thermal sulfur, oxygen, and hydrogen ions are 112 cm $^{-3}$ , 60 cm $^{-3}$ , and 28 cm $^{-3}$ , respectively (Addison et al., 2021).

Once a backtraced ion macroparticle of a given energy with an “allowed” trajectory escapes into the ambient magnetospheric plasma, its contribution to the surface flux is calculated from measured upstream distributions. To do this, GENTOO invokes Liouville’s Theorem, which states that, in the absence of collisions or other loss/production processes, the phase space density is conserved along each ion’s trajectory. This allows the flux represented by an ion macroparticle in the upstream plasma to be related to the

flux it carries onto Europa’s surface. The energetic ion distributions outside of Europa’s local interaction region are shaped by a multitude of magnetospheric processes, such as radial transport of charged particles within the Jovian magnetosphere and dissociation of sulfur dioxide from Io’s volcanoes. To calculate the surface flux represented by each backtraced particle in GENTOO, we apply the ion distributions observed by Galileo in the vicinity of Europa’s interaction region. In this way, we ensure that all of the above processes are properly accounted for when modeling ion precipitation onto Europa. Details of this procedure are discussed in section 2.2 of Addison et al. (2021). A detailed justification for the applicability of Liouville’s Theorem at Europa is also provided in section 2.2 of Addison et al. (2021).

We utilize a drifting Maxwellian upstream distribution to calculate the surface flux of the (thermal) corotating plasma. The upstream energy distributions of energetic ions used in our model are a fit to EPD data taken during the E12 flyby of Galileo (Paranicas et al., 2002), which occurred when the moon was located near the center of the Jovian plasma sheet (see Figure 2 of Addison et al., 2021). The energetic ion distributions measured by the Galileo spacecraft changed by less than an order of magnitude as a result of Europa’s variable proximity to the center of the plasma sheet. Thus, applying the E12 distribution in our model setups does not introduce any significant uncertainties into our results. While Mauk et al. (2004) suggest the pitch angle distribution (PAD) of energetic ions near Europa to be isotropic to within 25%, subsequent analysis by Kollmann et al. (2016) and N  non and Andr   (2019) has revealed that the energetic ion PAD may in fact be “pancake-shaped”, with a depletion of particles possessing pitch angles near 0  . However, for this study we assume the PAD of the energetic ions near Europa to be isotropic, as Addison et al. (2021) found that the inclusion of an anisotropic PAD has only a minimal, quantitative effect on the surface flux pattern. These authors showed that inclusion of a pancake-shaped PAD causes a discernible reduction of the surface fluxes only in the MeV regime, where the energetic ion upstream distribution is only sparsely populated (see Figure 2 of Addison et al., 2021). At each latitude  $\lambda$  and longitude  $\phi$  point on the GENTOO grid, the differential flux  $dJ(E, \lambda, \phi)$  is calculated by summing the flux contributions of each macroparticle of a given energy with an allowed trajectory which was launched from that point.

We do not consider charge exchange reactions between magnetospheric ions and exospheric neutrals. Addison et al. (2021) found that these reactions only affect the sur-

face flux of protons with energies below  $\sim 50$  keV, which have negligible sputtering yields (Johnson et al. (2009) and section 2.3 of this study).

### 2.3 Sputtering Yields of Magnetospheric Ions

Based upon laboratory experiments, several empirical models have been developed for the sputtering yields  $Y$  of ions impinging onto water ice (e.g., Famá et al., 2008; Johnson et al., 2009; Teolis et al., 2017). Sputtering yields depend upon projectile species, energy, and impact angle, as well as the temperature and composition of the surface. Different surface species may be sputtered in varying amounts based upon the extent to which dissociative chemical processes have caused different molecules to accumulate in layers close to the surface. Each of the available sputtering yield models (e.g., Famá et al., 2008; Johnson et al., 2009; Teolis et al., 2017) matches laboratory data best only in a specific projectile energy window, or for a certain sputtered species. Therefore, calculation of sputtering rates across the range of incident magnetospheric ion energies observed at Europa requires a combination of yields from several models. Sputtering yields are expressed in units of molecules released per incident particle. In sections 2.3.1 and 2.3.2 we describe our approach to calculate the surface sputtering rates of  $\text{H}_2\text{O}$ ,  $\text{O}_2$ , and  $\text{H}_2$  at Europa from the surface flux maps of magnetospheric ions provided by GENTOO.

#### 2.3.1 Sputtering Yields of $\text{H}_2\text{O}$

Europa's surface consists primarily of water ice, which may be chemically decomposed into constituent atoms via ion and electron impacts (Bar-Nun et al., 1985; Johnson et al., 2005). However, intact  $\text{H}_2\text{O}$  may be directly sputtered from the surface prior to any chemical decomposition. Data on sputtering yields generated by laboratory experiments has been fit with analytical forms by both Famá et al. (2008) and Johnson et al. (2009). Cassidy et al. (2013) showed that the model of Famá et al. (2008) matches the laboratory data for projectile energies below  $E \approx 100$  keV, while that of Johnson et al. (2009) matches the data more closely above 100 keV. Since Europa's regolith is approximately 1 m deep (Carlson et al., 2009), water ice is present well beyond the depth to which a magnetospheric ion may penetrate ( $\approx 1$  mm at most, Teolis et al., 2017). As such, the source of sputterable  $\text{H}_2\text{O}$  may be considered unlimited on short time scales. Over geologic timescales, sputtering may locally lead to lowered water ice concentrations (e.g., Ligier et al., 2016), gradually reducing  $\text{H}_2\text{O}$  yields from areas of consistently high

bombardment. However, quantitative constraints on this thinning of the ice layer are yet to be determined through observations or modeling.

The sputtering yields of H<sub>2</sub>O molecules are independent of surface temperature below 140 K (Baragiola et al., 2003), which is approximately the maximum surface temperature at Europa (Spencer et al., 1999). Hence, for the calculation of H<sub>2</sub>O sputtering yields, we can omit the temperature-dependent term in the yield expressions of both Famá et al. (2008) and Johnson et al. (2009). The H<sub>2</sub>O sputtering yields in our model are therefore given by

$$Y_{\text{H}_2\text{O}}(m, Z, E, \theta) = \begin{cases} \{A(m) S_n(m, Z, E) + B(Z) S_e^2(m, Z, E)\} \cos^{-f(m)}(\theta) & ; \quad E \leq E_T(m, Z) \\ \left\{ \left[ C_1 \left( \frac{v}{Z^{\frac{1}{3}}} \right)^{C_2} \right]^{-1} + \left[ D_1 \left( \frac{v}{Z^{\frac{1}{3}}} \right)^{D_2} \right]^{-1} \right\}^{-1} \cos^{-f(m)}(\theta) & ; \quad E > E_T(m, Z) \end{cases}, \quad (1)$$

where the top equation is that of Famá et al. (2008), the bottom equation is from Johnson et al. (2009), and  $E_T(m, Z)$  is a “transition energy” at which we switch between the two models (see discussion below). The mass, atomic number, and incidence angle (measured against the local surface normal) of the projectile ion are given by  $m$ ,  $Z$  and  $\theta$ , respectively, while  $v$  is the velocity of the particle divided by  $2.19 \times 10^6$  m/s (Johnson et al., 2009). The factors  $A(m)$ ,  $B(Z)$ , and  $f(m)$  are functions of projectile mass and atomic number and are given by Famá et al. (2008), while the constants  $C_1 = 4.2$ ,  $C_2 = 2.16$ ,  $D_1 = 11.22$ , and  $D_2 = -2.24$  do *not* depend on projectile species and are provided by Johnson et al. (2009). The factor  $f(m)$  controls the sensitivity of  $Y$  for each species to varying incidence angles, and reads  $f(m) = 1.3$ ,  $f(m) = 1.66$ ,  $f(m) = 1.75$  for hydrogen, oxygen, and sulfur ions, respectively. In addition, the yields calculated from equation (1) are subsequently multiplied by a factor of 0.3 to account for the sticking of ejected H<sub>2</sub>O within Europa’s surface regolith (Cassidy & Johnson, 2005; Cassidy et al., 2008; Teolis et al., 2017). A similar combination of sputtering yield models has been implemented by, e.g., Cassidy et al. (2013) and Vorburger and Wurz (2018) in order to study exospheric generation at Europa.

Cassidy et al. (2013) suggested that the a suitable fit to laboratory data on sputtering yields can be accomplished by transitioning from the model of Famá et al. (2008) to that of Johnson et al. (2009) at  $E \approx 100$  keV. However, such a procedure results in discontinuities of the sputtering yield profiles of all three ion species. Attempting to avoid such jumps in the sputtering yield profiles, we define a transition energy,  $E_T(m, Z)$ , for

each species at which we switch from the yield profiles of Famá et al. (2008) at  $E \leq E_T(m, Z)$  to Johnson et al. (2009) at  $E > E_T(m, Z)$ . We set the transition energy of hydrogen and sulfur ions to the energy at which yield curves from the two models intersect, roughly  $E_T = 30$  keV and  $E_T = 50$  keV, respectively. Not only does this choice ensure continuity of the sputtering yield profiles for these two species, but the values of  $E_T$  are also close to the value of  $E_T \approx 100$  keV suggested by Cassidy et al. (2013). Since the starting energies of the ions modeled here are discrete, the shift of the transition energy from the 100 keV value suggested by Cassidy et al. (2013) to our proposed values only affects the calculation of sputtering yields at two energies (50 keV and 100 keV) for sulfur, and one energy (100 keV) for hydrogen. At these energy values, the yields from the empirical models of Johnson et al. (2009) and Famá et al. (2008) do not differ by more than a factor of three. As such, the shift of the transition energy from 100 keV to 50 keV (hydrogen) and 30 keV (sulfur) does not substantially affect our results. The models of the sputtering yields from *oxygen* ions presented by Famá et al. (2008) and Johnson et al. (2009) do not intersect, thus the occurrence of a discontinuity in the yield curve for oxygen can not be avoided. We therefore set the transition energy for sputtering by oxygen ions to  $E_T = 100$  keV, in agreement with the method of Cassidy et al. (2013). This approach results in a jump in the sputtering yields by a factor of approximately 1.5 at  $E_T = 100$  keV.

The expression presented by Famá et al. (2008) for the  $\text{H}_2\text{O}$  sputtering yield is written in terms of the nuclear and electronic stopping powers of incident ions ( $S_n(m, Z, E)$  and  $S_e(m, Z, E)$ , respectively), for which those authors provide empirical fits. These stopping powers represent the rate at which an incident ion loses its energy with depth in the surface, either by nuclear/momentum transfer (elastic) collisions ( $S_n(m, Z, E)$ ) or electronic excitation of surface molecules ( $S_e(m, Z, E)$ ). Nuclear collisions dominate the yields at projectile energies below  $\approx 50$  keV, while electronic excitation reactions become predominant at higher energies. The expression provided by Johnson et al. (2009) is a fit to laboratory data gathered in the electronic regime. Therefore, while this expression is not written in terms of the electronic stopping power  $S_e$ , it still describes yields  $Y$  associated with electronic sputtering.

Figure 1(a) displays the sputtering yields of  $\text{H}_2\text{O}$  as a function of projectile energy from 10 eV (approximately the corotation energy of protons) to 10 MeV, calculated from equation (1). We do not consider “secondary” sputtering of the surface by ionospheric



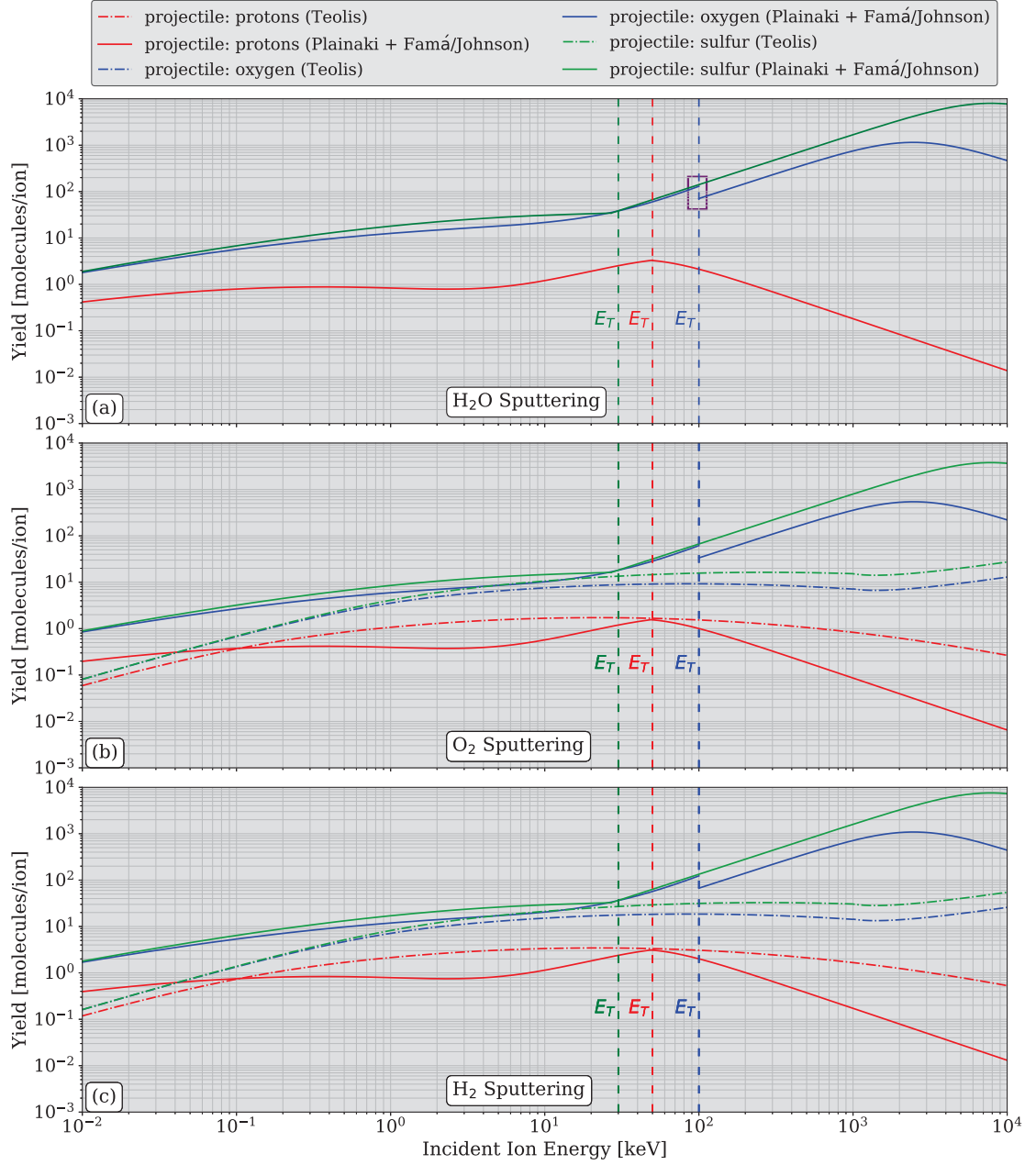


**Figure 1.** Sputtering yields in molecules/ion of H<sub>2</sub>O (panel (a)), O<sub>2</sub> (panel (b)), and H<sub>2</sub> (panel (c)) via impacts by normally-incident ( $\theta = 0^\circ$ ) hydrogen (red), oxygen (blue), and sulfur (green) ions with energies from 10 eV–10 MeV onto water ice at 100 K. Yields derived via the models of Plainaki et al. (2013), Famá et al. (2008) and Johnson et al. (2009) are shown as solid lines, while yields from Teolis et al. (2017) are shown as dash-dotted lines. The transition energy  $E_T$  is denoted with a vertical dashed line in the color corresponding to each species. The model of Famá et al. (2008) is applied for energies below the transition energy  $E_T$ , while the model Johnson et al. (2009) is used above  $E_T$ . The purple box near 100 keV in panel (a) highlights the unavoidable jump between the sputtering yields from oxygen ions of the two models. Yields derived with the model of Teolis et al. (2017) are valid across the entire energy range considered, i.e., we do not have to switch between different models at the transition energy.

pickup ions ( $E \ll 10$  eV), as the contribution of this process to atmospheric generation has been found to be a factor of 100 weaker than sputtering by magnetospheric ions (Saur et al., 1998). We note that sputtering by ionospheric ions may play an important role at Ganymede (Carnielli et al., 2020). In Figure 1(a) we discriminate between the three projectile ion species most prevalent along Europa’s orbit, with the yields from hydrogen, oxygen, and sulfur impacts shown in red, blue, and green, respectively. The transition energy  $E_T$  for each species is marked with a vertical, dashed line of corresponding color. Due to their similar atomic numbers, the H<sub>2</sub>O sputtering yields of incident oxygen and sulfur ions (blue and green curves) have very similar values over a wide range of energies; only at the very top of the energy range considered ( $E \approx 10$  MeV) do they differ by over an order of magnitude. The yield of incident hydrogen ions (red) is consistently smaller than that of the two heavy ion species, due to their small mass and atomic number. This difference in the H<sub>2</sub>O sputtering yields between hydrogen and oxygen/sulfur varies from a factor of approximately three at 10 eV to almost six orders of magnitude at 10 MeV (see Figure 1(a)). In general, the sputtering yields increase gradually with energy in the nuclear collision regime (below  $\approx 50$  keV), before growing rapidly above this energy due to the onset of electronic excitations. The sputtering yields of heavy ions maximize in the MeV regime, while the yields of protons maximize near 50 keV.

Laboratory experiments by Gibbs et al. (1988) and Vidal et al. (2005) revealed that sputtering yields follow a  $\cos^{-f(m)}(\theta)$  dependence on incidence angle in the electronic sputtering regime. Standard linear cascade theory predicts a similar dependence on incidence angle for nuclear sputtering yields (Famá et al., 2008). The form of  $f(m)$  for H<sub>2</sub>O sputtering is provided by Famá et al. (2008) based upon laboratory data, and ranges from  $f(m) \approx 1.3 - 1.8$  depending upon the projectile species. Therefore, sputtering yields can grow sharply with increasing incidence angle. For example, an impinging sulfur ion with an incidence angle of  $\theta = 80^\circ$  sputters up to twenty times more H<sub>2</sub>O than a sulfur ion with  $\theta = 0^\circ$ . This form of the angular dependence exhibits a singularity at  $\theta = 90^\circ$ , which would inflate the modeled sputtering yield to infinity. To avoid this, GEN-TOO does not initialize backtraced macroparticles exactly tangential to the surface, rather, only at angles of  $\theta \leq 87^\circ$ .

Previous studies of magnetospheric ion sputtering at Jupiter’s icy moons have typically assumed that all impinging ions hit the surface at the same incidence angle  $\theta$ . This assumption accounts for the fact that, in the absence of a detailed, high-resolution to-

pographical surface map (down to centimeter-scale), it is not feasible to precisely determine the incidence angle of an impinging ion. An ion may impact a crack or crevice on the moon’s surface and therefore impinge at a completely different angle than if it had hit a perfectly smooth sphere. Therefore, particle-tracing models often assume that the incidence angles of impacting ions average to a certain value within each cell of the grid used to discretize the surface. Cassidy et al. (2013) assumed a normal angle of incidence ( $\theta = 0^\circ$ ) for all impinging ions at Europa, while Carnielli et al. (2020) modeled ion sputtering at Ganymede with  $\theta = 45^\circ$ . So far, only Plainaki et al. (2015) studied ion sputtering at Ganymede without assuming a single, average incidence angle: their model considers the actual incidence angles of the ions onto a smooth sphere. Therefore, in order to constrain the uncertainties associated with the treatment of the incidence angle we will calculate H<sub>2</sub>O sputtering rates with (i) all ions treated as impacting normally (similar to Cassidy et al., 2013), and (ii) using the actual incidence angles onto a perfectly smooth sphere as obtained from GENTOO.

### 2.3.2 *Sputtering Yields of O<sub>2</sub> and H<sub>2</sub>*

Sputtering of O<sub>2</sub> and H<sub>2</sub> from Europa’s surface is the result of radiolysis and subsequent buildup of each type of molecule in the upper layers of the ice (e.g., Teolis et al., 2005, 2017). The sputtering of O<sub>2</sub> at Europa is of particular interest, as this process constitutes the main source of the moon’s near-surface (altitude < 300 km) exosphere. Within much of this region O<sub>2</sub> dominates the number density by up to two orders of magnitude, compared to H<sub>2</sub>O, H<sub>2</sub>, or other trace species (Plainaki et al., 2018; Vorburger & Wurz, 2018). However, the abundance of H<sub>2</sub>O has been found to exceed that of O<sub>2</sub> by an order of magnitude in a localized region above the central trailing hemisphere (Roth, 2021).

At the time of this study, two conceptually different models of O<sub>2</sub> sputtering have been applied in order to calculate the source rate of O<sub>2</sub> via magnetospheric ion sputtering at Europa. Plainaki et al. (2013) modeled the O<sub>2</sub> sputtering yield by using the temperature-dependent term in the equation for  $Y$  provided by Famá et al. (2008). They judged this approach to be accurate to within one order of magnitude. The sputtering yield of O<sub>2</sub> in this formulation (see, e.g, Plainaki et al., 2015) is given by

$$Y_{\text{O}_2}(m, Z, E, \theta, T) = \frac{1}{2} Y_{\text{H}_2\text{O}}(m, Z, E, \theta) \Phi(T) \quad , \quad (2)$$

where  $T$  is the temperature of the surface element from which material is sputtered, and  $Y_{\text{H}_2\text{O}}$  is given in equation (1). The temperature dependence of the sputtering yield,

$$\Phi(T) = q_0 \exp \left[ -\frac{E_A}{k_B T} \right] \quad , \quad (3)$$

resembles that of a Maxwell-Boltzmann distribution (Famá et al., 2008; Johnson et al., 2009; Teolis et al., 2017). In equation (3),  $q_0 = 1000$  is a scaling factor and  $E_A = 0.06$  eV is the activation energy required for breakdown of surface constituents (Johnson et al., 2009). The factor of  $\frac{1}{2}$  in equation (2) arises from the fact that two  $\text{H}_2\text{O}$  molecules must be decomposed in order for one  $\text{O}_2$  to form (Cassidy et al., 2010). The sputtering yield of  $\text{H}_2$  is therefore always twice that of  $\text{O}_2$ , i.e.,

$$Y_{\text{H}_2}(m, Z, E, \theta, T) = 2 Y_{\text{O}_2}(m, Z, E, \theta, T) \quad , \quad (4)$$

which holds regardless of the formulation for  $Y_{\text{O}_2}(m, Z, E, \theta, T)$ . Figures 1(b) and 1(c) display the sputtering yields at  $T = 100$  K (roughly the mean temperature of Europa's surface, e.g., Spencer et al., 1999) of  $\text{O}_2$  and  $\text{H}_2$ , respectively. The factor  $\Phi(T)$  becomes ranges from a value of  $10^{-2}$  at 60 K to a value of 7 at 140 K, the approximate minimum and maximum surface temperatures at Europa (e.g., Spencer et al., 1999; Oza et al., 2019). Therefore, the  $\text{O}_2$  and  $\text{H}_2$  yields calculated via the model of Plainaki et al. (2013) follow from the  $\text{H}_2\text{O}$  yields (equation (1)) by multiplication with  $\frac{1}{3}\Phi(T)$  for oxygen and  $\frac{2}{3}\Phi(T)$  for hydrogen. In Figure 1, we calculate the yield curves assuming a constant surface temperature of  $T = 100$  K.

The  $\text{O}_2$  sputtering yield model of Plainaki et al. (2013) is based upon available sputtering models of  $\text{H}_2\text{O}$ . As such, it assumes that, like  $\text{H}_2\text{O}$ , substantial amounts of  $\text{O}_2$  are present at any depth to which a magnetospheric ion may penetrate. Hence, their sputtering yield grows with energy, since higher energy ions penetrate deeper into the surface (up to  $10^7$  Å for 10 MeV protons, see, e.g., Teolis et al., 2017) and interact with more material than their lower energy counterparts.

An alternative method for calculating the sputtering yields of  $\text{O}_2$  and  $\text{H}_2$  is presented by Teolis et al. (2010, 2017). Based upon the findings of Petrik et al. (2006) and Teolis et al. (2005, 2009), these authors suggested that  $\text{O}_2$  and  $\text{H}_2$  molecules are mainly concentrated within the first  $\approx 28$  Å of Europa's surface, while their densities decrease sharply below this thin upper layer. Thus, penetration of projectile ions beyond this thin layer makes only a very minor additional contribution to the release of  $\text{O}_2$  or  $\text{H}_2$ . Teolis

et al. (2010, 2017) formulate a novel method of calculating O<sub>2</sub> sputtering yields which considers this decreasing density of sputterable molecules at ion penetration depths greater than  $\approx 28 \text{ \AA}$ . Their expression for O<sub>2</sub> sputtering yields reads

$$Y_{\text{O}_2}(E, \theta, T) = E g_{\text{O}_2}^0 x_0 \left[ 1 - \exp \left( \frac{-r_0(E) \cos(\theta)}{x_0} \right) \right] \frac{1}{r_0(E) \cos(\theta)} (1 + \Phi(T)) \quad , \quad (5)$$

where  $g_{\text{O}_2}^0 = 5 \times 10^{-3} \text{ eV}^{-1}$  is the (constant) sputtering yield per energy when the surface temperature is below  $\approx 80 \text{ K}$ ,  $x_0 = 28 \text{ \AA}$  is the thickness of the concentrated layer of O<sub>2</sub> and H<sub>2</sub> molecules directly beneath the surface, and  $r_0(E)$  is the energy-dependent penetration range of the projectile (Ziegler & Manoyan, 1988; Teolis et al., 2017). The sputtering yields of H<sub>2</sub> are again twice the O<sub>2</sub> yields (equation (4)). The form of  $\Phi(T)$  is the same as in equation (2). Values of  $r_0(E)$  in our model are taken from a fit to the curve provided by Teolis et al. (2017) in their Figure 4. When the penetration depth  $r_0(E) \cos(\theta)$  of the projectile, i.e., the penetration range  $r_0(E)$  projected onto the local surface normal, greatly exceeds the O<sub>2</sub> layer depth  $x_0$ , the exponential term in equation (3) approaches zero. The sputtering yield of O<sub>2</sub> then becomes inversely proportional to the energy-dependent penetration depth. Note that the angular dependence of equation (5) is limited to the two occurrences of the penetration depth of the projectile,  $r_0(E) \cos(\theta)$ . At high penetration depths ( $r_0(E) \cos(\theta) \gg x_0$ ), the yield becomes proportional to  $\cos^{-1}(\theta)$ , similar to the angle dependence of equations (1) and (2) with  $f(m) = 1$ . Due to the negligible sticking coefficient of O<sub>2</sub> (Saur et al., 1998), it is not necessary to include a reduction factor in the O<sub>2</sub> yields to account for sticking within the regolith (as is done for H<sub>2</sub>O).

Yields derived at  $T = 100 \text{ K}$  with the formulation of Teolis et al. (2010, 2017) are shown in Figures 1(b) for O<sub>2</sub> and 1(c) for H<sub>2</sub> as dash-dotted lines. Only for oxygen and sulfur impacts between 1 keV and 30 keV do the O<sub>2</sub> yields calculated with the model of Teolis et al. (2017) approximately match those of Plainaki et al. (2012). The yields from the two models differ by up to an order of magnitude below this energy range, and by over two orders of magnitude above this range. For hydrogen impacts, sputtering yields calculated with the methods of Plainaki et al. (2012) and Teolis et al. (2017) are different by 1-2 orders of magnitude across the entire energy range considered, except in very narrow windows near  $4 \times 10^{-2} \text{ keV}$  and 100 keV (see Figure 1(a)). The yields from the model of Teolis et al. (2017) initially grow with energy (and associated penetration depth), but level off near 10 keV as the ions pass deeper into surface layers where little O<sub>2</sub> or H<sub>2</sub> is present.

Observed sputtering yields of O<sub>2</sub> and H<sub>2</sub> increase exponentially with temperature above  $\sim 70$  K, while below 70 K they are roughly constant with temperature (Baragiola et al., 2003). The models of Plainaki et al. (2012) and Teolis et al. (2017) each utilize a slightly different form to emulate this temperature dependence:  $Y \propto \Phi(T)$  and  $Y \propto [1 + \Phi(T)]$ , respectively (see equations (2) and (5)). Therefore, while the O<sub>2</sub> sputtering yields of Plainaki et al. (2012) approach a value of zero when the surface temperature decreases below 70 K, the yields of Teolis et al. (2017) level off at nonzero values in this temperature regime, which more closely matches laboratory measurements (see Figure 5 of that paper).

In addition, Teolis et al. (2005, 2010, 2017) suggest that a water ice surface requires a minimum irradiation dosage of  $10^{15}$  cm<sup>-2</sup> before the O<sub>2</sub> sputtering yield displays a response to changes in the surface temperature. At Europa, such a dosage from impinging magnetospheric ions alone requires approximately three orbits around Jupiter to accumulate (Addison et al., 2021). Considering only magnetospheric ion bombardment, a discernible reaction of the O<sub>2</sub> sputtering rate at Europa to varying solar orientation (Plainaki et al., 2013) would therefore only occur on time scales far greater than the moon’s orbital period. In other words, the surface temperature profile would be “reset” before the ice has adjusted to the change in temperature encountered along Europa’s orbit. In this picture, the sputtering yields can be calculated by considering a diurnally-averaged temperature profile (i.e., averaged over an entire orbit).

However, magnetospheric electrons also impart a significant irradiation dosage onto Europa’s surface (e.g., Paranicas et al., 2001, 2007; Dalton et al., 2013). Indeed, recent analysis by Davis et al. (2021) suggests that electrons may irradiate Europa’s surface at even higher levels than the ions, although their study did not take into account shielding of the surface by the moon’s plasma interaction. Such shielding has been found to sharply reduce the precipitation of magnetospheric electrons onto Callisto (Liuzzo et al., 2019a). Therefore, the magnetospheric electron fluxes onto Europa’s surface calculated by, e.g., Paranicas et al. (2001, 2007), Dalton et al. (2013), and Nordheim et al. (2018) for uniform fields can be considered only an upper limit to electron surface irradiation. However, modeling of magnetospheric electron bombardment at Europa is a non-trivial task, requiring extensive modifications to the GENTOO framework. Electrons with energies greater than 50 keV display significant relativistic mass growth, changing the equation of motion that must be solved in order to determine their trajectories. Furthermore,

the bounce times of magnetospheric electrons can be smaller than the convection time of the plasma through Europa's interaction region (Paranicas et al., 2009). Modeling of electron bombardment therefore requires the implementation of a global model of Jupiter's magnetosphere, and is beyond the scope of this study. However, if electrons contribute to surface irradiation to the same extent (or greater) as the ions, the  $10^{15} \text{ cm}^{-2}$  irradiation dose required for the ice to adapt to surface temperature changes (Teolis et al., 2017) may be reached in far less than a European day. In that case, variations of the surface temperature profile generated by Europa's changing orientation with respect to the Sun need to be considered.

Our study will take into account the availability of two conceptually different models of  $\text{O}_2$  and  $\text{H}_2$  sputtering at Europa. In addition, we consider the uncertainty regarding the response of surface sputtering to changes in the incident solar flux which results from the moon's orbital motion. We shall compare maps of the  $\text{O}_2$  and  $\text{H}_2$  sputtering rates utilizing the approaches of both Plainaki et al. (2013) and Teolis et al. (2017). In addition, we will model the spatial distribution of  $\text{O}_2$  and  $\text{H}_2$  sputtering rates for four different orientations of the Sun relative to the incident plasma flow, as well as for a temperature profile averaged over a full European day. Specifically, we examine the  $\text{O}_2$  and  $\text{H}_2$  sputtering rates at Europa while the moon is located at 06:00 LT, 12:00 LT, 18:00 LT, and 23:30 LT. We do not consider the scenario of exactly 00:00 LT, as in this configuration Europa is in eclipse (see, e.g., Cassidy et al., 2008; Oza et al., 2019). The moon only spends approximately 3% of its orbit in eclipse, and the surface temperature quickly recovers (after approximately 6 hours, compared to an orbital period of 80 hours, see, e.g., Oza et al., 2019). Since our priority is to systematically assess the role of changing solar orientation along a full orbital period (rather than the special case of eclipse), we calculate maps of the  $\text{O}_2$  and  $\text{H}_2$  surface sputtering rate at 23:30 LT, just prior to Europa entering Jupiter's optical shadow. In this case, the sub-solar point is located only  $6^\circ$  east of where it would be in the (hypothetical) case of a Sun-illuminated Europa at 00:00 LT.

A global illustration of Europa's orbit showing each of these four cases, along with maps of the resultant surface temperature profiles, is displayed in Figure 2. Maps of the surface temperature are displayed in the West Longitude system, where longitude  $\phi$  increases in a clockwise direction when viewed from the north ( $z > 0$ ). In this system, Europa's sub-Jovian, downstream, anti-Jovian, and upstream apices are located at  $\phi =$

0°, 90°, 180°, and 270°, respectively. These maps range in latitude from  $\lambda = -90^\circ$  (denoting the south pole) to  $\lambda = 90^\circ$  (north pole).

For each of these four orbital positions, a map of the surface temperature profile is calculated using the thermophysical model THERMPROJRS (Spencer et al., 1989, 1999). The THERMPROJRS model solves the conductive heat flow equation for a surface layer of a given thermal inertia and bolometric albedo. A steady-state surface temperature is then calculated assuming equilibrium between solar heat influx and thermal emission from the moon. For our simulations, we utilize values of the emissivity and thermal inertia at Europa of 0.9 and  $7 \times 10^4 \text{ erg cm}^{-2} \text{ s}^{-1/2} \text{ K}^{-1}$ , in agreement with Spencer et al. (1999). Their thermophysical model assumes the albedo to be uniform across Europa’s surface. However, analysis of Galileo Photopolarimeter-Radiometer (PPR) data by Rathbun et al. (2010) and Oza et al. (2019) has demonstrated that Europa’s surface albedo varies linearly with longitude from a minimum of 0.45 near the upstream apex to a maximum of 0.65 near the downstream apex. In order to capture this upstream-downstream asymmetry in Europa’s surface brightness, we set the albedo to 0.45 at 18:00 LT (where the moon’s dayside and upstream hemispheres coincide), and to 0.65 at 06:00 LT (where the dayside and downstream hemispheres coincide). At 12:00 and 23:30 LT, when Europa’s terminator plane is approximately aligned with the corotation direction, the albedo is set to 0.55, i.e., we use the average of the upstream and downstream hemisphere values. The lower albedo at 18:00 LT in our model results in a slightly higher surface temperature by approximately 15% compared to 06:00 LT, and 8% compared to 12:00 and 23:30 LT (Figure 2). The temperature maps in Figure 2 each display a bullseye-like enhancement around the apex of the dayside hemisphere, as well as a “tail” of increased temperature extending eastward. This tail is a result of the thermal inertia of the surface material, which partially retains the heat after a surface element has rotated out of daylight.

The four surface temperature profiles shown in Figure 2 are averaged in order to produce a map of the average temperature profile over a complete orbit (“diurnal-average”, see Figure 3). The diurnally-averaged temperature profile is *not* uniform in longitude, since the sun-lit hemisphere heats to higher temperatures at 18:00 LT than at 06:00 LT. Averaging the surface temperature over a full European orbit therefore results in a profile which is hotter upstream and cooler downstream, albeit with a weaker upstream-downstream discrepancy compared to 18:00 LT ( $\approx 45 \text{ K}$  versus  $\approx 60 \text{ K}$ , see Figures 2 and 3). In re-



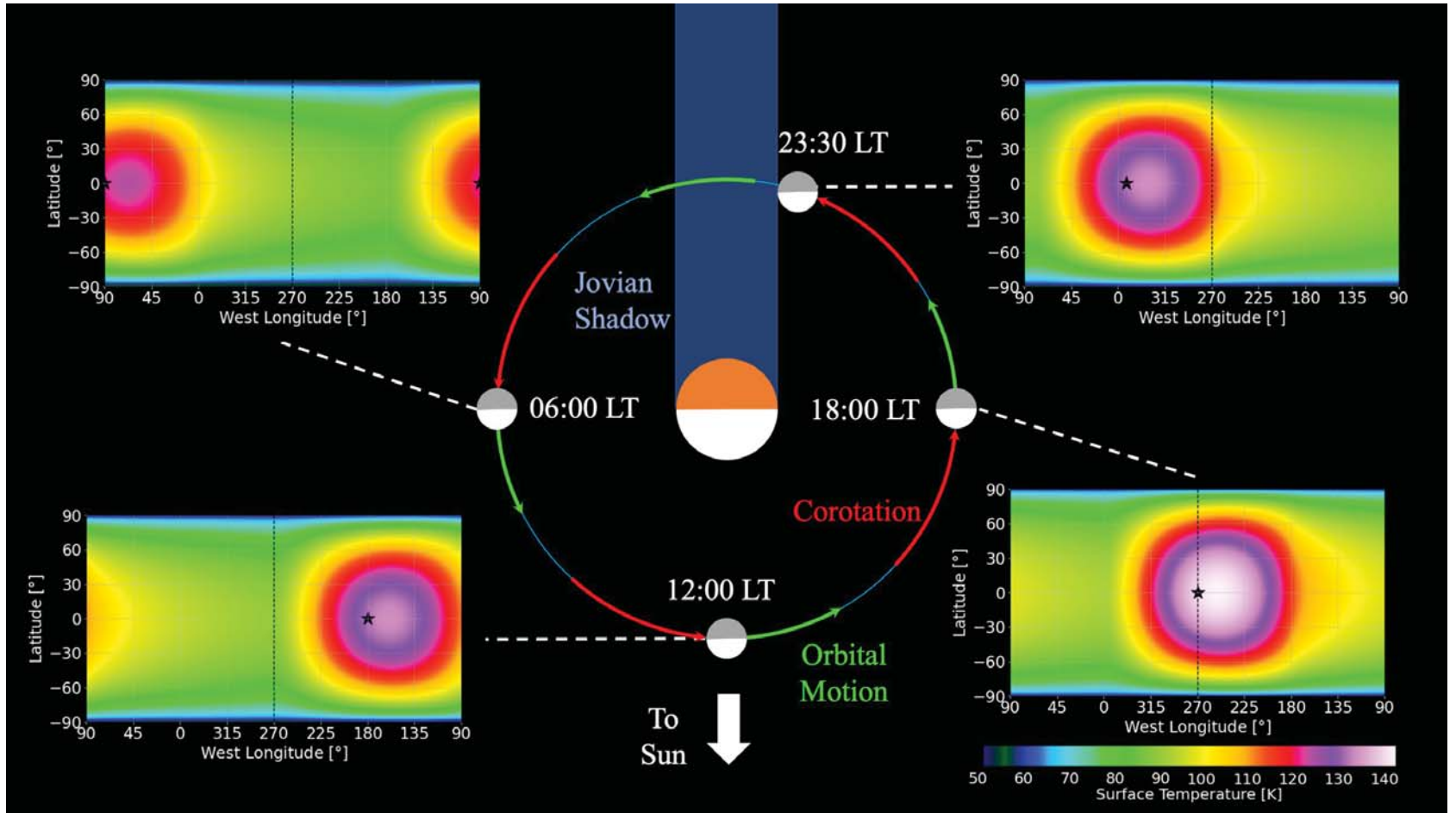


**Figure 2.** Orientation of Europa relative to Jupiter and the Sun for 06:00, 12:00, 18:00, and 23:30 LT, as described in section 2.3.2. Jupiter (orange nightside and white dayside) is located in the center of the figure. Red arrows indicate the direction of the corotating plasma flow, while green arrows indicate the direction of Europa's orbital motion. For each orbital position, Europa's nightside hemisphere is shown in gray, while the Sun-lit/dayside hemisphere is colored white. Next to each of the four orbital positions is a plot of the surface temperature profile in West Longitude coordinates, with Europa's sub-Jovian, downstream, anti-Jovian, and upstream apices located at longitudes of 0°, 90°, 180°, and 270°, respectively. The sub-solar point is marked with a black star, and a vertical dashed line marks a semi-meridian through the upstream apex. Note that at 06:00 LT, the black star is split between the left and right sides of the temperature map.

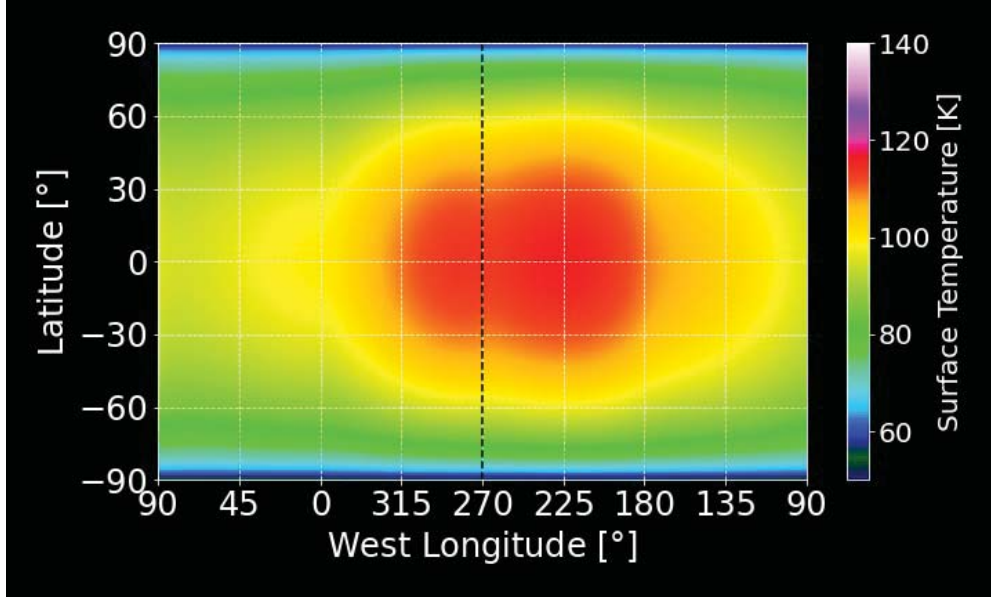


**Figure 3.** Diurnally-averaged surface temperature profile at Europa, calculated using the four temperature profiles shown in Figure 2.

ality, the diurnally-averaged temperature profile may be slightly cooler, since our model does not consider the drop in surface temperature during and after eclipse. In each scenario (the four local times and the diurnal average), the  $\text{O}_2$  and  $\text{H}_2$  sputtering yields are calculated with the respective temperature profile and the temperature dependence  $\Phi(T)$ , as given in equations (2) and (5).

### 3 Results

#### 3.1 Hybrid Simulation of Europa's Electromagnetic Environment

Figure 4 displays the structure of Europa's perturbed electromagnetic and plasma environment, as calculated by the AIKEF model. All quantities in Figure 4 are presented in cuts through the three-dimensional simulation domain at  $y = 0$ , i.e., in the plane that contains the corotational flow velocity  $\mathbf{u}_0$ , the background magnetic field  $\mathbf{B}_0$ , and the center of the moon. The first row (panels 4(a) and 4(b)) displays the flow-aligned component of the magnetic field,  $B_x$ , and the magnitude of the magnetic field,  $|\mathbf{B}|$ , respectively. The magnitude of the electric field,  $|\mathbf{E}|$ , is shown in panel 4(c). Finally, the number density of the corotating plasma,  $n$ , is presented in panel 4(d).

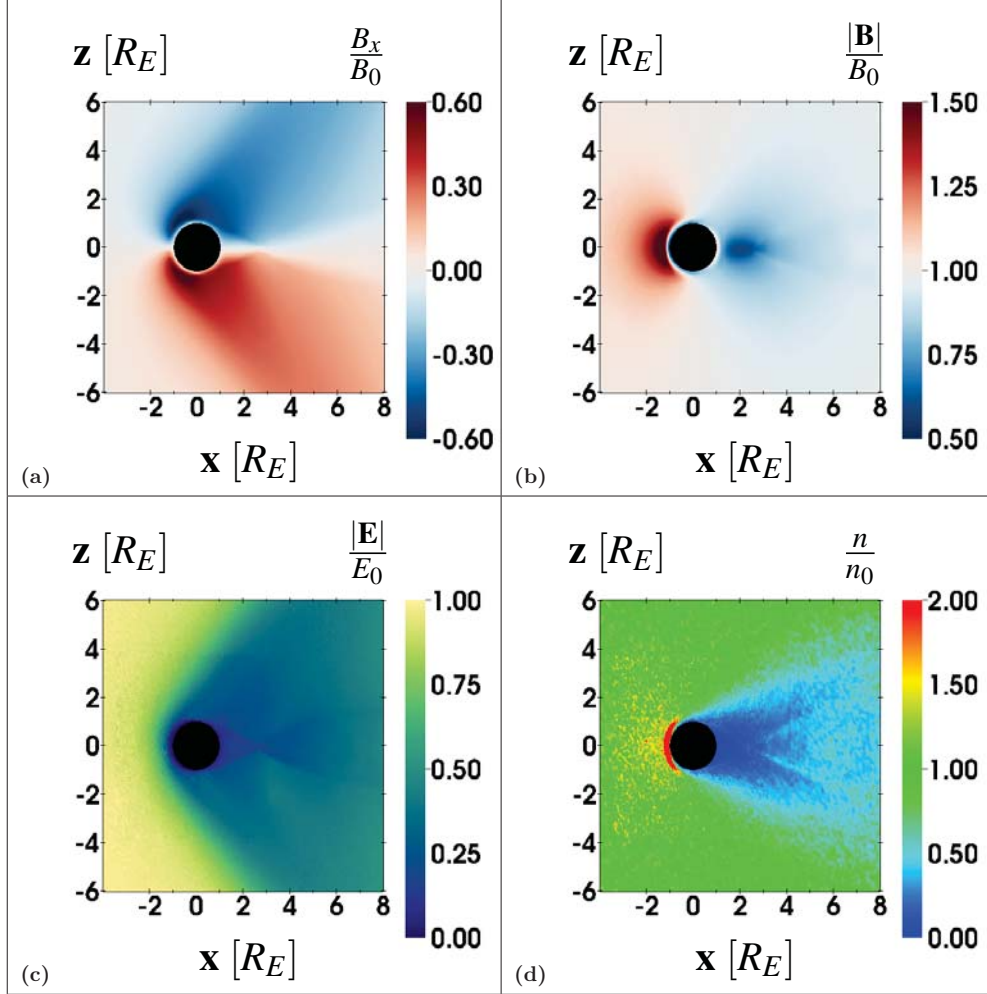


**Figure 4.** Electromagnetic and plasma environment near Europa, as calculated by the AIKEF model. All quantities are shown in cuts through the  $(x, z)$  plane, which contains the upstream flow velocity  $\mathbf{u}_0$ , the background magnetic field  $\mathbf{B}_0$ , and the center of Europa. Panels (a) and (b) display the  $B_x$  component and magnitude of the magnetic field, respectively, as a fraction of the background field magnitude  $|\mathbf{B}_0| = B_0 = 410$  nT. Panel (c) displays the electric field magnitude, normalized to the background convective electric field strength  $E_0 = u_0 B_0 = 41$  mV/m. Panel (d) displays the number density of the magnetospheric plasma, as a fraction of the upstream density  $n_0 = 200$  cm $^{-3}$ .

Ionization of Europa's exosphere drains momentum from the upstream plasma, causing the magnetospheric ion number density to grow to over twice the background value  $n_0 = 200 \text{ cm}^{-3}$  above the moon's upstream hemisphere (Figure 4(d)). Ionospheric ions are convected downstream, refilling the moon's magnetospheric plasma wake and maintaining pressure balance with the adjacent flow (see Figure 3 of Addison et al., 2021). The frozen-in magnetospheric field lines pile up above Europa's orbital trailing hemisphere, leading to an enhancement in the magnetic field magnitude by 50% compared to the background value (red region in Figure 4(b)). This upstream pileup is accompanied by a weakening of the magnetic field magnitude by 50% immediately downstream of the moon (blue region in Figure 4(b)). The plasma interaction also generates a system of Alfvén wings which extend north and south from Europa to Jupiter's polar ionosphere (Neubauer, 1980, 1998). The Alfvén wings are tilted against the  $z$  axis by an angle of  $\arctan(M_A) = 34^\circ$ , where  $M_A = 0.68$  is the Alfvénic Mach number. Inside of the Alfvén wing tubes the field possesses a flow-aligned component south of the moon ( $B_x > 0$ , red region in Figure 4(a)), and a component antiparallel to the flow direction north of the moon ( $B_x < 0$ , blue region in Figure 4(a)). The magnetospheric plasma slows within and downstream of the Alfvén wings, causing the downstream reduction in the electric field seen in Figure 4(c).

For a more detailed discussion of the electromagnetic field perturbations near Europa, the reader is referred to our numerous preceding publications that applied the same model to this moon (Arnold et al., 2019; Arnold, Liuzzo, & Simon, 2020; Arnold, Simon, & Liuzzo, 2020; Breer et al., 2019; Addison et al., 2021).

### 3.2 Magnetospheric Ion Surface Fluxes and Sputtering Rates of $\text{H}_2\text{O}$

In Figure 5 we present maps of the magnetospheric ion surface fluxes onto Europa for both the thermal (panels 5(a) and 5(b)) and energetic (panels 5(c) and 5(d)) regime, as calculated by the GENTOO model. The left column (panels 5(a) and 5(c)) displays flux maps calculated with only the uniform Jovian magnetic field  $\mathbf{B}_0$  and the undisturbed convective electric field  $\mathbf{E}_0$ , while the right column displays flux maps determined with the perturbed electromagnetic fields from AIKEF (see Figure 4). Figure 6 features maps of the  $\text{H}_2\text{O}$  sputtering rates across Europa's surface from thermal ions (panels 6(a)–6(c)), energetic ions (panels 6(d)–6(f)), and magnetospheric ions of all energies and species considered in this study (panels 6(g)–6(i)). The first column (panels 6(a), 6(d), and 6(g))

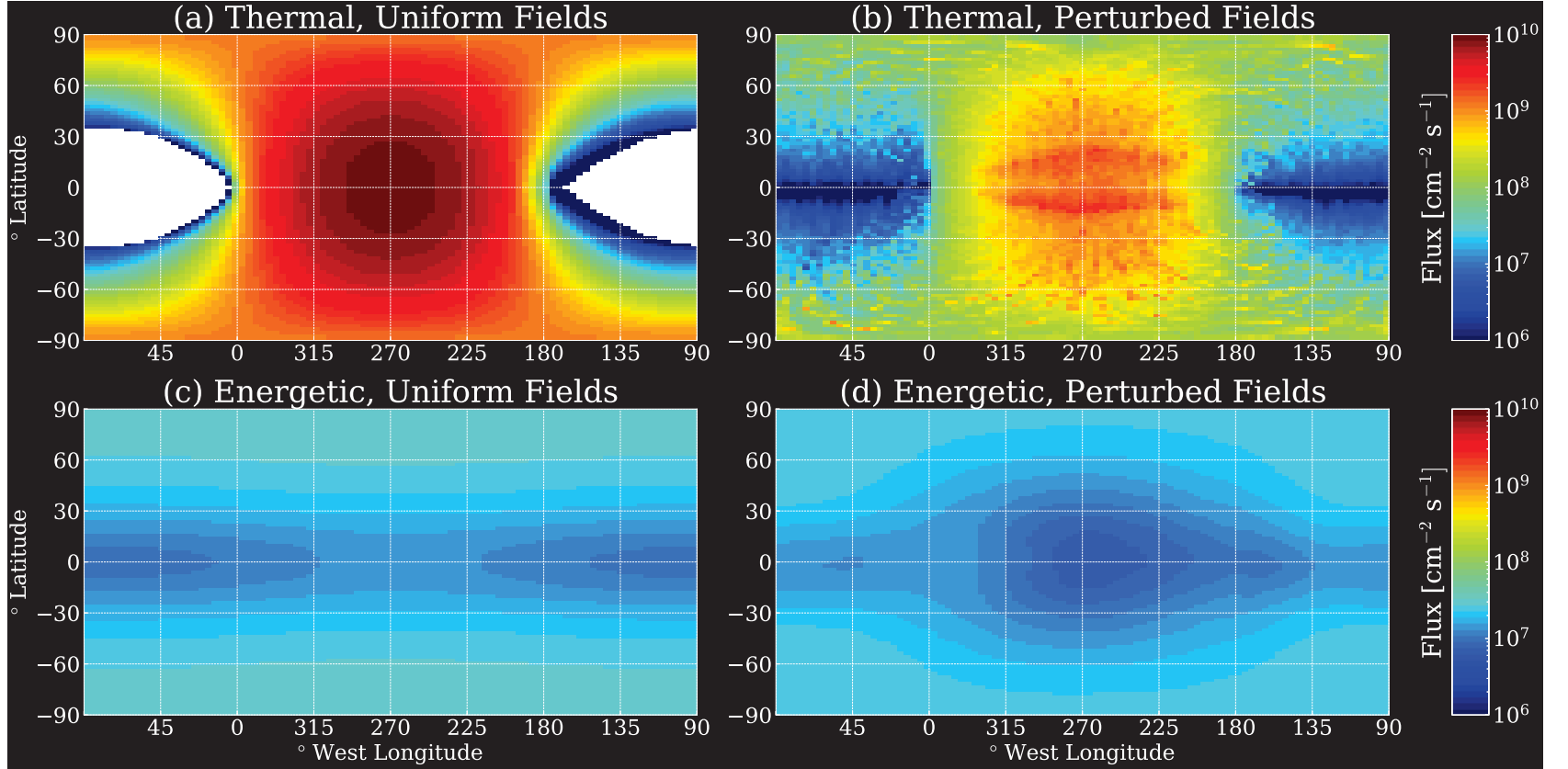


**Figure 5.** Surface flux maps of magnetospheric ions (hydrogen, oxygen, and sulfur) at Europa, calculated with the GENTOO model. The first row (panels (a) and (b)) displays the surface flux of the thermal ion population, while the second row (panels (c) and (d)) shows the flux from the energetic ion population (energies  $5\text{keV} \leq E \leq 10\text{MeV}$ ). The left column (panels (a) and (c)) shows fluxes calculated with the uniform electromagnetic fields  $\mathbf{B}_0$  and  $\mathbf{E}_0$ , while the right column (panels (b) and (d)) shows fluxes calculated with the perturbed fields determined by AIKEF. Each map is shown in the West Longitude system. The white region in panel (a) indicates areas in Europa's downstream hemisphere where the thermal ion surface flux is exactly zero.

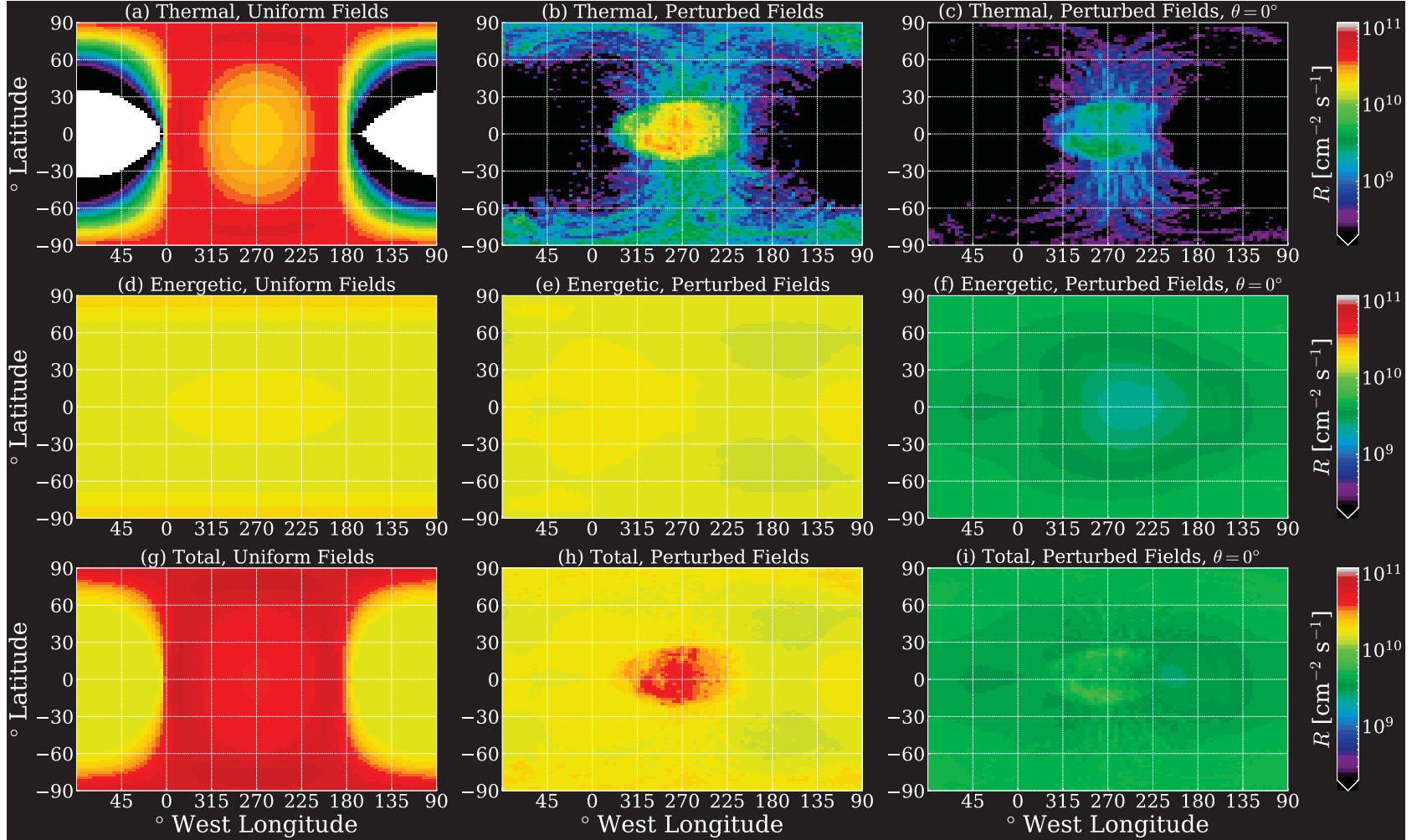


**Figure 6.**  $\text{H}_2\text{O}$  surface sputtering rates from impacts by all magnetospheric ion species (hydrogen, oxygen, and sulfur) considered in this study. Each map is displayed in the West Longitude system as described in the text. The first column (panels (a), (d), and (g)) shows  $\text{H}_2\text{O}$  sputtering rates calculated with only the uniform background electromagnetic fields  $\mathbf{B}_0$  and  $\mathbf{E}_0$  included, while the second column (panels (b), (e), and (h)) displays  $\text{H}_2\text{O}$  sputtering rates calculated using Europa's perturbed electromagnetic environment from the AIKEF model. Both the first and second columns utilize the actual incidence angles  $\theta$  of the incoming ions in their calculation of the sputtering yields (equation (1)). The third column (panels (c), (f), and (i)) displays  $\text{H}_2\text{O}$  sputtering rates calculated with perturbed electromagnetic fields (as in the second column), but with the incidence angles of all impinging ions set to  $\theta = 0^\circ$  in equation (1). From top to bottom, the rows display  $\text{H}_2\text{O}$  sputtering rates of thermal ions (panels (a)–(c)), energetic ions with energies  $5\text{keV} \leq E \leq 10\text{MeV}$  (panels (d)–(f)), and the total sputtering rate of all magnetospheric ions (thermal and energetic, panels (g)–(i)). White regions in panel (a) indicate areas where the sputtering rate from thermal ion impacts is exactly zero.



displays H<sub>2</sub>O sputtering rates calculated with a uniform field configuration, as well as with the modeled incidence angles from GENTOO used in equation (1). Sputtering rates calculated with the perturbed fields from AIKEF and the incidence angles from GENTOO are presented in the second column (panels 6(b), 6(e), and 6(h)).

Finally, to isolate the influence of non-uniform ion incidence angles on the H<sub>2</sub>O sputtering rate, the third column (panels 6(c), 6(f), and 6(i)) displays H<sub>2</sub>O sputtering rates determined with perturbed fields, but with the incidence angle of all impinging ions set to a constant value ( $\theta = 0^\circ$ ) in equation (1). This specific choice of incidence angle is consistent with the approach of Cassidy et al. (2013), but still somewhat arbitrary. Regarding the angle dependence of the sputtering yields, the choice of  $\theta = 0^\circ$  gives equal weight to all three ion species ( $\cos^{-f(m)}(0) = 1$ ), while a value of  $\theta > 0^\circ$  weights the three species differently (due to the mass dependence of  $f(m)$ ). However, choosing a value of, e.g.,  $\theta = 45^\circ$ , as done at Ganymede by Carnielli et al. (2020), results in (at maximum) a 14% enhancement of the H<sub>2</sub>O sputtering yield of one ion species compared to another. Therefore, the choice of a constant incidence angle  $\theta > 0^\circ$  would only cause a minor, quantitative enhancement of the H<sub>2</sub>O sputtering rate compared to when  $\theta = 0^\circ$ , and would not appreciably alter the spatial distribution of our modeled rates.

When the electromagnetic fields near Europa are treated as uniform, the corotating thermal plasma can impinge unimpeded onto the moon’s upstream hemisphere. In this case, the spatial distribution of the thermal ion surface flux onto Europa’s upstream hemisphere (180°–360° west longitude, Figure 5(a)) is mainly determined by the cosine of the angle between the normal vector at each surface location and the corotation direction (+ $x$ , see also equation (8) in Addison et al., 2021). This angle grows from 0° at the upstream apex to 90° at surface locations in the  $x = 0$  plane (0° W and 180° W longitudes, at all latitudes), and is rotationally symmetric around the  $x$  axis. The surface flux of the impinging thermal ions therefore drops with distance from the upstream apex, as the angle between the corotation direction and the surface normal vector grows. This results in a bullseye-like flux pattern in the upstream hemisphere, as also found by Cassidy et al. (2013) and Addison et al. (2021).

The downstream hemisphere between  $\lambda = -30^\circ$  and  $\lambda = 30^\circ$  latitude is mainly devoid of thermal ion influx, as many of the thermal ions are prevented access to this region by the solid body of Europa (Figure 5(a)). However, the thermal velocity of the

corotating magnetospheric ions can achieve values of over 60% of the bulk speed  $u_0$  (see section 2.2). Thus, the velocity vectors of a significant number of thermal ions near the moon are strongly inclined against the corotation direction. These ions are able to reach the high-latitude regions on Europa’s downstream hemisphere without being intercepted by the moon’s upstream surface.

The sputtering rates  $R$  of thermal ions in uniform fields (Figure 6(a)) achieve their peak values (up to  $R = 6 \times 10^{10} \text{cm}^{-2} \text{s}^{-1}$ ) on the upstream hemisphere, but are zero on the downstream hemisphere equatorward of  $\pm 30^\circ$  latitude. However, unlike the thermal ion surface flux, the  $\text{H}_2\text{O}$  sputtering rate of thermal ions (Figure 6(a)) does *not* maximize near the upstream apex. Rather, the  $\text{H}_2\text{O}$  sputtering rate from thermal ion impacts grows monotonically with distance from the upstream apex and maximizes in the region where the  $x = 0$  plane intersects Europa (dark red in Figure 6(a)). To explain this behavior, we consider ions whose velocity vectors are nearly aligned with the corotation direction, i.e., ions which originate from the region of velocity space where the Maxwellian distribution peaks and the bulk of the upstream thermal population is concentrated. For such an ion, the impact angle  $\theta$  in equation (1) is approximately given by the angle between the corotation direction and the surface normal vector. The contribution that such an ion makes to the surface flux is proportional to  $\cos(\theta)$ , whereas the ion’s sputtering yield is proportional to  $\cos^{-f(m)}(\theta)$ . The ion’s contribution to the sputtering rate, which is the product of these two quantities, is therefore proportional to  $\cos^{1-f(m)}(\theta)$ . Since  $f(m) > 1$  for all ion species (Famá et al., 2008), the sputtering rate of ions that move (nearly) along the corotation direction and impact the upstream hemisphere increases with distance from the upstream apex, i.e., as the angle between the ion’s velocity vector and the surface normal grows. This increase in sputtering rates with distance from the upstream apex is opposite to the pattern predicted by Cassidy et al. (2013) for uniform fields, as those authors treated all thermal ions as impacting the surface with the same incidence angle ( $\theta = 0^\circ$ ) when calculating sputtering yields.

Including the influence of Europa’s plasma interaction on magnetospheric ion trajectories drastically alters the spatial distribution of the thermal ion surface flux (Figure 5(b)). In this scenario, thermal ions no longer have unimpeded access to the moon’s upstream hemisphere. Deflection of thermal ions in the magnetic pileup region is too weak to appreciably reduce ion flux onto Europa’s upstream hemisphere (Addison et al., 2021). Deflection of thermal ions away from the moon is caused almost entirely by the Alfvén



wings, which encapsulate Europa and its exosphere. The bulk of the thermal ions which enter Europa’s interaction region are diverted around the Alfvén wing tubes, and pass by the moon’s sub-Jovian and anti-Jovian flanks (see also Figure 2 of Simon et al., 2021). Deflection of thermal ions around Europa’s Alfvén wings reduces the ion surface flux by over an order of magnitude at nearly all locations on the upstream hemisphere (Addison et al., 2021). As shown by Simon et al. (2021), the small number of ions which penetrate the wing tubes move almost completely in the corotation direction, since the ionospheric Hall Effect is too weak at Europa to drastically break the symmetry of the ion flow pattern between the sub-Jovian and anti-Jovian hemispheres. In analogy to the case of uniform fields, the influx pattern of these ions onto the upstream hemisphere is therefore determined by the cosine of the angle between the corotation direction and the local surface normal. Hence, even when the field perturbations are taken into account, the spatial distribution of the thermal ion flux onto the upstream hemisphere retains something of the bullseye-like distribution seen in the case of uniform fields (Figure 5(a)). We note that the model of Simon et al. (2021) applies a fluid approach to describe ion dynamics. Hence, their model does not capture individual ions from the “edges” of the Maxwellian upstream distribution that impinge onto Europa at large angles against the corotation direction.

Although the bulk of the thermal ions move along the corotation direction, a non-negligible fraction of the upstream ions have velocity vectors which are significantly inclined against the corotation direction. These ions are deflected by the draped magnetic fields onto Europa’s downstream and polar regions (Addison et al., 2021). The thermal ion flux onto the polar caps is therefore similar in magnitude to that at lower latitudes of the upstream hemisphere, except near the upstream apex where the thermal ion surface flux is higher by two orders of magnitude. The deflection of ions with highly-inclined trajectories against the corotation direction onto the high-latitude regions leaves an equatorial depletion in flux by up to three orders of magnitude compared to the polar and low-latitude upstream regions (dark blue region in Figure 5(b)). This is in contrast to a uniform field geometry, where *no* thermal ions can reach the downstream hemisphere between approximately  $-30^\circ$  and  $30^\circ$  latitude (white regions in Figure 5(a)).

The alterations to the thermal ion flux pattern brought on by the field perturbations carry over into the  $\text{H}_2\text{O}$  sputtering rates (Figure 6(b)). For perturbed fields, the spatial distribution of the rates from thermal ions sputtering is remarkably similar to the

pattern seen in the thermal ion flux (Figure 5). Unlike in the case of uniform electro-magnetic fields (Figure 6(a)), the H<sub>2</sub>O sputtering rate for perturbed fields (Figure 6(b)) does indeed maximize near the trailing apex (270° W) in an elliptically-shaped region which extends approximately 45° east and west of the upstream apex and 30° north and south. This elliptical region of enhanced H<sub>2</sub>O sputtering corresponds to the ion surface flux enhancement centered near the upstream apex (Figure 5(b)). This enhancement possesses a minor east-west asymmetry, which results from the (small) rotation of the electric field against the  $-\hat{\mathbf{y}}$  axis by the ionospheric Hall Effect. Simon et al. (2021) estimated that this angle of rotation may reach about 16°, consistent with the rather subtle east-west asymmetry in Figure 6(b). The draping of the magnetic field lines allows thermal ions with a greater range of incidence angles to impinge upon each surface location on the upstream hemisphere, compared to when the fields are uniform. In particular, ions with grazing trajectories may impinge onto the surface near the upstream apex, while ions with trajectories normal to the surface may impact far from the upstream apex (see Figure 5 of Addison et al., 2021). As such, the increase in the H<sub>2</sub>O sputtering rate with distance from the upstream apex seen in uniform fields (Figure 6a) does not occur when the field perturbations are included. In draped fields, the H<sub>2</sub>O sputtering rate from thermal ions decreases with distance from the upstream apex, and falls off sharply upon entering the downstream hemisphere. The H<sub>2</sub>O sputtering rate is 2-3 orders of magnitude lower on the downstream hemisphere than it is near the upstream apex. The near-equatorial depletion in thermal ion surface flux onto the downstream hemisphere (Figure 5(b)) causes a similar depletion in the H<sub>2</sub>O sputtering rate at low latitudes. However, even near the downstream equator the sputtering rate obtained for perturbed fields still reaches  $R \approx 10^6 \text{ cm}^{-2} \text{ s}^{-1}$ . This is in contrast to a uniform field configuration, where the sputtering rate in this region is exactly zero (Figure 6(a)). Setting  $\theta = 0^\circ$  in equation (1) further reduces the H<sub>2</sub>O sputtering rate from thermal ions by up to an order of magnitude (Figure 6(c)) to the minimum possible value. However, the spatial distribution largely remains unaffected compared to the rates obtained with the actual incidence angles (Figure 6(b)).

In a uniform field configuration, the surface flux of energetic ( $5 \text{ keV} \leq E \leq 10 \text{ MeV}$ ) ions is nearly uniform across Europa’s surface, differing between any two locations by no more than one order of magnitude (Figure 5(c)). The large gyroradii of energetic ions ( $\approx 0.5R_E$  for 1 MeV S<sup>3+</sup>) allow them to impact every location on Europa’s surface, in-

cluding the downstream hemisphere between  $-30^\circ$  and  $30^\circ$  latitude which is inaccessible to the thermal ions in a uniform field setup (Figure 6(a) and Addison et al., 2021). The high field-aligned velocities of many energetic ions cause them to most heavily irradiate Europa's polar caps (Cassidy et al., 2013; Breer et al., 2019; Addison et al., 2021). As a result, the energetic ion surface flux monotonically decreases in the direction of descending latitude (Figure 5(c)), achieving a value at the equator that is roughly one order of magnitude lower than at the poles. A latitudinal decrease can also be seen in the  $\text{H}_2\text{O}$  sputtering rates of energetic ions in uniform fields (Figure 6(d)). Convection of energetic ions toward downstream leads to a slight enhancement in the energetic ion influx by approximately 20% near the upstream apex (Figure 5(c)) compared to the downstream equator. Thus, in the upstream hemisphere, the equatorial reduction in  $\text{H}_2\text{O}$  sputtering rate is interrupted by an elliptical enhancement of approximately 20% compared to the downstream equator.

Magnetic field line draping leads to a large, quasi-elliptical region of reduced energetic ion flux centered at Europa's upstream apex and covering much of the upstream hemisphere (see Figure 5(d), as well as Addison et al., 2021). The draping increases the latitudinal extent of the region near the moon where ions traveling along the field lines are within one gyroradius of the surface. Impinging ions can therefore gyrate into the moon at higher latitudes than in uniform fields (Addison et al., 2021), creating an influx depletion by approximately a factor of two near the upstream apex compared to the downstream equatorial region. Surprisingly, a similar depletion feature is *not* present in the energetic ion  $\text{H}_2\text{O}$  sputtering rate calculated with draped fields and the actual incidence angles from GENTOO (Figure 6(e)). Although the energetic ion flux is reduced near the upstream apex by a factor of three compared to the poles (Figure 5(d)), ions entering the interaction region along the draped field lines (mostly) encounter the near-equatorial surface with grazing trajectories, i.e., with incidence angles well over  $\theta = 45^\circ$  (Breer et al., 2019; Addison et al., 2021). Such grazing impacts result in substantial sputtering yields around the upstream apex (equation (1)), overcompensating the drop in incident ion flux and producing a slight enhancement of the  $\text{H}_2\text{O}$  sputtering rates in that region.

To further illustrate this mechanism, Figure 7 displays maps of the average incidence angles of impinging sulfur ions exposed to Europa's perturbed electromagnetic environment, with energies of 10 keV (panel (a)), 100 keV (panel (b)), and 1 MeV (panel

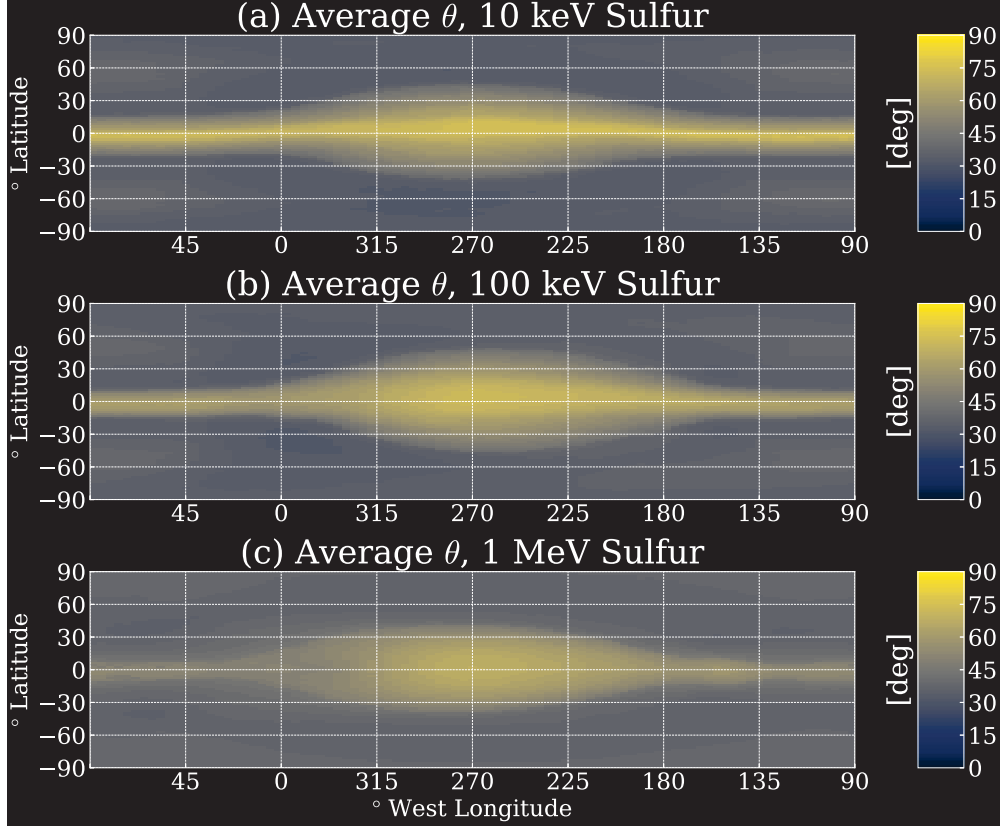


**Figure 7.** Maps of the average incidence angle  $\langle \theta \rangle$  of (a) 10 keV, (b) 100 keV, and (c) 1 MeV  $\text{S}^{3+}$  ions with allowed trajectories, calculated with the perturbed electromagnetic fields from AIKEF.

(c)). It can be seen that these sulfur ions impact the surface with high incidence angles exactly in the regions where the ion influx is low (Figure 5(d)). The resultant high sputtering yields of these ions are able to replenish the upstream flux depletion revealed by Figure 5(d). The result is that the energetic ion H<sub>2</sub>O sputtering rate in the upstream hemisphere is similar for uniform and perturbed fields. However, the mechanism behind this similarity is highly intricate. In the case of uniform fields, the drift motion of the energetic ions along the corotation direction causes the surface flux near the upstream apex to be roughly 20% higher than at the downstream equator, which leads to a sputtering rate around the upstream apex that is similarly enhanced. In contrast, field line draping *lowers* the flux near the upstream apex by a factor of two. However, the grazing trajectories of energetic ions which impact these regions generate substantial sputtering yields and compensate for the low surface flux.

When a constant impact angle of  $\theta = 0^\circ$  is used to calculate the H<sub>2</sub>O sputtering yields (analogous to Cassidy et al., 2013), the depletion in energetic ion flux around the upstream apex (Figure 5(d)) maps into the H<sub>2</sub>O sputtering rates (Figure 6(f)). In this case, the non-uniformity of ion incidence angles across Europa’s surface is truncated, and the sputtering rates assume their minimum value (regarding the angle dependence) everywhere on the surface. Ions precipitating along grazing trajectories are thus not able to compensate for the upstream depletion in energetic ion flux. The result is an “inverted bullseye” distribution in the upstream hemisphere, where the sputtering rate grows with distance from the upstream apex (Figure 6(f)).

The H<sub>2</sub>O sputtering rates of all ions and energies combined are shown in Figures 6(g)–6(i). In the case of uniform electromagnetic fields (Figure 6(g)), the spatial distribution of the total H<sub>2</sub>O sputtering rate is nearly rotationally symmetric about the  $x$  axis, and maximizes near the  $x = 0$  plane. The nearly homogeneous H<sub>2</sub>O sputtering rate from energetic ions (second row of Figure 6) uniformly augments that from thermal ions at all locations. Without the field perturbations, energetic ions are the sole agents of H<sub>2</sub>O sputtering on the downstream hemisphere between approximately  $-30^\circ$  and  $30^\circ$  latitude (which is inaccessible to upstream thermal ions in the case of uniform fields, see Figure 5(a)). The H<sub>2</sub>O sputtering rate on the downstream hemisphere is a factor of 2-3 less than the maximum value on the upstream hemisphere. When the fields are treated as uniform, H<sub>2</sub>O sputtering from thermal ions dominates at every point on the surface except mid-to-low latitudes on the downstream hemisphere (first column in Figure 6).

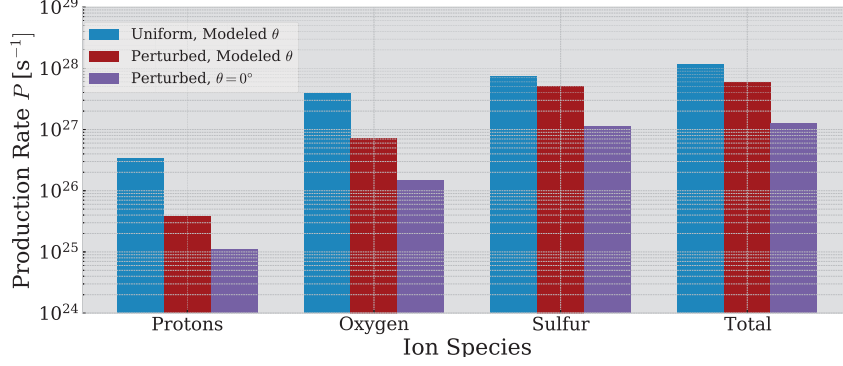


**Figure 8.** Total H<sub>2</sub>O production rate  $P$  for all ion energies and species modeled in this study. From left to right, production rates of incident hydrogen, oxygen, sulfur, and the combined production rates of all ion species are shown. The production rates calculated with uniform and perturbed electromagnetic fields are displayed in blue and red, respectively, both with sputtering yields calculated using the actual incidence angles from GENTOO in equation (1). Purple bars indicate production rates calculated with perturbed fields and the incidence angles of all impinging ions set to  $\theta = 0^\circ$  in equation (1).

However, with perturbed fields, the quasi-uniform H<sub>2</sub>O sputtering rate from energetic ions exceeds that from thermal ions at nearly every surface location except near the upstream apex (Figures 6(b) and 6(e)). The map of the total H<sub>2</sub>O sputtering rate from all ions and energies combined (Figure 6(h)) therefore closely resembles the nearly featureless pattern caused by energetic ion sputtering alone (Figure 6(e)). Comparison of Figures 6(b) and 6(e) reveals that the contribution of thermal ions to the total H<sub>2</sub>O sputtering rate equals that of the energetic ions only near the upstream apex, effectively doubling the energetic H<sub>2</sub>O sputtering rate there (red region in Figure 6(h)). This preferential emission of H<sub>2</sub>O molecules near the upstream apex agrees well with a recent study by Roth (2021), who used observed emission rates from HST to surmise the presence of a stable, localized H<sub>2</sub>O component of the exosphere above Europa's central trailing hemisphere.

For each species, the total amount of H<sub>2</sub>O sputtered from Europa's surface per time via magnetospheric ion impacts at all energies,  $P$ , is given by

$$P(m, Z) = R_E^2 \int_{-\pi/2}^{\pi/2} \int_0^{2\pi} R(m, Z, \lambda, \phi) \cos(\lambda) d\phi d\lambda, \quad (6)$$

where  $R(m, Z, \lambda, \phi)$  is the  $\text{H}_2\text{O}$  sputtering rate of a given species at a particular surface location  $(\lambda, \phi)$ . The resulting production rates from protons, oxygen ions, sulfur ions, and all ion species combined are displayed in Figure 8. Blue bars indicate production rates calculated with uniform electromagnetic fields and the incidence angles obtained from GENTOO, red bars indicate production rates calculated with perturbed fields and incidence angles from GENTOO, and purple bars show production rates calculated with perturbed fields and  $\theta$  set to  $0^\circ$  in equation (1) for all precipitating ions.

In all three setups presented in Figure 8, sulfur ions sputter the most  $\text{H}_2\text{O}$  per second, while oxygen ions and protons sputter successively less. This trend follows the hierarchy of the sputtering yield curves shown in Figure 1(a), revealing that the yields (not the surface fluxes) are the most important factor in determining the relative  $\text{H}_2\text{O}$  sputtering rate contributions between ion species. As shown by Addison et al. (2021), the surface fluxes of hydrogen ions exceed those of the two heavy ion species by up to an order of magnitude. However, due to their low mass, hydrogen ions play a negligible role in the sputtering of  $\text{H}_2\text{O}$  from Europa's surface (see Figure 1(a)). The surface fluxes of sulfur and oxygen ions differ by no more than a factor of five (Addison et al., 2021). However, since the sputtering yields of sulfur ions may exceed those of oxygen ions by over an order of magnitude (see Figure 1a), sulfur makes the largest contribution to the total  $\text{H}_2\text{O}$  production rate. In the case of uniform fields (blue bars in Figure 8), sulfur ions sputter roughly twice as much  $\text{H}_2\text{O}$  per second as oxygen ions ( $P \approx 7 \times 10^{27} \text{ s}^{-1}$  versus  $P \approx 4 \times 10^{27} \text{ s}^{-1}$ , respectively). Hydrogen ions sputter an order of magnitude less  $\text{H}_2\text{O}$  than either of the heavy ion species. We calculate a total  $\text{H}_2\text{O}$  production rate (from all three species) of  $P_T = 1.16 \times 10^{28} \text{ s}^{-1}$  in a uniform field configuration. Energetic sulfur ions generate the most  $\text{H}_2\text{O}$  per second (42% of  $P_T$ ), while thermal oxygen ions generate the second most (31%). Cassidy et al. (2013) found the same hierarchy of sputtering agents from their calculation of the total sputtering rates in uniform fields and with  $\theta = 0^\circ$  for all impinging ions (63% from energetic sulfur, 19% from thermal oxygen).

The  $\text{H}_2\text{O}$  production rate from sulfur ion impacts is reduced by only 10% when the field perturbations are considered, while the production rates associated with oxygen and hydrogen ions each fall by almost an order of magnitude (red bars, Figure 8). This discrepancy can be understood by isolating the contribution of the thermal and energetic regimes to each species' sputtering rate with perturbed fields. The high sputtering yields

of sulfur ions in the energetic regime (Figure 1(a)) allow the production rate from energetic sulfur ions ( $P = 4.9 \times 10^{27} \text{ s}^{-1}$ ) to exceed that from the thermal sulfur ions ( $P = 2.5 \times 10^{26} \text{ s}^{-1}$ ) by over an order of magnitude, despite the energetic sulfur ion surface flux being an order of magnitude lower (Addison et al., 2021). For oxygen, thermal ions produce 50% more  $\text{H}_2\text{O}$  per second than energetic ions ( $P = 4.38 \times 10^{26} \text{ s}^{-1}$  versus  $P = 2.9 \times 10^{26} \text{ s}^{-1}$ , respectively). The discrepancy for hydrogen ions is even more stark: thermal protons produce  $P = 3.58 \times 10^{25} \text{ s}^{-1}$ , while energetic protons produce only  $P = 2.3 \times 10^{24} \text{ s}^{-1}$ . In other words, sulfur is the only ion species that causes higher  $\text{H}_2\text{O}$  production rates in the energetic regime than in the thermal regime. Since the sputtering rates of energetic ions are much less affected by the perturbed fields (Figure 6), the sulfur ion contribution to the total production rate is much more “resilient” to the inclusion of the field perturbations than the contributions from hydrogen or oxygen, whose production rates are dominated by the thermal ions.

Of the thermal ion contribution to the total  $\text{H}_2\text{O}$  production rate  $P_T$  in perturbed fields, sulfur ions constitute 35%, oxygen ions constitute 60%, and protons add 5%. These values are in rough agreement with the 21%, 78%, and  $< 1\%$  contributions (for thermal sulfur, oxygen, and hydrogen ions, respectively) found by Cassidy et al. (2013) with uniform fields. The dominance of  $\text{H}_2\text{O}$  sputtering by thermal oxygen ions over the contribution from thermal sulfur stems from the slightly higher surface flux of oxygen (Addison et al., 2021). In the energetic regime, we find that sulfur ions contribute approximately 94% of  $\text{H}_2\text{O}$  production in perturbed fields, while oxygen ions and protons add 6% and  $< 1\%$ , respectively. The total production rate from all ions falls by about 50% to a value of  $P_T \approx 5.9 \times 10^{27} \text{ s}^{-1}$  when the field perturbations are included (blue versus red bars in the right-most block of Figure 8). Setting the incidence angles of all impinging ions to  $\theta = 0^\circ$  in equation (1) further reduces the  $\text{H}_2\text{O}$  production rate by a factor of 2-5, depending upon the ion species (purple bars in Figure 8). The total  $\text{H}_2\text{O}$  production rate from all ion species in the case of perturbed fields and  $\theta = 0^\circ$  falls to  $P_T = 1.27 \times 10^{27} \text{ s}^{-1}$ , which is a factor of five smaller than the rate calculated with the actual incidence angles from GENTOO.

Thus, inclusion of the perturbed fields reduces the total  $\text{H}_2\text{O}$  production rate at Europa by at least a factor of two compared to uniform fields (rightmost block in Figure 8). In addition, the perturbed fields significantly modify the spatial distribution of the  $\text{H}_2\text{O}$  sputtering rates (Figure 6). When the electromagnetic fields near Europa are



1301 treated as uniform, the corotating thermal plasma is unable to sputter material from the  
 1302 moon’s low-latitude downstream hemisphere, and the  $\text{H}_2\text{O}$  sputtering rate maximizes  
 1303 near the meridian through the moon’s sub-Jovian and anti-Jovian apices. With the in-  
 1304 clusion of the magnetospheric field perturbations, the distribution of the  $\text{H}_2\text{O}$  sputter-  
 1305 ing rate becomes much more homogeneous, besides a localized enhancement by up to  
 1306 an order of magnitude near the upstream apex. Except for this narrow region, the quasi-  
 1307 uniform  $\text{H}_2\text{O}$  sputtering rate of the energetic ions exceeds that of the thermal ions at ev-  
 1308 ery surface location. Therefore, in draped fields the energetic ions are able to “smear out”  
 1309 many of the non-uniformities in the thermal ion  $\text{H}_2\text{O}$  sputtering rate pattern.

### 1310 **3.3 Sputtering Rates of $\text{O}_2$ and $\text{H}_2$**

1311 We now investigate the temperature-dependent sputtering rates of  $\text{O}_2$  and  $\text{H}_2$  over  
 1312 the course of a European day ( $\approx 80$  hours), i.e., as the sub-solar point moves across the  
 1313 moon’s surface. Maps of the  $\text{H}_2$  sputtering rates will be qualitatively identical to those  
 1314 of  $\text{O}_2$ , since  $\text{H}_2$  sputtering rates are twice those of  $\text{O}_2$  (equation (4)). Therefore, for most  
 1315 of this section we will restrict our discussion to  $\text{O}_2$  sputtering rates. In section 3.3.1 we  
 1316 present sputtering rates calculated with the  $\text{O}_2$  sputtering yield model of Teolis et al.  
 1317 (2017), i.e., with the assumption that the  $\text{O}_2$  is concentrated in a “thin layer” approx-  
 1318 imately  $28 \text{ \AA}$  in depth (dash-dotted lines in Figures 1(b) and 1(c)). In section 3.3.2 we  
 1319 investigate  $\text{O}_2$  sputtering rates calculated with a “thick layer” model, i.e., with the as-  
 1320 sumption that the  $\text{O}_2$ -bearing layer within Europa’s surface extends to any depth to which  
 1321 a magnetospheric ion may penetrate. This model is shown as solid lines in Figures 1(b)  
 1322 and 1(c), and is adopted from Plainaki et al. (2013). In section 3.3.3 we compare the to-  
 1323 tal production rates of  $\text{O}_2$  from both models, and discuss their implications for the gen-  
 1324 eration of Europa’s exosphere.

#### 1325 **3.3.1 Contributions of Thermal and Energetic Ions in a “Thin Layer”** 1326 **Model**

1327 Figure 9 shows  $\text{O}_2$  sputtering rates from thermal (first column) and energetic (sec-  
 1328 ond column) ions impinging upon a thin  $\text{O}_2$  layer, i.e., calculated with equations (3) and  
 1329 (5). To isolate the effect of a non-uniform temperature profile on the  $\text{O}_2$  sputtering rates,  
 1330 the first row in Figure 9 (panels (a)–(b)) displays the spatial distribution of the  $\text{O}_2$  sput-  
 1331 tering rates calculated with a uniform surface temperature of  $T = 93 \text{ K}$ . This value of

$T$  was derived by averaging the diurnal temperature profile shown in Figure 3. In the case of a uniform surface temperature,  $\Phi(T)$  in equation (5) assumes the same constant value at all surface locations, i.e., the temperature dependence of the sputtering yields does not generate any changes to the spatial distribution of the  $O_2$  and  $H_2$  sputtering rates. The middle four rows (panels 9(c)–(j)) present maps of the  $O_2$  sputtering rates at the four local times for which temperature maps have been provided in Figure 2. The final row (panels 9(k) and 9(l)) shows  $O_2$  sputtering rates calculated with the diurnally-averaged temperature profile presented in Figure 3.

All sputtering rates shown in Figure 9 were calculated with the perturbed fields from AIKEF: the necessity to include these perturbations has been demonstrated in section 3.2 and numerous preceding publications. The angular dependence for  $O_2$  in a thin layer model (Teolis et al., 2017) is given by  $(1 - \exp[-r_0(E) \cos(\theta)/x_0]) \cos^{-1}(\theta)$ , see equation (5). Within the range of  $r_0(E)$  values used in our study, this term always results in an increase in  $O_2$  sputtering yields with increasing incidence angle, similar to  $H_2O$ . Therefore, in analogy to  $H_2O$  (middle vs. right columns of Figure 6), inclusion of the incidence angles from GENTOO (instead of a constant value) is expected to cause only subtle differences in the spatial distribution of the  $O_2$  sputtering rates, and will not alter the relative contributions of thermal and energetic ions. Hence, for our calculation of  $O_2$  sputtering rates we utilize the modeled incidence angles from GENTOO in equation (5).

The first column of Figure 9 reveals that the  $O_2$  sputtering rate from thermal ions peaks near the upstream apex, where the thermal ion flux is largest, and decreases with distance from the upstream apex as the surface influx drops (Figure 5(b)). The downstream hemisphere at low latitudes experiences substantially less  $O_2$  sputtering from thermal ions, with a sputtering rate 3–4 orders of magnitude lower than on the upstream hemisphere. Since the sputtering yields of  $H_2O$  and  $O_2$  both grow monotonically with increasing incidence angle, the  $O_2$  sputtering rate pattern from thermal ions resembles that of  $H_2O$  (Figure 6).

Changes in the orientation between the incoming solar radiation (and thus the surface temperature profile) and the upstream plasma flow cause slight qualitative modifications to the spatial distribution of the  $O_2$  sputtering rate from thermal ions (Figures 9(c), 9(e), 9(g), and 9(i)), compared to the “baseline” case of a constant surface temper-

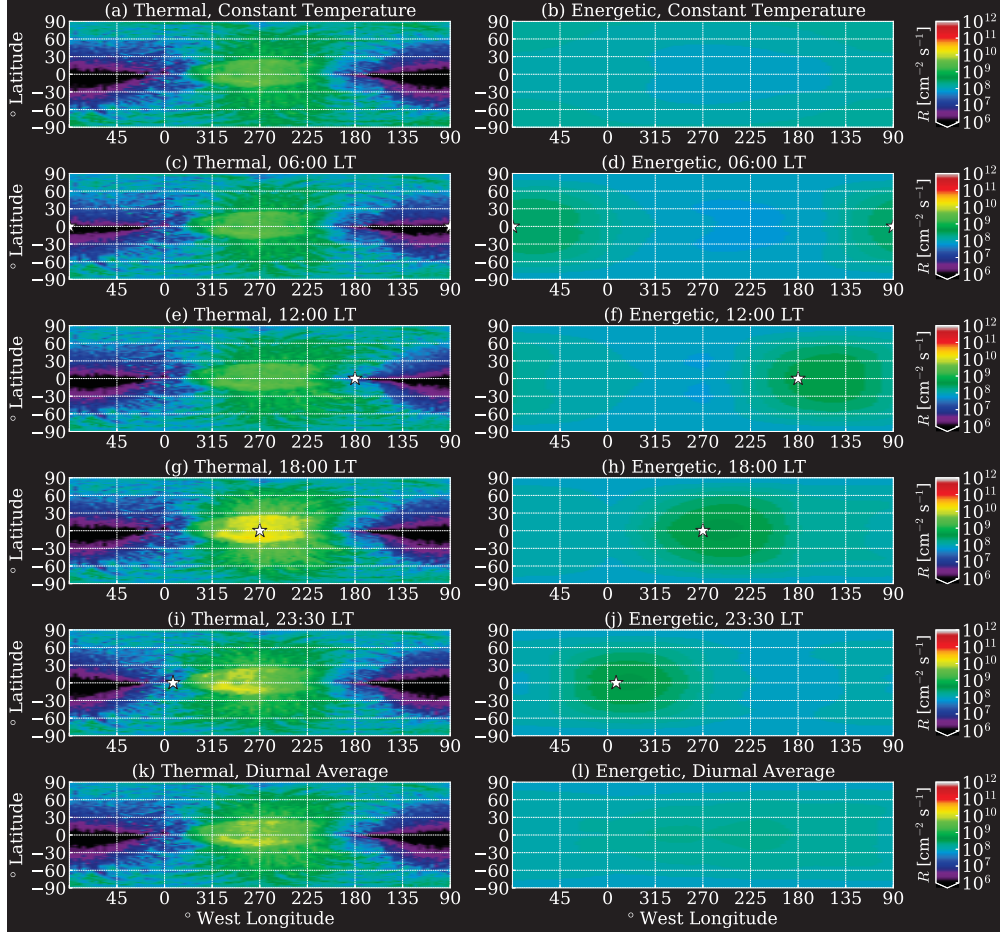


**Figure 9.** Maps of the O<sub>2</sub> sputtering rates from all ion species considered in this study, calculated with the perturbed electromagnetic fields from AIKEF and the actual incidence angles from GENTOO. The sputtering yields were calculated with a “thin layer” model of the oxygen-bearing surface layer (Teolis et al., 2017), i.e., with equation (5). The first column (panels (a), (c), (e), (g), (i), and (k)) displays the O<sub>2</sub> sputtering rates from thermal ion impacts, while the second column (panels (b), (d), (f), (h), (j), and (l)) shows O<sub>2</sub> sputtering rates from energetic ion impacts. To establish a “baseline” for our analysis, the first row (panels (a) and (b)) presents O<sub>2</sub> sputtering rates calculated with a uniform surface temperature of  $T = 93$  K. The next four rows show maps of the sputtering rates for different orbital positions of Europa, as illustrated in Figure 2: 06:00 LT (panels (c) and (d)), 12:00 LT (panels (e) and (f)), 18:00 LT (panels (g) and (h)), and 23:30 LT (panels (i) and (j)). In the plots which depict a specific local time (panels (c)–(j)), a white star is shown to denote the sub-solar point on Europa’s surface. Note that in panels (c) and (d), the star is divided between the leftmost and rightmost edges of the surface maps. The final row (panels (k) and (l)) presents maps of the O<sub>2</sub> sputtering rates calculated with a diurnally-averaged temperature profile (see Figure 3).

ature (Figure 9(a)). Within the range of surface temperatures present at Europa ( $\approx 60$ –  
140 K, see Figure 2), the temperature-dependent term  $\Phi(T)$  in equation (5) ranges from  
approximately  $10^{-2}$  to 7. As such, variations in the surface temperature profile along  
Europa’s orbit can (at most) enhance the  $\text{O}_2$  sputtering rate at a given point by a fac-  
tor of eight. Since the thermal ion surface flux varies by more than three orders of mag-  
nitude between surface locations, the shifting of the surface temperature profile along  
Europa’s orbit is not sufficient to qualitatively alter the  $\text{O}_2$  sputtering rate maps from  
thermal ions when the oxygen-bearing surface layer is thin.

For each of the orbital positions shown in Figure 9, the  $\text{O}_2$  sputtering rates drop  
slightly with increasing latitude, since Europa’s polar caps are consistently cold (Figures  
2 and 3). Movement of the sub-solar point (denoted by a star in the plots) across Eu-  
ropa’s surface quantitatively enhances the sputtering rate by a factor of 4-7, which is in-  
sufficient to noticeably alter the spatial distribution (left column of Figure 9). When the  
upstream apex and sub-solar point are coincident at 18:00 LT, the  $\text{O}_2$  sputtering rate  
from thermal ions near the upstream apex maximizes, as the thermal plasma directly  
impinges upon the hottest region of the moon’s surface (see also Figure 2). The surface  
near the sub-solar point in this configuration is hotter than at any other local time, since  
the low albedo at 18:00 LT causes it to heat to a maximum temperature that is roughly  
15% higher than when the sub-solar point is located on the downstream hemisphere (06:00  
LT). At 12:00 LT and 23:30 LT the sub-solar point is located near the moon’s anti-Jovian  
and sub-Jovian apices, respectively (Figures 9(e) and 9(i)), and the upstream enhance-  
ment in  $\text{O}_2$  sputtering rates is slightly “pulled” toward the sub-solar point, where the  
temperature and the resultant sputtering yields maximize. At these two orbital positions,  
the sub-solar enhancement in surface temperature, and therefore the enhancement in  $\text{O}_2$   
sputtering rates, is roughly a factor of two less than at 18:00 LT (Figure 9(g)).

Figure 9(k) displays the  $\text{O}_2$  sputtering rate from thermal ions calculated with a di-  
urnally averaged surface temperature profile (shown in Figure 3). The dichotomy in the  
surface temperatures between the upstream and downstream hemisphere in this case causes  
the map of the thermal ion  $\text{O}_2$  sputtering rate to qualitatively resemble that at 18:00  
LT (Figure 9(g)), although the upstream enhancement is a factor of two weaker. When  
the oxygen-bearing surface layer is thin, the chosen surface temperature profile does not  
significantly alter the map of the  $\text{O}_2$  sputtering rate from thermal ions. Regardless of

the temperature profile, the maps of the sputtering rates display similar patterns as the influx map for thermal magnetospheric ions (Figure 5(b)).

In contrast, the spatial distribution of the O<sub>2</sub> sputtering rate from energetic ion impacts is largely determined by the surface temperature profile, i.e., by the orientation of the Sun relative to Europa. The energetic ion sputtering rate for a constant surface temperature (Figure 9(b)) is nearly homogeneous, never varying between any two surface locations by more than a factor of two. A global minimum in the O<sub>2</sub> sputtering rate from energetic ions is present near the upstream apex, with the rate reduced by 35% compared to that near the poles (Figure 9(b)). Above incident ion energies of  $E = 10$  keV, the penetration depths of the ions are greater than the O<sub>2</sub> layer depth ( $x_0 = 28$  Å) even at an extreme grazing incidence of  $\theta = 80^\circ$  (Ziegler & Manoyan, 1988; Teolis et al., 2017). The angle-dependent exponential term in equation (5) is therefore nearly zero, and the sputtering yield is proportional to  $\cos^{-1}(\theta)$ . Hence, the O<sub>2</sub> sputtering yields around the upstream apex are less amplified by high incidence angles compared to the H<sub>2</sub>O yields, which are proportional to  $\cos^{-f(m)}(\theta)$  with  $f(m) > 1$  for all ion species. For example, the H<sub>2</sub>O sputtering yield of a  $\theta = 80^\circ$  incident sulfur ion is enhanced by a factor of  $\approx 21$  compared to normal incidence ( $\theta = 0^\circ$ ), while the O<sub>2</sub> yield of the same projectile would only be enhanced by a factor of  $\approx 6$ . As a result, the sputtering yields due to grazing impacts of energetic ions near the upstream apex are no longer able to compensate for the upstream flux depletion (Figure 5(d)), resulting in a net drop of the sputtering rate around the upstream apex. However, this upstream drop in the energetic ion O<sub>2</sub> sputtering rates is much smaller than the variability associated with the range of European surface temperatures.

At all four local times considered (Figures 9(d), 9(f), 9(h), and 9(j)), a quasi-elliptical enhancement in the O<sub>2</sub> sputtering rate forms near the sub-solar point. In each case, the maximum of the O<sub>2</sub> sputtering rate from energetic ions is displaced somewhat to the east of the sub-solar point, since the thermal inertia of Europa's surface slightly delays the surface heating. With a diurnally-averaged temperature profile, the map of the O<sub>2</sub> sputtering rates from energetic ions (Figure 9(l)) is nearly homogeneous, since the temperature enhancement covers a wider range of surface longitudes on the upstream hemisphere (see Figure 3).

In contrast to the case of sputtered H<sub>2</sub>O, thermal ions dominate the O<sub>2</sub> sputtering rate at almost every location on Europa’s upstream hemisphere (180–360° W longitude), regardless of the surface temperature profile (Figure 9). While the H<sub>2</sub>O sputtering yields of heavy ions grow by 3-4 orders of magnitude in the energetic regime compared to the thermal regime (equation (1) and Figure 1(a)), the respective O<sub>2</sub> yields increase by no more than two orders of magnitude. The energetic ions still penetrate more deeply into the surface than thermal ions. However, this increased penetration is largely ineffective at producing additional O<sub>2</sub> in the “thin layer” picture of Teolis et al. (2017), since the O<sub>2</sub> surface concentration quickly drops at greater depths. Thus, the O<sub>2</sub> sputtering yields of the energetic ions are insufficient for their sputtering rates to overcome those of the thermal ions on the upstream hemisphere, and the thermal ion O<sub>2</sub> sputtering rate dominates. This does not hold for the downstream hemisphere, however, where the thermal ion surface flux and the associated sputtering rates are several orders of magnitude lower than those of energetic ions. However, the energetic ion sputtering rate on the downstream hemisphere is still 1-2 orders of magnitude weaker than the upstream maximum.

### 3.3.2 Contributions of Thermal and Energetic Ions in a “Thick Layer” model

Figure 10 displays O<sub>2</sub> sputtering rates calculated with a “thick layer” model of the sputtering yields (Plainaki et al., 2013), i.e., with the assumption that the thickness of the O<sub>2</sub>-bearing layer within Europa’s surface exceeds the penetration depth of any incident magnetospheric ion. The associated yields are given in equation (2) and shown as solid lines in Figure 1(b).

The assumption of a thick oxygen-bearing surface layer does not significantly alter the qualitative distribution of the O<sub>2</sub> sputtering rates from thermal (left column of Figure 10) or energetic (right column of Figure 10) ions compared to when a thin layer is assumed (Figure 9). Recall that O<sub>2</sub> yields in both a thick-layer model and a thin-layer model grow with incidence angle, similar to the yields of H<sub>2</sub>O. Therefore, the quantitative behavior of the O<sub>2</sub> sputtering rates with respect to incidence angle is the same as for the H<sub>2</sub>O rates, regardless of O<sub>2</sub> layer thickness.

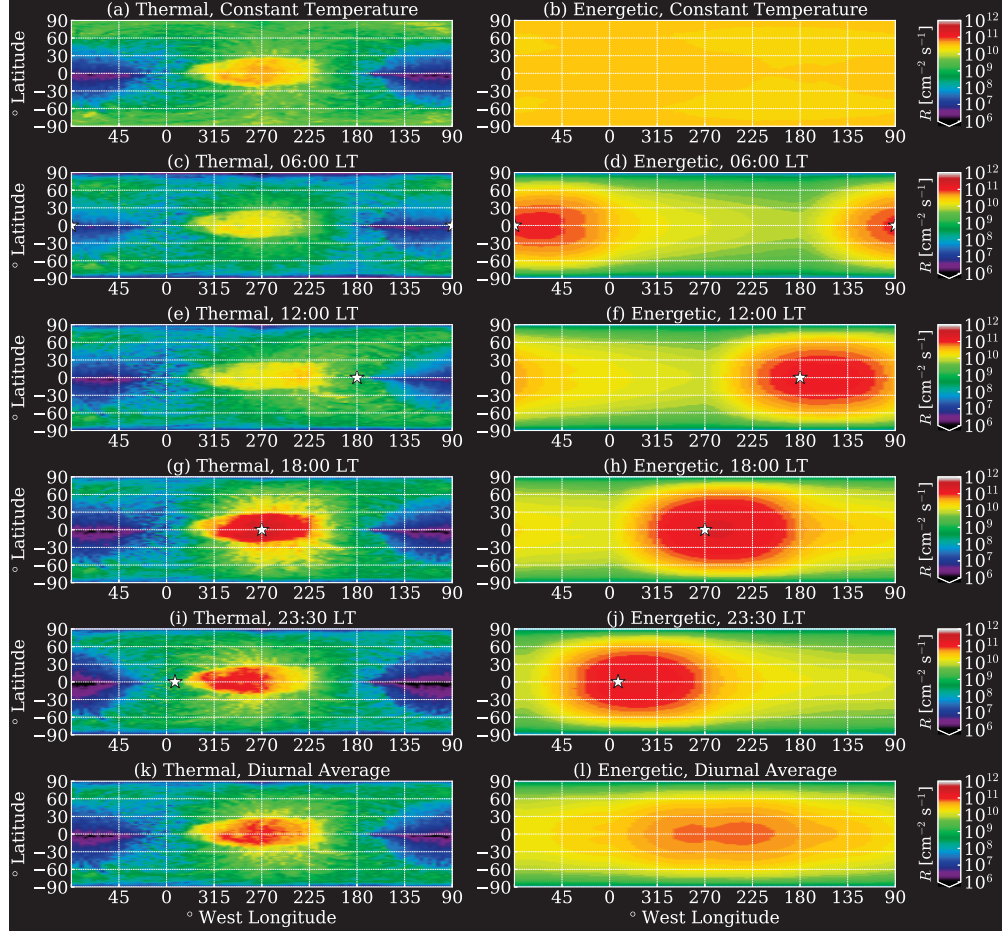


**Figure 10.** Maps of the  $\text{O}_2$  sputtering rates from all ion species considered in this study, calculated with the perturbed electromagnetic fields from AIKEF and the actual incidence angles from GENTOO. The sputtering yields were calculated with a “thick layer” model of the surface oxygen (Plainaki et al., 2013), i.e., with equation (2), depicted as solid lines in Figure 1(b). The layout of the panels is identical to Figure 9.



The difference between the temperature-dependent terms of the two O<sub>2</sub> sputtering models (thin layer and thick layer) becomes significant in regions of low surface temperatures, especially the polar caps. With a thin oxygen-bearing layer (Teolis et al., 2017), the temperature dependence takes the form of  $1+\Phi(T)$ , while with a thick layer (Plainaki et al., 2013) the dependence is given by only  $\Phi(T)$ . Thus, in both models the O<sub>2</sub> yields are independent of temperature below approximately 70 K, grow monotonically with temperature above 70 K, and eventually stagnate at very high temperatures. At the hottest regions of Europa's surface, the temperature dependencies of both models augment the sputtering yields by nearly the same factor. However, at low temperatures ( $\Phi(T) \approx 0$ ), the O<sub>2</sub> sputtering yields of Plainaki et al. (2013) approach a value of zero, while those of Teolis et al. (2017) approach a nonzero value. This discrepancy at low temperatures causes the two models to produce vastly different sputtering rates in cold surface regions (below 70 K). Since Europa's surface temperature (Figures 2 and 3) drops by a factor of two from the equator (100-140 K) to the poles ( $\approx 60$  K), the O<sub>2</sub> sputtering rates from thermal ions calculated with a thick oxygen-bearing layer fall by up to five orders of magnitude from the upstream equator to the poles (Figures 10(c), 10(e), 10(g), 10(i), 10(k)). In contrast, with a thin oxygen-bearing layer (Figure 9) the difference between the O<sub>2</sub> sputtering rates of thermal ions at the equator and the poles at any local time is limited to around three orders of magnitude. In the (hypothetical) case of a constant, averaged surface temperature the O<sub>2</sub> sputtering rates of thermal ions fall by at most two orders of magnitude from the equator to the poles (Figure 10(a)), and this decrease is caused purely by non-uniformities in the ion influx pattern. O<sub>2</sub> sputtering rates from energetic ions feature a similar behavior, falling by up to four orders of magnitude from the equator to the poles when a non-uniform temperature profile is included (Figures 10(d), 10(f), 10(h), 10(j), 10(l)). In contrast, the O<sub>2</sub> sputtering rates of energetic ions calculated with a constant temperature profile (Figure 10) do not decrease with increasing latitude. The consistently low temperatures of Europa's polar caps are therefore crucial to understanding exospheric generation at high latitudes.

In contrast to the thin layer model (Teolis et al., 2017), energetic ions in the thick layer model (Plainaki et al., 2013) can eject O<sub>2</sub> along their entire trajectory through the surface ice. As such, the O<sub>2</sub> sputtering yields of these ions dwarf those of the thermal ions by up to three orders of magnitude (Figure 1(b)). Hence, the O<sub>2</sub> sputtering rates of energetic ions in the picture of Plainaki et al. (2013) exceed those of the thermal ions



at nearly every surface location, regardless of the temperature profile (Figure 10). When the thick layer approach is used, the “roving” enhancement in energetic ion sputtering rates which follows the sub-solar point slightly exceeds that due to preferential thermal ion bombardment at the upstream apex.

The sputtering yields of thermal heavy ions in a thick layer approach exceed those in a thin layer approach by nearly an order of magnitude (solid vs. dash-dotted lines, Figure 1(b)). As can be seen from the left columns in Figures 9 and 10, this leads to the O<sub>2</sub> sputtering rates of thermal ions in a thick layer model surpassing those in a thin layer model by roughly an order of magnitude at almost every surface location. The deviation in the O<sub>2</sub> sputtering yields and rates of energetic ions between the two models is much more drastic, with the rates in a thick layer model typically exceeding those in a thin layer model by 2-3 orders of magnitude.

### 3.3.3 Total Sputtering and Neutral Gas Production Rates

Presented in Figure 11 are maps of the total O<sub>2</sub> sputtering rates from ions of all species and energies considered in this study. Rates calculated with the thin layer model of the O<sub>2</sub> sputtering yields (Teolis et al., 2017) are displayed in the first column, while results from the thick layer model (Plainaki et al., 2013) are shown in the second column. Similar to Figures 9 and 10, each row corresponds to a specific surface temperature profile, with the first row representing a constant, averaged temperature of  $T = 93$  K at all surface points, the next four rows corresponding to specific local times, and the final row denoting rates calculated with a diurnally-averaged temperature profile (Figure 3).

In the upstream hemisphere, the total O<sub>2</sub> sputtering rates calculated with a thin oxygen-bearing layer (left column of Figure 11) closely resemble the thermal ion rates (left column of Figure 9). The downstream depletion in the thermal ion sputtering rate is “filled in” by the energetic ion contribution (right column of Figure 9 and left column of Figure 11). Thus, the thermal ion contribution to O<sub>2</sub> sputtering dominates that of energetic ions on the upstream hemisphere, while the energetic ion contribution exceeds that of the thermal ions on much of the downstream hemisphere. This is in contrast to the H<sub>2</sub>O sputtering rate pattern, where the nearly homogeneous energetic ion sputtering rate dominates the thermal ion contribution at all surface locations except for a nar-

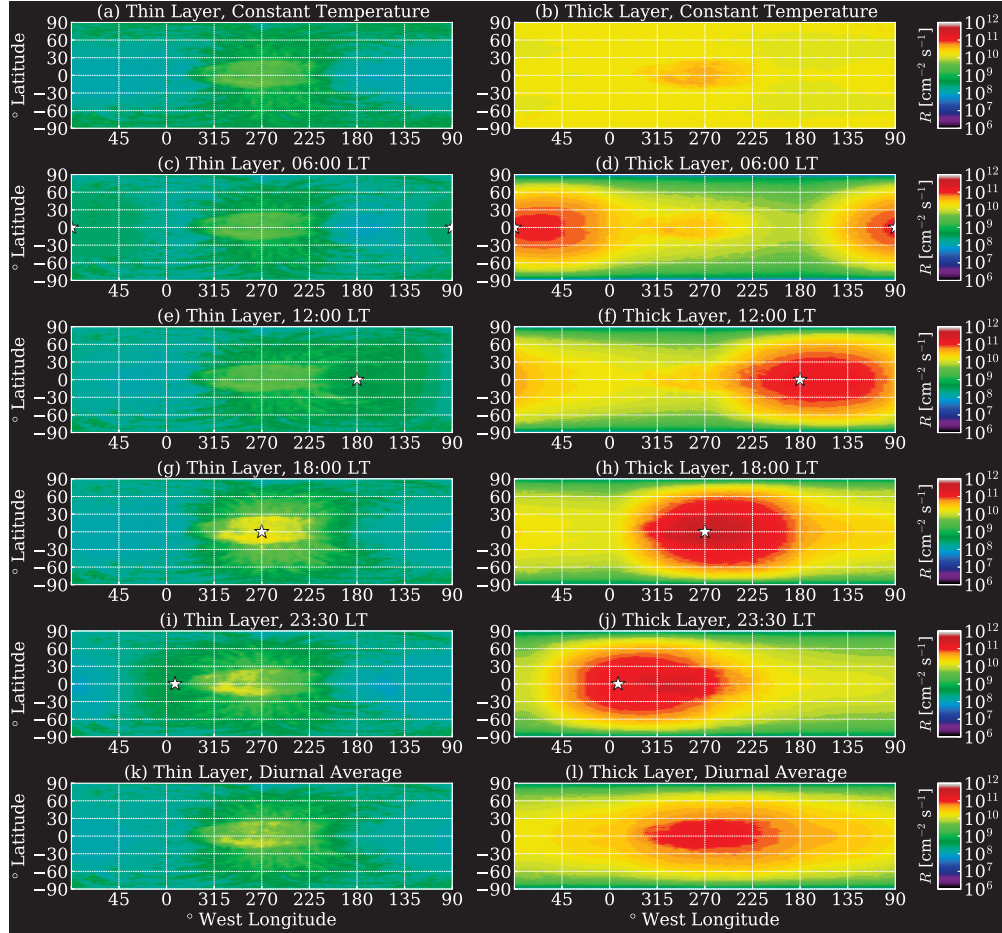


**Figure 11.** Maps of the total  $\text{O}_2$  sputtering rates from all ion species and energies considered in this study, calculated with the perturbed electromagnetic fields from AIKEF and the actual incidence angles from GENTOO. In the first column (panels (a), (c), (e), (g), (i), and (k)) are presented the  $\text{O}_2$  sputtering rates calculated with a “thin layer” model of the surface oxygen (equation (5)), while the second column (panels (b), (d), (f), (h), (j), and (l)) shows  $\text{O}_2$  sputtering rates from a “thick layer” model (equation (2)). The rows represent different surface temperature profiles, following the layout of Figures 9 and 10.

row region near the upstream apex (Figure 6(h)), since for H<sub>2</sub>O the energetic ion sputtering yields exceed those of thermal ions by several orders of magnitude.

The region of maximum O<sub>2</sub> generation in the thin layer approach is always located near the upstream apex, regardless of the solar orientation. Depending on the local time, the center of this enhancement is slightly displaced in longitude toward the sub-solar point (Figures 11(e) and 11(i)), as long as the sub-solar point is not located on the downstream side of the moon (Figure 11(c)). The maximum O<sub>2</sub> sputtering rate in the upstream hemisphere calculated with a thin oxygen-bearing layer ranges from  $R = 5.1 \times 10^9 \text{ cm}^{-2} \text{ s}^{-1}$  at 06:00 LT to  $R = 2.5 \times 10^{10} \text{ cm}^{-2} \text{ s}^{-1}$  at 18:00 LT.

For a thin layer model, the diurnally-averaged temperature profile yields a maximum O<sub>2</sub> sputtering rate (reached near the upstream apex) of approximately  $R = 1.1 \times 10^{10} \text{ cm}^{-2} \text{ s}^{-1}$ , a factor of four lower than predicted for uniform fields by Cassidy et al. (2013). These authors also utilized a diurnally-averaged temperature profile and a thin O<sub>2</sub>-bearing layer. However, Cassidy et al. (2013) treated all impinging ions as impacting normal to the surface ( $\theta = 0^\circ$ ). Therefore, these authors' sputtering rates constitute the minimum value possible with their choice of magnetospheric parameters (see also equation (5)). If Cassidy et al. (2013) had utilized actual incidence angles instead, their sputtering rates would be higher, and the discrepancy between their rates for uniform fields and those calculated here for draped fields would be even greater. The low sputtering rates obtained for draped fields in our model are consistent with the idea that the perturbations to the electromagnetic fields partially shield Europa's surface from magnetospheric ion bombardment (Breer et al., 2019; Addison et al., 2021; Harris et al., 2021; Simon et al., 2021).

Using a thin layer, our model predicts a minimum O<sub>2</sub> sputtering rate near the downstream apex (90° W) of  $R \approx 10^8 \text{ cm}^{-2} \text{ s}^{-1}$ . While this value is roughly two orders of magnitude lower than the peak value near the upstream apex, the occurrence of such substantial surface erosion in Europa's downstream hemisphere is in stark contrast to the results of Cassidy et al. (2013). Using uniform fields, these authors predicted a minimum sputtering rate of nearly zero on almost the *entire* downstream hemisphere (see Figure 9 of that paper). Therefore, if Europa's electromagnetic environment were perfectly uniform, any O<sub>2</sub> gas located above the downstream hemisphere would have to be transported there from the upstream hemisphere through, e.g., Coriolis or centrifugal

forces (Oza et al., 2019). However, with the inclusion of the perturbed fields in our model,  $\text{O}_2$  gas can be produced directly in the downstream hemisphere. As can be seen from the right column of Figure 11, this effect is amplified when the surface oxygen is assumed to occupy a thick layer (Plainaki et al., 2013).

In the thick layer picture, the energetic ions have substantial sputtering yields compared to a thin layer approach (right columns of Figures 9 and 10). This allows the energetic ions to become the dominant agents in determining the spatial distribution of the  $\text{O}_2$  source rate at Europa. When the surface temperature is treated as constant (Figure 11(b)), the  $\text{O}_2$  yields in a thick layer approach are simply the  $\text{H}_2\text{O}$  yields multiplied by the same, constant coefficient at every surface location (equation (2)). Therefore, if the surface temperature were uniform, the spatial distribution of the  $\text{O}_2$  sputtering rate would be largely homogeneous across Europa’s surface, with the bullseye-like “surplus” of thermal ion influx near the upstream apex (red in Figure 5(b)) generating the only significant local enhancement.

When a non-uniform temperature profile is used to calculate the  $\text{O}_2$  sputtering yields for a thick oxygen-bearing layer, the spatial distribution of the energetic ion  $\text{O}_2$  sputtering rate demonstrates a quasi-elliptical enhancement by a factor of five around the sub-solar point (Figures 10(d), 10(f), 10(h), and 10(j)). Since in this case the  $\text{O}_2$  sputtering rates from energetic ions exceed those from thermal ions at nearly every surface point, this sub-solar augmentation is also clearly visible in the total  $\text{O}_2$  rate maps (right column of Figure 11). At 06:00 LT (Figure 11(d)), this results in two distinct  $\text{O}_2$  sputtering maxima on Europa’s surface: the more pronounced one is centered near the sub-solar point at  $90^\circ$  W, whereas the fainter one (originating from the preferential precipitation of thermal ions near the upstream apex) is located near the upstream apex at  $270^\circ$  W. These two enhancements are still discernible, but also have substantial overlap at 12:00 LT and 23:30 LT (red regions in Figures 11(f) and 11(j)), since the sub-solar point is located only approximately  $90^\circ$  in longitude from the upstream apex. At 18:00 LT, the sub-plasma and sub-solar points are coincident, resulting in a single, quasi-elliptical enhancement by approximately an order of magnitude compared to the downstream apex. This enhancement ( $R \approx 5 \times 10^{11} \text{ cm}^{-2} \text{ s}^{-1}$ ) is over an order of magnitude greater than the maximum sputtering rate calculated with a thin layer at 18:00 LT, and marks the maximum  $\text{O}_2$  sputtering rate at any point along Europa’s orbit.

If the sputtering maxima from a thick layer model directly translated into local enhancements of the exospheric column density, this would imply that there may be two distinct “bulges” in Europa’s neutral gas envelope: a minor enhancement persistently located near the upstream apex, and a more pronounced increase that follows the region of greatest solar irradiation. This is in contrast to the results for a thin oxygen-bearing layer model, which predicts only one emission maximum for  $\text{O}_2$  molecules, consistently located near the upstream apex. However, investigating any potential exospheric asymmetries requires to take into account all relevant influences on the dynamics of the emitted gas molecules (e.g., gravitational and fictitious forces, collisions, ionization). Such an effort is beyond the scope of this study.

The total  $\text{O}_2$  production rates  $P$  from ions of all species and energies considered in this study are presented in Figure 12 for each of the five non-uniform temperature profiles shown in Figure 11. We do not include the case of a uniform surface temperature profile, as we do not expect this approach to generate accurate sputtering rates for Europa’s nightside hemisphere. Figure 12(a) displays production rates calculated with a thin  $\text{O}_2$ -bearing surface layer (equation (5)). Averaged across all four local times shown in Figure 12(a), oxygen ions produce roughly the same amount of  $\text{O}_2$  as sulfur ions (the averaged rates differ by only  $\approx 30\%$ ), whereas sulfur ions sputter nearly seven times more  $\text{H}_2\text{O}$  than oxygen ions (Figure 8). Regardless of the chosen sputtering model, the surface flux and  $\text{O}_2$  sputtering yields of the two heavy ion species are very similar in the thermal regime. Since thermal ions dominate the  $\text{O}_2$  sputtering rate in a thin layer model, the contributions of the two heavy ion species are nearly the same.

However, if the  $\text{O}_2$ -bearing surface layer is assumed to be thick (Figure 10), energetic ions make the greatest contribution to the total  $\text{O}_2$  sputtering rates at nearly every location on the surface. Hence, sulfur ions, which dominate the  $\text{O}_2$  sputtering yields in the energetic regime by up to an order of magnitude over oxygen ions (solid lines in Figure 1(b)), surpass the production rates of oxygen ions by at least an order of magnitude regardless of the temperature profile (second vs. third block in Figure 12(b)). Sulfur ions in a thick layer configuration (Figure 12(b)) produce approximately two orders of magnitude more  $\text{O}_2$  per second than when the  $\text{O}_2$ -bearing layer is thin (Figure 12(a)), while the discrepancies for oxygen and hydrogen ions are roughly an order of magnitude and a factor of 2-5, respectively. Thus, the thickness of the oxygen-bearing layer beneath

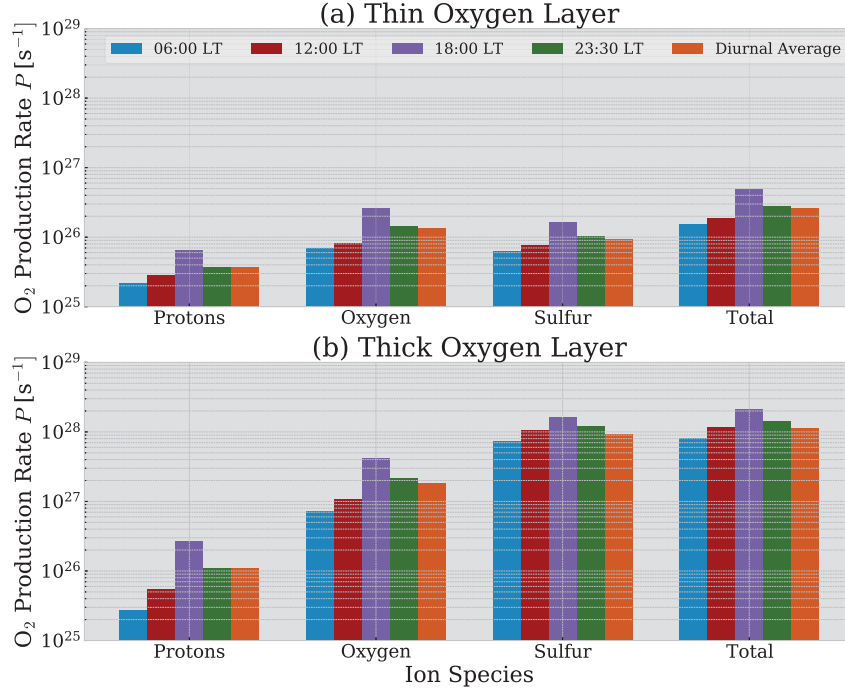


**Figure 12.**  $O_2$  production rates from impinging magnetospheric protons, oxygen ions, sulfur ions, and all species combined at all energies, calculated with a thin layer model (panel (a)), and a thick layer model (panel (b)) of the oxygen concentration within Europa's surface. The different colors denote different orbital positions: 06:00 LT (blue), 12:00 LT (red), 18:00 LT (purple), and 23:30 LT (green). Rates calculated with a diurnally-averaged temperature profile are shown in orange. The production rates of  $H_2$  are exactly twice those of  $O_2$  (see equation (4)).

Europa's surface has a measurable impact on the production, and likely the resulting density, of the moon's neutral gas envelope and the torus formed along its orbit.

This effect is particularly visible in the total O<sub>2</sub> production rates (rightmost blocks of Figures 12(a) and 12(b)), which differ drastically based upon the assumed thickness of the surface O<sub>2</sub>-bearing layer. For all five temperature profiles shown, the production rate calculated with a thick layer is nearly two orders of magnitude greater than that calculated with a thin layer. Depending upon the temperature profile used, the total O<sub>2</sub> production rate for a thin layer ranges from  $P_T = (1.5 \times 10^{26} - 4.9 \times 10^{26}) \text{ s}^{-1}$ , while the thick layer estimate ranges from  $P_T = (8.1 \times 10^{27} - 2.1 \times 10^{28}) \text{ s}^{-1}$ . Our modeled production rate for a thin layer agrees well with published estimates of the global neutral *escape* rate at Europa of  $\approx 1 \times 10^{26} \text{ s}^{-1}$  (Vorburger & Wurz, 2018) and  $\approx 2.7 \times 10^{26} \text{ s}^{-1}$  (Smyth & Marconi, 2006), which must be true for the exosphere to be in hydrostatic equilibrium. Dols et al. (2016) suggested that symmetric charge exchange reactions between picked-up O<sub>2</sub><sup>+</sup> ions and exospheric O<sub>2</sub> neutrals may increase the O<sub>2</sub> escape rate by up to an order of magnitude, arriving at a figure of  $P \approx 4 \times 10^{27} \text{ s}^{-1}$ . This value edges slightly closer to our thick layer estimate.

Cassidy et al. (2013) reported a global O<sub>2</sub> production rate of  $P_T = 1.0 \times 10^{26} \text{ s}^{-1}$  using uniform electromagnetic fields and the same thin oxygen layer model applied here. Thus, the combination of the field perturbations (which reduce the surface flux) and the actual incidence angles (which enhance the sputtering yields) in our model results in a similar estimate of  $P$  as a model setup that treats the fields as uniform and assumes a constant incidence angle of  $\theta = 0^\circ$  (Cassidy et al., 2013). When the field perturbations are included, the chosen treatment of the incidence angles does not substantially alter the *spatial distribution* of the sputtering rates. However, assuming normal incidence does reduce the rates to their minimum possible values at all surface locations (see also second vs. third column of Figure 6). Therefore, if our model was to utilize a constant incidence angle of  $\theta = 0^\circ$  for all impinging ions, our estimate of the total O<sub>2</sub> production rate would fall below that of Cassidy et al. (2013), due to the shielding effect of the electromagnetic field perturbations. Regardless of the integrated production rates, using uniform electromagnetic fields (Cassidy et al., 2013) leads to vastly different estimates as to where the most exospheric material is being ejected compared to perturbed fields. In other words, careful treatment of Europa's perturbed electromagnetic environment is mandatory to constrain, e.g., the location and extent of large-scale inhomogeneities in the moon's

exosphere. Precise knowledge on the properties of such exospheric inhomogeneities is critical for the ongoing search for transient water vapor plumes in plasma and magnetic field data (Jia et al., 2018; Arnold et al., 2019).

For both a thick and a thin oxygen-bearing layer the total production rate is affected by less than a factor of five when the surface temperature profile is altered (rightmost blocks of Figures 12(a) and 12(b)). In both cases, the  $O_2$  production maximizes at 18:00 LT, when the surface temperature reaches its maximum and the sub-plasma point coincides with the sub-solar point. The minimum production rate occurs at 06:00 LT for both sputtering yield models, since the surface is at its coolest and the dayside hemisphere is downstream (i.e., it is only weakly irradiated). For either model of the  $O_2$ -bearing surface layer thickness, the production rate at 18:00 LT exceeds that at 06:00 LT by a factor of approximately three. Therefore, while the assumption of a thick  $O_2$ -bearing layer markedly increases the  $O_2$  source rate compared to a thin layer, both assumptions result in a similar dependence of  $P$  on Europa's orbital position.

Sputtered  $O_2$  remains in Europa's exosphere for only a finite residence time before it is lost due to ionization or Jeans escape into the neutral torus (Smith et al., 2019). The average residence time of sputtered  $O_2$  in Europa's exosphere ( $\approx 1.4 \times 10^5$  s, Smyth and Marconi (2006)) allows for an estimation of the globally-averaged  $O_2$  column density, namely by multiplying the production rate  $P$  with the residence time and dividing by Europa's surface area  $4\pi R_E^2$ . Using this method we estimate an  $O_2$  column density of  $(6.9 \times 10^{13} - 2.2 \times 10^{14}) \text{ cm}^{-2}$  in a thin layer model, and  $(7.6 \times 10^{15} - 1.9 \times 10^{16}) \text{ cm}^{-2}$  for a thick layer. HST observations have assessed the column density of Europa's exosphere to be  $(2 \times 10^{14} - 6 \times 10^{14}) \text{ cm}^{-2}$  (Hall et al., 1998; Saur et al., 2011; Roth et al., 2016). Thus, our model indicates that a thick oxygen layer approach to  $O_2$  sputtering overestimates the observed  $O_2$  content of Europa's exosphere, whereas a thin oxygen layer approach is consistent with the observed exospheric column densities.

Since the sputtering yields (and resultant rates) of  $H_2$  are exactly twice those of  $O_2$  (equation (4)), the spatial distribution of the  $H_2$  sputtering rates is the same as that of  $O_2$ , regardless of the surface layer thickness. The production rates of  $H_2$  in a thin layer approach range from  $P_T = (3.0 \times 10^{26} - 9.8 \times 10^{26}) \text{ s}^{-1}$ , depending upon the local time, while those in a thick layer approach vary from  $P_T = (1.6 \times 10^{28} - 6.3 \times 10^{28}) \text{ s}^{-1}$ . Again combining our modeled production rates with the exospheric residence time of  $H_2$



( $1.2 \times 10^4$  s, Smyth & Marconi, 2006), we estimate an  $\text{H}_2$  column density of ( $2.9 \times 10^{12} - 9.6 \times 10^{12}$ )  $\text{cm}^{-2}$  with a thin layer, and ( $1.6 \times 10^{14} - 3.9 \times 10^{14}$ )  $\text{cm}^{-2}$  with a thick layer. Although the column density of molecular hydrogen in Europa's exosphere has not yet been constrained through observations, our estimated  $\text{H}_2$  column density calculated with a thin layer is in good agreement with exospheric modeling by Vorbuerger and Wurz (2018). These authors calculated a value of  $\approx 2.0 \times 10^{12} \text{ cm}^{-2}$ .

#### 4 Summary and Concluding Remarks

In this study, we have presented the first model of magnetospheric ion sputtering at Europa which takes into account the perturbations to the electromagnetic fields near the moon. To accomplish this, we have combined the electromagnetic fields from the AIKEF hybrid model (Arnold et al., 2019; Arnold, Liuzzo, & Simon, 2020; Arnold, Simon, & Liuzzo, 2020; Breer et al., 2019; Addison et al., 2021) with a variant of the GENTOO particle tracing model (Liuzzo et al., 2019a, 2019b, 2020; Breer et al., 2019; Addison et al., 2021) which has been expanded to calculate the contribution of impinging magnetospheric ions to surface sputtering. We have calculated maps of the sputtering rates of  $\text{H}_2\text{O}$ ,  $\text{O}_2$ , and  $\text{H}_2$ , the major exospheric constituents at Europa (e.g., Vorbuerger & Wurz, 2018; Roth et al., 2016; Roth, 2021) from the three dominant ion species in the moon's magnetospheric environment. To constrain the variations in the surface sputtering rate with solar orientation (European local time), we have examined the temperature-dependent  $\text{O}_2$  and  $\text{H}_2$  sputtering rates at four (near) equally-spaced locations of Europa along its orbit, as well as with a diurnally-averaged temperature profile. In addition, we have investigated how the thickness of the  $\text{O}_2$ -bearing layer within Europa's surface (Plainaki et al., 2013; Teolis et al., 2017) affects the spatial distribution of the sputtering rates. Finally, we have calculated the total  $\text{H}_2\text{O}$ ,  $\text{O}_2$ , and  $\text{H}_2$  production rates at Europa, as well as estimations of the corresponding exospheric  $\text{O}_2$  column densities, which agree well with observations by HST and the Galileo spacecraft.

Our major results are as follows:

1. The inclusion of the electromagnetic field perturbations near Europa substantially modifies the spatial distribution of  $\text{H}_2\text{O}$  sputtering rates across the surface. Compared to a uniform field model, the deflection of the impinging ions by the draped fields reduces the sputtering rate by up to two orders of magnitude across much

of the upstream hemisphere. Furthermore, substantial amounts of  $\text{H}_2\text{O}$ ,  $\text{O}_2$ , and  $\text{H}_2$  are sputtered from the downstream hemisphere when the field perturbations are taken into account, in contrast to a uniform field model which predicts zero sputtering in this region (Cassidy et al., 2013). Therefore, while a uniform field model would require redistribution of the sputtered gas in order to explain any substantial column density above the downstream hemisphere, deflection of the projectile ions by the perturbed fields allows for the direct generation of exospheric neutrals in this region. Thus, not only are the field perturbations affected by any asymmetries in Europa’s neutral gas envelope (e.g., Arnold et al., 2019), but—due to their influence on the trajectories of projectile ions—the field perturbations in turn play a key role in determining where such “bulges” in the moon’s exosphere are located.

2. The spatial distribution of the temperature-dependent  $\text{O}_2$  and  $\text{H}_2$  sputtering rates is largely determined by the thickness of the oxygen-bearing layer within Europa’s surface. If the oxygen-bearing layer is thin compared to the penetration depths of energetic ions, thermal ions dominate the  $\text{O}_2$  and  $\text{H}_2$  sputtering rates everywhere except low latitudes on the downstream hemisphere. Thus, the highest sputtering rates with a thin layer are persistently located near Europa’s upstream apex, regardless of the moon’s orbital position. However, if the oxygen-bearing surface layer is thick, the sputtering efficiency of energetic ions does not decrease with penetration depth, and energetic ions make the greatest contribution to the sputtering rate. The spatial distribution of the energetic ion sputtering rate is then determined almost exclusively by the surface temperature profile. Hence, with a thick oxygen-bearing layer the region of maximum  $\text{O}_2$  and  $\text{H}_2$  sputtering follows the sub-solar point as Europa orbits Jupiter. Therefore, depending on the moon’s orbital position, two enhancements in the sputtering rates may be present if the  $\text{O}_2$ -bearing surface layer is thick: one located near the sub-solar point (which moves along Europa’s equator as the moon orbits Jupiter), and a persistent, weaker enhancement near the upstream apex.
3. The total production rates of  $\text{O}_2$  and  $\text{H}_2$  vary as a function of Europa’s orbital position. The  $\text{O}_2$  production rate maximizes at 18:00 LT, when the Sun is illuminating the moon’s low-albedo, upstream hemisphere. The  $\text{O}_2$  production rate minimizes at 06:00 LT, when the dayside hemisphere is located on the moon’s brighter,

downstream face. Regardless of the thickness of the oxygen-bearing surface layer, the production rate at 18:00 LT exceeds that at 06:00 LT by a factor of approximately three.

4. Assuming the oxygen-bearing surface layer to be thin compared to the penetration depth of energetic ions reproduces the values of Europa’s exospheric column density, as observed by HST and the Galileo spacecraft. However, our estimated column densities do not take into account the redistribution of newly-sputtered molecules due to, e.g., gravitational and fictitious forces, nor the contribution of magnetospheric electrons to surface erosion.
5. The preferential ejection of  $\text{H}_2\text{O}$  molecules from a narrow region near the upstream apex, as revealed by our model, correlates well with the recent detection of a localized, persistent  $\text{H}_2\text{O}$  exosphere above Europa’s upstream apex by Roth (2021) using HST observations. In addition, particularly intense weathering of the upstream hemisphere in a quasi-ellipse centered near the upstream apex (see section 3.2) matches the low concentrations of  $\text{H}_2\text{O}$  ice observed in that region by the Earth-based *Very Large Telescope* (Ligier et al., 2016).

The analytical exosphere model used in AIKEF to determine the field perturbations near Europa includes a upstream-downstream asymmetry (see section 2.1 and, e.g., Addison et al., 2021). The upstream “bulge” in this model exosphere has a clearly discernible impact on the field perturbations near the moon (Arnold et al., 2019). However, our results for the sputtering rates suggest that the draped fields themselves play a critical role in determining the regions on Europa’s surface that are exposed to particularly intense erosion by magnetospheric ions. To achieve self-consistency, it would therefore be necessary to develop an improved exosphere model based on our calculated maps of the sputtering rates, subsequently use AIKEF to assess the influence of this modified neutral gas envelope on the electromagnetic fields, and then again update the ion surface fluxes and sputtering rates with GENTOO. This cycle would have to be repeated until convergence is achieved. However, such an exhaustive modeling effort is beyond the scope of the present study. In addition, our model has not considered the contribution of magnetospheric electrons to surface sputtering, which was recently suggested to be equal to, or even exceed, that of the ions (Vorbürger & Wurz, 2018; Davis et al., 2021). Modeling of electron surface bombardment requires treatment of the bounce motion of electrons between Europa’s local interaction region and Jupiter’s polar ionosphere (Paranicas

et al., 2009), as well as inclusion of relativistic mass growth of the electrons. This effort will be the subject of a future publication.

## Acknowledgments

The authors are grateful to the NASA Solar System Workings 2018 Program (Grant no. # 80NSSC20K0463) for financial support. The authors would also like to thank both referees for careful inspection of the manuscript and for valuable comments. Results from both the AIKEF hybrid model and the GENTOO particle-tracing model can be downloaded from <https://doi.org/10.5281/zenodo.5708206>.

## References

- Addison, P., Liuzzo, L., Arnold, H., & Simon, S. (2021). Influence of Europa's Time-Varying Electromagnetic Environment on Magnetospheric Ion Precipitation and Surface Weathering. *Journal of Geophysical Research: Space Physics*, 126(5), e2020JA029087. Retrieved from <https://agupubs.onlinelibrary.wiley.com/doi/abs/10.1029/2020JA029087> (e2020JA029087 2020JA029087) doi: <https://doi.org/10.1029/2020JA029087>
- Arnold, H., Liuzzo, L., & Simon, S. (2019). Magnetic Signatures of a Plume at Europa during the Galileo E26 Flyby. *Geophysical Research Letters*, 46(3), 1149–1157. doi: 10.1029/2018GL081544
- Arnold, H., Liuzzo, L., & Simon, S. (2020). Plasma Interaction Signatures of Plumes at Europa. *Journal of Geophysical Research: Space Physics*, 125(1), e2019JA027346. Retrieved from <https://agupubs.onlinelibrary.wiley.com/doi/abs/10.1029/2019JA027346> (e2019JA027346 10.1029/2019JA027346) doi: 10.1029/2019JA027346
- Arnold, H., Simon, S., & Liuzzo, L. (2020). Applying Ion Energy Spectrograms to Search for Plumes at Europa. *Journal of Geophysical Research: Space Physics*, n/a(n/a), e2020JA028376. Retrieved from <https://agupubs.onlinelibrary.wiley.com/doi/abs/10.1029/2020JA028376> (e2020JA028376 2020JA028376) doi: 10.1029/2020JA028376
- Bagenal, F., & Delamere, P. A. (2011). Flow of mass and energy in the magnetospheres of Jupiter and Saturn. *Journal of Geophysical Research (Space Physics)*, 116, A05209. doi: 10.1029/2010JA016294

- 1810 Bagenal, F., & Dols, V. (2020, May). The Space Environment of Io and Eu-  
1811 ropa. *Journal of Geophysical Research (Space Physics)*, 125(5), e27485. doi:  
1812 10.1029/2019JA027485
- 1813 Bagenal, F., Sidrow, E., Wilson, R. J., Cassidy, T. A., Dols, V., Crary, F. J., ...  
1814 Paterson, W. R. (2015). Plasma conditions at Europa's orbit. *Icarus*, 261, 1 -  
1815 13. Retrieved from [http://www.sciencedirect.com/science/article/pii/](http://www.sciencedirect.com/science/article/pii/S0019103515003413)  
1816 S0019103515003413 doi: <https://doi.org/10.1016/j.icarus.2015.07.036>
- 1817 Bagenal, F., Wilson, R. J., Siler, S., Paterson, W. R., & Kurth, W. S. (2016, May).  
1818 Survey of Galileo plasma observations in Jupiter's plasma sheet. *Journal of*  
1819 *Geophysical Research (Planets)*, 121(5), 871-894. doi: 10.1002/2016JE005009
- 1820 Bar-Nun, A., Herman, G., Rappaport, M. L., & Mekler, Y. (1985, Febru-  
1821 ary). Ejection of H<sub>2</sub>O, O<sub>2</sub>, H<sub>2</sub> and H from water ice by 0.5-6 keV H  
1822 <sup>+</sup> and Ne <sup>+</sup> ion bombardment. *Surface Science*, 150(1), 143-156. doi:  
1823 10.1016/0039-6028(85)90215-8
- 1824 Baragiola, R., Vidal, R., Svendsen, W., Schou, J., Shi, M., Bahr, D., & Atteberry,  
1825 C. (2003). Sputtering of water ice. *Nuclear Instruments and Methods in*  
1826 *Physics Research Section B: Beam Interactions with Materials and Atoms*,  
1827 209, 294-303. Retrieved from [https://www.sciencedirect.com/science/](https://www.sciencedirect.com/science/article/pii/S0168583X02020529)  
1828 article/pii/S0168583X02020529 (Fifth International Symposium on Swift  
1829 Heavy Ions in Matter) doi: [https://doi.org/10.1016/S0168-583X\(02\)02052-9](https://doi.org/10.1016/S0168-583X(02)02052-9)
- 1830 Bierhaus, E. B., Zahnle, K., & Chapman, C. R. (2009). Europa's Crater Distribu-  
1831 tions and Surface Ages. In R. T. Pappalardo, W. B. McKinnon, & K. K. Khu-  
1832 rana (Eds.), *Europa* (p. 161).
- 1833 Breer, B. R., Liuzzo, L., Arnold, H., Andersson, P. N., & Simon, S. (2019). En-  
1834 ergetic Ion Dynamics in the Perturbed Electromagnetic Fields near Eu-  
1835 ropa. *Journal of Geophysical Research (Space Physics)*, in press. doi:  
1836 10.1029/2019JA027147
- 1837 Brown, W. L., Augustyniak, W. M., Simmons, E., Marcantonio, K. J., Lanze-  
1838 rotti, L. J., Johnson, R. E., ... Pirronello, V. (1982, July). Erosion and  
1839 molecule formation in condensed gas films by electronic energy loss of fast  
1840 ions. *Nuclear Instruments and Methods in Physics Research*, 198(1), 1-8. doi:  
1841 10.1016/0167-5087(82)90043-6
- 1842 Brown, W. L., Lanzerotti, L. J., Poate, J. M., & Augustyniak, W. M. (1978,

- 1843 Apr). “Sputtering” of Ice by MeV Light Ions. *Physical Review Letters*,  
 1844 40, 1027–1030. Retrieved from [https://link.aps.org/doi/10.1103/](https://link.aps.org/doi/10.1103/PhysRevLett.40.1027)  
 1845 [PhysRevLett.40.1027](https://link.aps.org/doi/10.1103/PhysRevLett.40.1027) doi: 10.1103/PhysRevLett.40.1027
- 1846 Carlson, R. W., Anderson, M. S., Mehlman, R., & Johnson, R. E. (2005, October).  
 1847 Distribution of hydrate on Europa: Further evidence for sulfuric acid hydrate.  
 1848 *Icarus*, 177(2), 461–471. doi: 10.1016/j.icarus.2005.03.026
- 1849 Carlson, R. W., Calvin, W. M., Dalton, J. B., Hansen, G. B., Hudson, R. L.,  
 1850 Johnson, R. E., ... Moore, M. H. (2009). Europa’s Surface Composition.  
 1851 In R. T. Pappalardo, W. B. McKinnon, & K. K. Khurana (Eds.), *Europa*  
 1852 (p. 283).
- 1853 Carnielli, G., Galand, M., Leblanc, F., Modolo, R., Beth, A., & Jia, X. (2020).  
 1854 Simulations of ion sputtering at Ganymede. *Icarus*, 351, 113918. Re-  
 1855 trieved from [https://www.sciencedirect.com/science/article/pii/](https://www.sciencedirect.com/science/article/pii/S0019103520302967)  
 1856 [S0019103520302967](https://www.sciencedirect.com/science/article/pii/S0019103520302967) doi: <https://doi.org/10.1016/j.icarus.2020.113918>
- 1857 Cassidy, T., Coll, P., Raulin, F., Carlson, R. W., Johnson, R. E., Loeffler, M. J.,  
 1858 ... Baragiola, R. A. (2010, June). Radiolysis and Photolysis of Icy Satellite  
 1859 Surfaces: Experiments and Theory. *Space Science Reviews*, 153(1-4), 299–315.  
 1860 doi: 10.1007/s11214-009-9625-3
- 1861 Cassidy, T., & Johnson, R. (2005). Monte Carlo model of sputtering and  
 1862 other ejection processes within a regolith. *Icarus*, 176(2), 499–507. Re-  
 1863 trieved from [https://www.sciencedirect.com/science/article/pii/](https://www.sciencedirect.com/science/article/pii/S0019103505000813)  
 1864 [S0019103505000813](https://www.sciencedirect.com/science/article/pii/S0019103505000813) doi: <https://doi.org/10.1016/j.icarus.2005.02.013>
- 1865 Cassidy, T., Johnson, R. E., Geissler, P. E., & Leblanc, F. (2008). Simulation  
 1866 of Na D emission near Europa during eclipse. *Journal of Geophysical Re-*  
 1867 *search: Planets*, 113(E2). Retrieved from [https://agupubs.onlinelibrary](https://agupubs.onlinelibrary.wiley.com/doi/abs/10.1029/2007JE002955)  
 1868 [.wiley.com/doi/abs/10.1029/2007JE002955](https://agupubs.onlinelibrary.wiley.com/doi/abs/10.1029/2007JE002955) doi: [https://doi.org/10.1029/](https://doi.org/10.1029/2007JE002955)  
 1869 [2007JE002955](https://doi.org/10.1029/2007JE002955)
- 1870 Cassidy, T., Paranicas, C., Shirley, J., Dalton III, J., Teolis, B., Johnson, R., ...  
 1871 Hendrix, A. (2013). Magnetospheric ion sputtering and water ice grain size at  
 1872 Europa. *Planetary and Space Science*, 77, 64 – 73. Retrieved from [http://](http://www.sciencedirect.com/science/article/pii/S0032063312002024)  
 1873 [www.sciencedirect.com/science/article/pii/S0032063312002024](http://www.sciencedirect.com/science/article/pii/S0032063312002024) (Sur-  
 1874 faces, atmospheres and magnetospheres of the outer planets and their satellites  
 1875 and ring systems: Part VIII) doi: <https://doi.org/10.1016/j.pss.2012.07.008>

- Clark, G., Mauk, B. H., Kollmann, P., Paranicas, C., Bagenal, F., Allen, R. C.,  
 ... Westlake, J. H. (2020). Heavy ion charge states in Jupiter's polar mag-  
 netosphere inferred from auroral megavolt electric potentials. *Journal of*  
*Geophysical Research: Space Physics*, n/a(n/a), e2020JA028052. Retrieved  
 from [https://agupubs.onlinelibrary.wiley.com/doi/abs/10.1029/](https://agupubs.onlinelibrary.wiley.com/doi/abs/10.1029/2020JA028052)  
 2020JA028052 (e2020JA028052 2020JA028052) doi: 10.1029/2020JA028052
- Cooper, J. F., Johnson, R. E., Mauk, B. H., Garrett, H. B., & Gehrels, N. (2001).  
 Energetic Ion and Electron Irradiation of the Icy Galilean Satellites. *Icarus*,  
 149(1), 133 - 159. Retrieved from [http://www.sciencedirect.com/](http://www.sciencedirect.com/science/article/pii/S0019103500964984)  
 science/article/pii/S0019103500964984 doi: [https://doi.org/10.1006/](https://doi.org/10.1006/icar.2000.6498)  
 icar.2000.6498
- Coustenis, A., Tokano, T., Burger, M. H., Cassidy, T. A., Lopes, R. M., Lorenz,  
 R. D., ... Schubert, G. (2010, June). Atmospheric/Exospheric Charac-  
 teristics of Icy Satellites. *Space Science Reviews*, 153(1-4), 155-184. doi:  
 10.1007/s11214-009-9615-5
- Dalton, J. B., Cassidy, T., Paranicas, C., Shirley, J. H., Prockter, L. M., & Kamp,  
 L. W. (2013, March). Exogenic controls on sulfuric acid hydrate produc-  
 tion at the surface of Europa. *Planetary and Space Science*, 77, 45-63. doi:  
 10.1016/j.pss.2012.05.013
- Davis, M. R., Meier, R. M., Cooper, J. F., & Loeffler, M. J. (2021, feb). The  
 Contribution of Electrons to the Sputter-produced O<sub>2</sub> Exosphere on Europa.  
*The Astrophysical Journal*, 908(2), L53. Retrieved from [https://doi.org/](https://doi.org/10.3847/2041-8213/abe415)  
 10.3847/2041-8213/abe415 doi: 10.3847/2041-8213/abe415
- Dols, V. J., Bagenal, F., Cassidy, T. A., Cray, F. J., & Delamere, P. A. (2016).  
 Europa's atmospheric neutral escape: Importance of symmetrical O<sub>2</sub>  
 charge exchange. *Icarus*, 264, 387-397. Retrieved from [https://](https://www.sciencedirect.com/science/article/pii/S0019103515004315)  
 www.sciencedirect.com/science/article/pii/S0019103515004315 doi:  
<https://doi.org/10.1016/j.icarus.2015.09.026>
- Eviatar, A., Bar-Nun, A., & Podolak, M. (1985, February). European surface phe-  
 nomena. *Icarus*, 61(2), 185-191. doi: 10.1016/0019-1035(85)90100-9
- Famá, M., Shi, J., & Baragiola, R. (2008). Sputtering of ice by low-energy  
 ions. *Surface Science*, 602(1), 156-161. Retrieved from [https://](https://www.sciencedirect.com/science/article/pii/S0039602807009879)  
 www.sciencedirect.com/science/article/pii/S0039602807009879 doi:

- 1909 <https://doi.org/10.1016/j.susc.2007.10.002>
- 1910 Feyerabend, M., Simon, S., Motschmann, U., & Liuzzo, L. (2015). Filamented ion  
1911 tail structures at Titan: A hybrid simulation study. *Planet. Space Sci.*, *117*,  
1912 362–376. doi: 10.1016/j.pss.2015.07.008
- 1913 Feyerabend, M., Simon, S., Neubauer, F. M., Motschmann, U., Bertucci, C., Edberg,  
1914 N. J. T., ... Kurth, W. S. (2016). Hybrid simulation of Titan’s interaction  
1915 with the supersonic solar wind during Cassini’s T96 flyby. *Geophys. Res. Lett.*,  
1916 *43*(1), 35–42. doi: 10.1002/2015GL066848
- 1917 Gibbs, K. M., Brown, W. L., & Johnson, R. E. (1988, Dec). Electronic sputtering  
1918 of condensed O<sub>2</sub>. *Phys. Rev. B*, *38*, 11001–11007. Retrieved from [https://](https://link.aps.org/doi/10.1103/PhysRevB.38.11001)  
1919 [link.aps.org/doi/10.1103/PhysRevB.38.11001](https://link.aps.org/doi/10.1103/PhysRevB.38.11001) doi: 10.1103/PhysRevB.38  
1920 .11001
- 1921 Hall, D. T., Feldman, P. D., McGrath, M. A., & Strobel, D. F. (1998, may). The  
1922 Far-Ultraviolet Oxygen Airglow of Europa and Ganymede. , *499*(1), 475–481.  
1923 Retrieved from <https://doi.org/10.1086/305604> doi: 10.1086/305604
- 1924 Hall, D. T., Strobel, D. F., Feldman, P. D., McGrath, M. A., & Weaver, H. A.  
1925 (1995). Detection of an oxygen atmosphere on Jupiter’s moon Europa. *Nature*,  
1926 *373*(6516), 677–679. Retrieved from <https://doi.org/10.1038/373677a0>  
1927 doi: 10.1038/373677a0
- 1928 Harris, C. D. K., Jia, X., Slavin, J. A., Toth, G., Huang, Z., & Rubin, M.  
1929 (2021). Multi-Fluid MHD Simulations of Europa’s Plasma Interaction  
1930 Under Different Magnetospheric Conditions. *Journal of Geophysical Re-*  
1931 *search: Space Physics*, *126*(5), e2020JA028888. Retrieved from [https://](https://agupubs.onlinelibrary.wiley.com/doi/abs/10.1029/2020JA028888)  
1932 [agupubs.onlinelibrary.wiley.com/doi/abs/10.1029/2020JA028888](https://agupubs.onlinelibrary.wiley.com/doi/abs/10.1029/2020JA028888)  
1933 (e2020JA028888 2020JA028888) doi: <https://doi.org/10.1029/2020JA028888>
- 1934 Hendrix, A. R., Cassidy, T. A., Johnson, R. E., Paranicas, C., & Carlson, R. W.  
1935 (2011, Academic Press). Europa’s disk-resolved ultraviolet spectra: Relation-  
1936 ships with plasma flux and surface terrains. *Icarus*, *212*(2), 736–743. doi:  
1937 10.1016/j.icarus.2011.01.023
- 1938 Hill, T. W., & Michel, F. C. (1976). Heavy ions from the Galilean satellites and  
1939 the centrifugal distortion of the Jovian magnetosphere. *Journal of Geophys-*  
1940 *ical Research (1896-1977)*, *81*(25), 4561–4565. Retrieved from [https://](https://agupubs.onlinelibrary.wiley.com/doi/abs/10.1029/JA081i025p04561)  
1941 [agupubs.onlinelibrary.wiley.com/doi/abs/10.1029/JA081i025p04561](https://agupubs.onlinelibrary.wiley.com/doi/abs/10.1029/JA081i025p04561)



- doi: 10.1029/JA081i025p04561
- Huybrighs, H. L. F., Roussos, E., Blöcker, A., Krupp, N., Futaana, Y., Barabash, S., ... Witasse, O. (2020). An Active Plume Eruption on Europa During Galileo Flyby E26 as Indicated by Energetic Proton Depletions. *Geophysical Research Letters*, 47(10), e2020GL087806. Retrieved from <https://agupubs.onlinelibrary.wiley.com/doi/abs/10.1029/2020GL087806> (e2020GL087806 10.1029/2020GL087806) doi: 10.1029/2020GL087806
- Jia, X., Kivelson, M. G., Khurana, K. K., & Kurth, W. S. (2018). Evidence of a plume on Europa from Galileo magnetic and plasma wave signatures. *Nature Astronomy*, 2(6), 459-464. Retrieved from <https://doi.org/10.1038/s41550-018-0450-z> doi: 10.1038/s41550-018-0450-z
- Johnson, R. E. (1996, January). Sputtering of ices in the outer solar system. *Reviews of Modern Physics*, 68(1), 305-312. doi: 10.1103/RevModPhys.68.305
- Johnson, R. E., Burger, M. H., Cassidy, T. A., Leblanc, F., Marconi, M., & Smyth, W. H. (2009). Composition and Detection of Europa's Sputter-induced Atmosphere. In R. T. Pappalardo, W. B. McKinnon, & K. K. Khurana (Eds.), *Europa* (p. 507).
- Johnson, R. E., Carlson, R. W., Cooper, J. F., Paranicas, C., Moore, M. H., & Wong, M. C. (2004). Radiation effects on the surfaces of the Galilean satellites. In F. Bagenal, T. E. Dowling, & W. B. McKinnon (Eds.), *Jupiter. the planet, satellites and magnetosphere* (Vol. 1, p. 485-512).
- Johnson, R. E., Cooper, P. D., Quickenden, T. I., Grieves, G. A., & Orlando, T. M. (2005, November). Production of oxygen by electronically induced dissociations in ice. *Journal of Chemical Physics*, 123(18), 184715-184715. doi: 10.1063/1.2107447
- Kabin, K., Combi, M. R., Gombosi, T. I., Nagy, A. F., DeZeeuw, D. L., & Powell, K. G. (1999). On Europa's magnetospheric interaction: A MHD simulation of the E4 flyby. *J. Geophys. Res.*, 104(A9), 19983-19992, doi = 10.1029/1999JA900263.
- Kattenhorn, S. A., & Hurford, T. (2009). Tectonics of Europa. In R. T. Pappalardo, W. B. McKinnon, & K. K. Khurana (Eds.), *Europa* (p. 199).
- Khurana, K. K., & Kivelson, M. G. (1993). Inference of the angular velocity of plasma in the Jovian magnetosphere from the sweepback of magnetic field.

- 1975 *Journal of Geophysical Research: Space Physics*, 98(A1), 67-79. Retrieved  
1976 from [https://agupubs.onlinelibrary.wiley.com/doi/abs/10.1029/](https://agupubs.onlinelibrary.wiley.com/doi/abs/10.1029/92JA01890)  
1977 92JA01890 doi: 10.1029/92JA01890
- 1978 Kim, T. K., Ebert, R. W., Valek, P. W., Allegrini, F., McComas, D. J., Bage-  
1979 nal, F., ... Bolton, S. J. (2020). Survey of Ion Properties in Jupiter's  
1980 Plasma Sheet: Juno JADE-I Observations. *Journal of Geophysical Re-*  
1981 *search: Space Physics*, 125(4), e2019JA027696. Retrieved from [https://](https://agupubs.onlinelibrary.wiley.com/doi/abs/10.1029/2019JA027696)  
1982 [agupubs.onlinelibrary.wiley.com/doi/abs/10.1029/2019JA027696](https://agupubs.onlinelibrary.wiley.com/doi/abs/10.1029/2019JA027696)  
1983 (e2019JA027696 10.1029/2019JA027696) doi: 10.1029/2019JA027696
- 1984 Kivelson, M. G., Khurana, K. K., Russell, C. T., Volwerk, M., Walker, R. J., & Zim-  
1985 mer, C. (2000). Galileo Magnetometer Measurements: A Stronger Case for  
1986 a Subsurface Ocean at Europa. *Science*, 289(5483), 1340-1343. Retrieved  
1987 from <https://science.sciencemag.org/content/289/5483/1340> doi:  
1988 10.1126/science.289.5483.1340
- 1989 Kivelson, M. G., Khurana, K. K., Stevenson, D. J., Bennett, L., Joy, S., Russell,  
1990 C. T., ... Polanskey, C. (1999). Europa and Callisto: Induced or intrin-  
1991 sic fields in a periodically varying plasma environment. *J. Geophys. Res.*,  
1992 104(A3), 4609-4626, doi = 10.1029/1998JA900095.
- 1993 Kivelson, M. G., Khurana, K. K., & Volwerk, M. (2009). Europa's Interaction  
1994 with the Jovian Magnetosphere. In R. T. Pappalardo, W. B. McKinnon, &  
1995 K. K. Khurana (Eds.), *Europa* (p. 545).
- 1996 Kollmann, P., Paranicas, C., Clark, G., Roussos, E., Lagg, A., & Krupp, N. (2016).  
1997 The vertical thickness of Jupiter's Europa gas torus from charged particle  
1998 measurements. *Geophysical Research Letters*, 43(18), 9425-9433. Retrieved  
1999 from [https://agupubs.onlinelibrary.wiley.com/doi/abs/10.1002/](https://agupubs.onlinelibrary.wiley.com/doi/abs/10.1002/2016GL070326)  
2000 2016GL070326 doi: 10.1002/2016GL070326
- 2001 Krupp, N., Kotova, A., Roussos, E., Simon, S., Liuzzo, L., Paranicas, C., ...  
2002 Jones, G. H. (2020). Magnetospheric Interactions of Saturn's Moon  
2003 Dione (2005-2015). *Journal of Geophysical Research: Space Physics*,  
2004 125(6), e2019JA027688. Retrieved from [https://agupubs.onlinelibrary](https://agupubs.onlinelibrary.wiley.com/doi/abs/10.1029/2019JA027688)  
2005 [.wiley.com/doi/abs/10.1029/2019JA027688](https://agupubs.onlinelibrary.wiley.com/doi/abs/10.1029/2019JA027688) (e2019JA027688  
2006 10.1029/2019JA027688) doi: <https://doi.org/10.1029/2019JA027688>
- 2007 Lagg, A., Krupp, N., Woch, J., & Williams, D. J. (2003). In-situ observations

2008 of a neutral gas torus at Europa. *Geophysical Research Letters*, 30(11).  
2009 Retrieved from [https://agupubs.onlinelibrary.wiley.com/doi/abs/](https://agupubs.onlinelibrary.wiley.com/doi/abs/10.1029/2003GL017214)  
2010 10.1029/2003GL017214 doi: 10.1029/2003GL017214

2011 Ligier, N., Poulet, F., Carter, J., Brunetto, R., & Gourgéot, F. (2016, June).  
2012 VLT/SINFONI Observations of Europa: New Insights into the Surface Composi-  
2013 tion. *The Astrophysical Journal*, 151(6), 163. doi: 10.3847/0004-6256/151/6/  
2014 163

2015 Liuzzo, L., Feyerabend, M., Simon, S., & Motschmann, U. (2015). The impact  
2016 of Callisto's atmosphere on its plasma interaction with the Jovian magneto-  
2017 sphere. *Journal of Geophysical Research: Space Physics*, 120(11), 9401-9427.  
2018 Retrieved from [https://agupubs.onlinelibrary.wiley.com/doi/abs/](https://agupubs.onlinelibrary.wiley.com/doi/abs/10.1002/2015JA021792)  
2019 10.1002/2015JA021792 doi: 10.1002/2015JA021792

2020 Liuzzo, L., Paty, C., Cochrane, C., Nordheim, T., Luspay-Kuti, A., Castillo-Rogez,  
2021 J., ... Prockter, L. (2021). Triton's Variable Interaction With Neptune's Mag-  
2022 netospheric Plasma. *Journal of Geophysical Research: Space Physics*, 126(11),  
2023 e2021JA029740. Retrieved from [https://agupubs.onlinelibrary.wiley](https://agupubs.onlinelibrary.wiley.com/doi/abs/10.1029/2021JA029740)  
2024 .com/doi/abs/10.1029/2021JA029740 (e2021JA029740 2021JA029740) doi:  
2025 <https://doi.org/10.1029/2021JA029740>

2026 Liuzzo, L., Poppe, A. R., Halekas, J. S., Simon, S., & Cao, X. (2021). Investigating  
2027 the Moon's Interaction With the Terrestrial Magnetotail Lobe Plasma. *Geo-*  
2028 *physical Research Letters*, 48(9), e2021GL093566. Retrieved from [https://](https://agupubs.onlinelibrary.wiley.com/doi/abs/10.1029/2021GL093566)  
2029 [agupubs.onlinelibrary.wiley.com/doi/abs/10.1029/2021GL093566](https://agupubs.onlinelibrary.wiley.com/doi/abs/10.1029/2021GL093566)  
2030 (e2021GL093566 2021GL093566) doi: <https://doi.org/10.1029/2021GL093566>

2031 Liuzzo, L., Poppe, A. R., Paranicas, C., Nénon, Q., Fatemi, S., & Simon, S. (2020).  
2032 Variability in the energetic electron bombardment of Ganymede. *Journal of*  
2033 *Geophysical Research: Space Physics*, n/a(n/a), e2020JA028347. Retrieved  
2034 from [https://agupubs.onlinelibrary.wiley.com/doi/abs/10.1029/](https://agupubs.onlinelibrary.wiley.com/doi/abs/10.1029/2020JA028347)  
2035 2020JA028347 (e2020JA028347 2020JA028347) doi: 10.1029/2020JA028347

2036 Liuzzo, L., Simon, S., & Feyerabend, M. (2018). Observability of Callisto's In-  
2037 ductive Signature During the Jupiter ICy Moons Explorer Mission. *Jour-*  
2038 *nal of Geophysical Research: Space Physics*, 123(11), 9045-9054. Retrieved  
2039 from [https://agupubs.onlinelibrary.wiley.com/doi/abs/10.1029/](https://agupubs.onlinelibrary.wiley.com/doi/abs/10.1029/2018JA025951)  
2040 2018JA025951 doi: 10.1029/2018JA025951

- Liuzzo, L., Simon, S., Feyerabend, M., & Motschmann, U. (2016). Disentangling plasma interaction and induction signatures at Callisto: The Galileo C10 flyby. *Journal of Geophysical Research: Space Physics*, 121(9), 8677-8694. Retrieved from <https://agupubs.onlinelibrary.wiley.com/doi/abs/10.1002/2016JA023236> doi: 10.1002/2016JA023236
- Liuzzo, L., Simon, S., Feyerabend, M., & Motschmann, U. (2017). Magnetic signatures of plasma interaction and induction at Callisto: The Galileo C21, C22, C23, and C30 flybys. *Journal of Geophysical Research: Space Physics*, 122(7), 7364-7386. Retrieved from <https://agupubs.onlinelibrary.wiley.com/doi/abs/10.1002/2017JA024303> doi: 10.1002/2017JA024303
- Liuzzo, L., Simon, S., & Regoli, L. (2019a, December). Energetic electron dynamics near Callisto. *Planetary and Space Science*, 179, 104726. Retrieved from <http://www.sciencedirect.com/science/article/pii/S0032063319302430> doi: <https://doi.org/10.1016/j.pss.2019.104726>
- Liuzzo, L., Simon, S., & Regoli, L. (2019b, February). Energetic ion dynamics near Callisto. *Planet. Space Sci.*, 166, 23–53. doi: 10.1016/j.pss.2018.07.014
- Mauk, B. H., Mitchell, D. G., McEntire, R. W., Paranicas, C. P., Roelof, E. C., Williams, D. J., ... Lagg, A. (2004). Energetic ion characteristics and neutral gas interactions in Jupiter's magnetosphere. *Journal of Geophysical Research: Space Physics*, 109(A9). Retrieved from <https://agupubs.onlinelibrary.wiley.com/doi/abs/10.1029/2003JA010270> doi: 10.1029/2003JA010270
- McEwen, A. S. (1986). Exogenic and endogenic albedo and color patterns on Europa. *Journal of Geophysical Research: Solid Earth*, 91(B8), 8077-8097. Retrieved from <https://agupubs.onlinelibrary.wiley.com/doi/abs/10.1029/JB091iB08p08077> doi: <https://doi.org/10.1029/JB091iB08p08077>
- Müller, J., Simon, S., Motschmann, U., Schüle, J., Glassmeier, K.-H., & Pringle, G. J. (2011, Academic Press). A.I.K.E.F.: Adaptive hybrid model for space plasma simulations. *Computer Physics Communications*, 182(4), 946-966. doi: 10.1016/j.cpc.2010.12.033
- Néron, Q., & André, N. (2019). Evidence of Europa Neutral Gas Torii From Energetic Sulfur Ion Measurements. *Geophysical Research Letters*, 46(7), 3599-3606. Retrieved from <https://agupubs.onlinelibrary.wiley.com/doi/abs/>

- 2074 10.1029/2019GL082200 doi: 10.1029/2019GL082200
- 2075 Neubauer, F. M. (1980). Nonlinear standing Alfvén wave current system at Io - The-  
 2076 ory. *J. Geophys. Res.*, *85*, 1171–1178. doi: 10.1029/JA085iA03p01171
- 2077 Neubauer, F. M. (1998). The sub-Alfvénic interaction of the Galilean satellites with  
 2078 the Jovian magnetosphere. *J. Geophys. Res.*, *103*, 19843–19866. doi: 10.1029/  
 2079 97JE03370
- 2080 Neubauer, F. M. (1999). Alfvén wings and electromagnetic induction in the inte-  
 2081 riors: Europa and Callisto. *Journal of Geophysical Research (Space Physics)*,  
 2082 *104*, 28671–28684. doi: 10.1029/1999JA900217
- 2083 Nordheim, T. A., Hand, K. P., & Paranicas, C. (2018, July). Preservation of poten-  
 2084 tial biosignatures in the shallow subsurface of Europa. *Nature Astronomy*, *2*,  
 2085 673-679. doi: 10.1038/s41550-018-0499-8
- 2086 Nordheim, T. A., Jasinski, J. M., & Hand, K. P. (2019, aug). Galactic Cosmic-Ray  
 2087 Bombardment of Europa’s Surface. *The Astrophysical Journal*, *881*(2), L29.  
 2088 Retrieved from <https://doi.org/10.3847/2041-8213/ab3661> doi: 10.3847/  
 2089 2041-8213/ab3661
- 2090 Oza, A. V., Leblanc, F., Johnson, R. E., Schmidt, C., Leclercq, L., Cassidy, T. A.,  
 2091 & Chaufray, J.-Y. (2019, March). Dusk over dawn O<sub>2</sub> asymmetry in Eu-  
 2092 ropa’s near-surface atmosphere. *Planetary and Space Science*, *167*, 23-32. doi:  
 2093 10.1016/j.pss.2019.01.006
- 2094 Paganini, L., Villanueva, G. L., Roth, L., Mandell, A. M., Hurford, T. A., Rether-  
 2095 ford, K. D., & Mumma, M. J. (2020, January). A measurement of water  
 2096 vapour amid a largely quiescent environment on Europa. *Nature Astronomy*,  
 2097 *4*, 266-272. doi: 10.1038/s41550-019-0933-6
- 2098 Paranicas, C., Carlson, R. W., & Johnson, R. E. (2001). Electron bombard-  
 2099 ment of Europa. *Geophysical Research Letters*, *28*(4), 673-676. Retrieved  
 2100 from [https://agupubs.onlinelibrary.wiley.com/doi/abs/10.1029/](https://agupubs.onlinelibrary.wiley.com/doi/abs/10.1029/2000GL012320)  
 2101 [2000GL012320](https://agupubs.onlinelibrary.wiley.com/doi/abs/10.1029/2000GL012320) doi: 10.1029/2000GL012320
- 2102 Paranicas, C., Cooper, J. F., Garrett, H. B., Johnson, R. E., & Sturmer, S. J. (2009).  
 2103 Europa’s Radiation Environment and Its Effects on the Surface. In R. T. Pap-  
 2104 palardo, W. B. McKinnon, & K. K. Khurana (Eds.), *Europa* (p. 529).
- 2105 Paranicas, C., Mauk, B. H., Khurana, K., Jun, I., Garrett, H., Krupp, N., & Rous-  
 2106 sos, E. (2007). Europa’s near-surface radiation environment. *Geophysical*

- 2107 *Research Letters*, 34(15). Retrieved from <https://agupubs.onlinelibrary>  
2108 [.wiley.com/doi/abs/10.1029/2007GL030834](https://doi.org/10.1029/2007GL030834) doi: [https://doi.org/10.1029/](https://doi.org/10.1029/2007GL030834)  
2109 2007GL030834
- 2110 Paranicas, C., McEntire, R. W., Cheng, A. F., Lagg, A., & Williams, D. J. (2000).  
2111 Energetic charged particles near Europa. *Journal of Geophysical Re-*  
2112 *search: Space Physics*, 105(A7), 16005-16015. Retrieved from [https://](https://agupubs.onlinelibrary.wiley.com/doi/abs/10.1029/1999JA000350)  
2113 [agupubs.onlinelibrary.wiley.com/doi/abs/10.1029/1999JA000350](https://agupubs.onlinelibrary.wiley.com/doi/abs/10.1029/1999JA000350) doi:  
2114 10.1029/1999JA000350
- 2115 Paranicas, C., Ratliff, J. M., Mauk, B. H., Cohen, C., & Johnson, R. E. (2002).  
2116 The ion environment near Europa and its role in surface energetics. *Geo-*  
2117 *physical Research Letters*, 29(5), 18-1-18-4. Retrieved from [https://](https://agupubs.onlinelibrary.wiley.com/doi/abs/10.1029/2001GL014127)  
2118 [agupubs.onlinelibrary.wiley.com/doi/abs/10.1029/2001GL014127](https://agupubs.onlinelibrary.wiley.com/doi/abs/10.1029/2001GL014127) doi:  
2119 10.1029/2001GL014127
- 2120 Paterson, W. R., Frank, L. A., & Ackerson, K. L. (1999). Galileo plasma obser-  
2121 vations at Europa: Ion energy spectra and moments. *Journal of Geophysical*  
2122 *Research: Space Physics*, 104(A10), 22779-22791. Retrieved from [https://](https://agupubs.onlinelibrary.wiley.com/doi/abs/10.1029/1999JA900191)  
2123 [agupubs.onlinelibrary.wiley.com/doi/abs/10.1029/1999JA900191](https://agupubs.onlinelibrary.wiley.com/doi/abs/10.1029/1999JA900191) doi:  
2124 10.1029/1999JA900191
- 2125 Pensionerov, I. A., Alexeev, I. I., Belenkaya, E. S., Connerney, J. E. P., & Cowley,  
2126 S. W. H. (2019). Model of Jupiter's Current Sheet With a Piecewise Current  
2127 Density. *Journal of Geophysical Research: Space Physics*, 124(3), 1843-1854.  
2128 Retrieved from [https://agupubs.onlinelibrary.wiley.com/doi/abs/](https://agupubs.onlinelibrary.wiley.com/doi/abs/10.1029/2018JA026321)  
2129 [10.1029/2018JA026321](https://agupubs.onlinelibrary.wiley.com/doi/abs/10.1029/2018JA026321) doi: <https://doi.org/10.1029/2018JA026321>
- 2130 Petrik, N. G., Kavetsky, A. G., & Kimmel, G. A. (2006, September). Electron-  
2131 stimulated production of molecular oxygen in amorphous solid water on  
2132 Pt(111): Precursor transport through the hydrogen bonding network. *Journal*  
2133 *of Chemical Physics*, 125(12), 124702-124702. doi: 10.1063/1.2345367
- 2134 Plainaki, C., Cassidy, T. A., Shematovich, V. I., Milillo, A., Wurz, P., Vorburger,  
2135 A., ... Teolis, B. (2018, February). Towards a Global Unified Model of  
2136 Europa's Tenuous Atmosphere. *Space Science Reviews*, 214(1), 40. doi:  
2137 10.1007/s11214-018-0469-6
- 2138 Plainaki, C., Milillo, A., Massetti, S., Mura, A., Jia, X., Orsini, S., ... Rispoli, R.  
2139 (2015). The H<sub>2</sub>O and O<sub>2</sub> exospheres of Ganymede: The result of a com-

- plex interaction between the jovian magnetospheric ions and the icy moon.  
*Icarus*, 245, 306 - 319. Retrieved from <http://www.sciencedirect.com/science/article/pii/S0019103514004801> doi: <https://doi.org/10.1016/j.icarus.2014.09.018>
- Plainaki, C., Milillo, A., Mura, A., Orsini, S., Massetti, S., & Cassidy, T. (2012, 04). The role of sputtering and radiolysis in the generation of Europa exosphere. *Icarus*, 218, 956-966. doi: 10.1016/j.icarus.2012.01.023
- Plainaki, C., Milillo, A., Mura, A., Saur, J., Orsini, S., & Massetti, S. (2013). Exospheric O<sub>2</sub> densities at Europa during different orbital phases. *Planetary and Space Science*, 88, 42 - 52. Retrieved from <http://www.sciencedirect.com/science/article/pii/S003206331300216X> (Atmospheres, Magnetospheres and Surfaces of the outer planets, their satellites and ring systems: Part IX) doi: <https://doi.org/10.1016/j.pss.2013.08.011>
- Pospieszalska, M., & Johnson, R. (1989). Magnetospheric ion bombardment profiles of satellites: Europa and Dione. *Icarus*, 78(1), 1 - 13. Retrieved from <http://www.sciencedirect.com/science/article/pii/0019103589900651> doi: [https://doi.org/10.1016/0019-1035\(89\)90065-1](https://doi.org/10.1016/0019-1035(89)90065-1)
- Rathbun, J. A., Rodriguez, N. J., & Spencer, J. R. (2010). Galileo PPR observations of Europa: Hotspot detection limits and surface thermal properties. *Icarus*, 210(2), 763-769. Retrieved from <https://www.sciencedirect.com/science/article/pii/S0019103510002897> doi: <https://doi.org/10.1016/j.icarus.2010.07.017>
- Regoli, L. H., Roussos, E., Feyerabend, M., Jones, G. H., Krupp, N., Coates, A. J., ... Dougherty, M. K. (2016). Access of energetic particles to Titan's exobase: A study of Cassini's T9 flyby. *Planet. Space Sci.*, 130, 40-53. doi: 10.1016/j.pss.2015.11.013
- Roth, L. (2021). A Stable H<sub>2</sub>O Atmosphere on Europa's Trailing Hemisphere From HST Images. *Geophysical Research Letters*, 48(20), e2021GL094289. Retrieved from <https://agupubs.onlinelibrary.wiley.com/doi/abs/10.1029/2021GL094289> (e2021GL094289 2021GL094289) doi: <https://doi.org/10.1029/2021GL094289>
- Roth, L., Retherford, K. D., Ivchenko, N., Schlatter, N., Strobel, D. F., Becker, T. M., & Grava, C. (2017, February). Detection of a Hydrogen Corona in

- 2173 HST Ly $\alpha$  Images of Europa in Transit of Jupiter. *The Astrophysical Journal*,  
2174 153(2), 67. doi: 10.3847/1538-3881/153/2/67
- 2175 Roth, L., Retherford, K. D., Saur, J., Strobel, D. F., Feldman, P. D., McGrath,  
2176 M. A., & Nimmo, F. (2014). Orbital apocenter is not a sufficient con-  
2177 dition for HST/STIS detection of Europa’s water vapor aurora. *Pro-*  
2178 *ceedings of the National Academy of Sciences*, 111(48), E5123–E5132.  
2179 Retrieved from <https://www.pnas.org/content/111/48/E5123> doi:  
2180 10.1073/pnas.1416671111
- 2181 Roth, L., Saur, J., Retherford, K. D., Strobel, D. F., Feldman, P. D., McGrath,  
2182 M. A., ... Ivchenko, N. (2016). Europa’s far ultraviolet oxygen aurora  
2183 from a comprehensive set of HST observations. *Journal of Geophysical*  
2184 *Research: Space Physics*, 121(3), 2143–2170. Retrieved from [https://](https://agupubs.onlinelibrary.wiley.com/doi/abs/10.1002/2015JA022073)  
2185 [agupubs.onlinelibrary.wiley.com/doi/abs/10.1002/2015JA022073](https://agupubs.onlinelibrary.wiley.com/doi/abs/10.1002/2015JA022073) doi:  
2186 <https://doi.org/10.1002/2015JA022073>
- 2187 Rubin, M., Jia, X., Altwegg, K., Combi, M. R., Daldorff, L. K. S., Gombosi, T. I.,  
2188 ... Wurz, P. (2015). Self-consistent multifluid MHD simulations of Europa’s  
2189 exospheric interaction with Jupiter’s magnetosphere. *Journal of Geophysi-*  
2190 *cal Research: Space Physics*, 120(5), 3503–3524. Retrieved from [https://](https://agupubs.onlinelibrary.wiley.com/doi/abs/10.1002/2015JA021149)  
2191 [agupubs.onlinelibrary.wiley.com/doi/abs/10.1002/2015JA021149](https://agupubs.onlinelibrary.wiley.com/doi/abs/10.1002/2015JA021149) doi:  
2192 10.1002/2015JA021149
- 2193 Saur, J., Feldman, P., Roth, L., Nimmo, F., Strobel, D., Retherford, K., ... Gro-  
2194 dent, D. (2011, 09). Hubble Space Telescope/Advanced Camera for Surveys  
2195 Observations of Europa’s Atmospheric Ultraviolet Emission at Eastern Elonga-  
2196 tion. *apj*, 738, 153. doi: 10.1088/0004-637X/738/2/153
- 2197 Saur, J., Strobel, D. F., & Neubauer, F. M. (1998). Interaction of the Jovian magne-  
2198 tosphere with Europa: Constraints on the neutral atmosphere. *Journal of Geo-*  
2199 *physical Research: Planets*, 103(E9), 19947–19962. Retrieved from [https://](https://agupubs.onlinelibrary.wiley.com/doi/abs/10.1029/97JE03556)  
2200 [agupubs.onlinelibrary.wiley.com/doi/abs/10.1029/97JE03556](https://agupubs.onlinelibrary.wiley.com/doi/abs/10.1029/97JE03556) doi: 10  
2201 .1029/97JE03556
- 2202 Saur, J., Strobel, D. F., Neubauer, F. M., & Summers, M. E. (2003, June). The ion  
2203 mass loading rate at Io. *Icarus*, 163(2), 456–468. doi: 10.1016/S0019-1035(03)  
2204 00085-X
- 2205 Schenk, P. M., Chapman, C. R., Zahnle, K., & Moore, J. M. (2007). Ages and Inte-



- 2206 riors: the Cratering Record of the Galilean Satellites. In *Jupiter* (p. 427).
- 2207 Schilling, N., Neubauer, F. M., & Saur, J. (2007). Time-varying interaction  
2208 of Europa with the jovian magnetosphere: Constraints on the conductiv-  
2209 ity of Europa’s subsurface ocean. *Icarus*, 192(1), 41 - 55. Retrieved from  
2210 <http://www.sciencedirect.com/science/article/pii/S0019103507002837>  
2211 doi: <https://doi.org/10.1016/j.icarus.2007.06.024>
- 2212 Seufert, M., Saur, J., & Neubauer, F. M. (2011). Multi-frequency electromagnetic  
2213 sounding of the Galilean moons. *Icarus*, 214(2), 477–494. doi: 10.1016/j.icarus  
2214 .2011.03.017
- 2215 Shematovich, V. I., Johnson, R. E., Cooper, J. F., & Wong, M. C. (2005, February).  
2216 Surface-bounded atmosphere of Europa. *Icarus*, 173(2), 480-498. doi: 10.1016/  
2217 j.icarus.2004.08.013
- 2218 Sieger, M. T., Simpson, W. C., & Orlando, T. M. (1998, August). Production of O<sub>2</sub>  
2219 on icy satellites by electronic excitation of low-temperature water ice. *Nature*,  
2220 394(6693), 554-556. doi: 10.1038/29015
- 2221 Sigmund, P. (1969, Aug). Theory of Sputtering. I. Sputtering Yield of Amor-  
2222 phous and Polycrystalline Targets. *Phys. Rev.*, 184, 383–416. Retrieved  
2223 from <https://link.aps.org/doi/10.1103/PhysRev.184.383> doi:  
2224 10.1103/PhysRev.184.383
- 2225 Simon, S., Addison, P., & Liuzzo, L. (2022). Formation of a Displaced  
2226 Plasma Wake at Neptune’s Moon Triton. *Journal of Geophysical Re-*  
2227 *search: Space Physics*, 127(1), e2021JA029958. Retrieved from [https://](https://agupubs.onlinelibrary.wiley.com/doi/abs/10.1029/2021JA029958)  
2228 [agupubs.onlinelibrary.wiley.com/doi/abs/10.1029/2021JA029958](https://agupubs.onlinelibrary.wiley.com/doi/abs/10.1029/2021JA029958)  
2229 (e2021JA029958 2021JA029958) doi: <https://doi.org/10.1029/2021JA029958>
- 2230 Simon, S., Kriegel, H., Saur, J., Wennmacher, A., Neubauer, F. M., Roussos, E., ...  
2231 Dougherty, M. K. (2012). Analysis of Cassini magnetic field observations over  
2232 the poles of Rhea. *Journal of Geophysical Research: Space Physics*, 117(A7).  
2233 Retrieved from [https://agupubs.onlinelibrary.wiley.com/doi/abs/](https://agupubs.onlinelibrary.wiley.com/doi/abs/10.1029/2012JA017747)  
2234 [10.1029/2012JA017747](https://agupubs.onlinelibrary.wiley.com/doi/abs/10.1029/2012JA017747) doi: 10.1029/2012JA017747
- 2235 Simon, S., Liuzzo, L., & Addison, P. (2021). Role of the ionospheric conductance  
2236 profile in sub-alfvénic moon-magnetosphere interactions: An analytical model.  
2237 *Journal of Geophysical Research: Space Physics*, 126(7), e2021JA029191.  
2238 Retrieved from <https://agupubs.onlinelibrary.wiley.com/doi/abs/>

10.1029/2021JA029191 (e2021JA029191 2021JA029191) doi: <https://doi.org/10.1029/2021JA029191>

Simon, S., Saur, J., Neubauer, F., Motschmann, U., & Dougherty, M. (2009). Plasma wake of Tethys: Hybrid simulations versus Cassini MAG data. *Geophys. Res. Lett.*, *36*(4), L04108. doi: 10.1029/2008GL036943

Smith, H. T., Mitchell, D. G., Johnson, R. E., Mauk, B. H., & Smith, J. E. (2019, January). Europa Neutral Torus Confirmation and Characterization Based on Observations and Modeling. *The Astrophysical Journal*, *871*(1), 69. doi: 10.3847/1538-4357/aaed38

Smyth, W. H., & Marconi, M. L. (2006, Academic Press). Europa's atmosphere, gas tori, and magnetospheric implications. *Icarus*, *181*(2), 510-526. doi: 10.1016/j.icarus.2005.10.019

Spencer, J. R., Lebofsky, L. A., & Sykes, M. V. (1989). Systematic biases in radiometric diameter determinations. *Icarus*, *78*(2), 337-354. Retrieved from <https://www.sciencedirect.com/science/article/pii/0019103589901826> doi: [https://doi.org/10.1016/0019-1035\(89\)90182-6](https://doi.org/10.1016/0019-1035(89)90182-6)

Spencer, J. R., Tamppari, L. K., Martin, T. Z., & Travis, L. D. (1999, May). Temperatures on Europa from Galileo Photopolarimeter-Radiometer: Nighttime Thermal Anomalies. *Science*, *284*, 1514. doi: 10.1126/science.284.5419.1514

Teolis, B. D., Jones, G. H., Miles, P. F., Tokar, R. L., Magee, B. A., Waite, J. H., ... Baragiola, R. A. (2010). Cassini Finds an Oxygen-Carbon Dioxide Atmosphere at Saturn's Icy Moon Rhea. *Science*, *330*(6012), 1813-1815. doi: 10.1126/science.1198366

Teolis, B. D., Plainaki, C., Cassidy, T. A., & Raut, U. (2017). Water Ice Radiolytic O<sub>2</sub>, H<sub>2</sub>, and H<sub>2</sub>O<sub>2</sub> Yields for Any Projectile Species, Energy, or Temperature: A Model for Icy Astrophysical Bodies. *Journal of Geophysical Research: Planets*, *122*(10), 1996-2012. Retrieved from <https://agupubs.onlinelibrary.wiley.com/doi/abs/10.1002/2017JE005285> doi: <https://doi.org/10.1002/2017JE005285>

Teolis, B. D., Shi, J., & Baragiola, R. A. (2009, Academic Press). Formation, trapping, and ejection of radiolytic O<sub>2</sub> from ion-irradiated water ice studied by sputter depth profiling. *Journal of Chemical Physics*, *130*(13), 134704-134704. doi: 10.1063/1.3091998

- 2272 Teolis, B. D., Vidal, R. A., Shi, J., & Baragiola, R. A. (2005, December). Mecha-  
2273 nisms of O<sub>2</sub> sputtering from water ice by keV ions. *Physical Review B*, 72(24),  
2274 245422. doi: 10.1103/PhysRevB.72.245422
- 2275 Vance, S., Styczinski, M. J., Bills, B. G., Cochrane, C. J., Soderlund, K. M.,  
2276 Gómez-Pérez, N., & Paty, C. (2021, February). Magnetic Induction Re-  
2277 sponses of Jupiter’s Ocean Moons Including Effects From Adiabatic Con-  
2278 vection. *Journal of Geophysical Research (Planets)*, 126(2), e06418. doi:  
2279 10.1029/2020JE006418
- 2280 Vidal, R., Teolis, B., & Baragiola, R. (2005). Angular dependence of the sputtering  
2281 yield of water ice by 100keV proton bombardment. *Surface Science*, 588(1), 1-  
2282 5. Retrieved from [https://www.sciencedirect.com/science/article/pii/](https://www.sciencedirect.com/science/article/pii/S003960280500498X)  
2283 [S003960280500498X](https://www.sciencedirect.com/science/article/pii/S003960280500498X) doi: <https://doi.org/10.1016/j.susc.2005.05.007>
- 2284 Vorburger, A., & Wurz, P. (2018, September). Europa’s ice-related atmosphere: The  
2285 sputter contribution. *Icarus*, 311, 135-145. doi: 10.1016/j.icarus.2018.03.022
- 2286 Wiehle, S., Plaschke, F., Motschmann, U., Glassmeier, K.-H., Auster, H., An-  
2287 gelopoulos, V., ... McFadden, J. (2011). First lunar wake passage of  
2288 ARTEMIS: Discrimination of wake effects and solar wind fluctuations by  
2289 3D hybrid simulations. *Planetary and Space Science*, 59(8), 661-671. Re-  
2290 trieved from [https://www.sciencedirect.com/science/article/pii/](https://www.sciencedirect.com/science/article/pii/S0032063311000407)  
2291 [S0032063311000407](https://www.sciencedirect.com/science/article/pii/S0032063311000407) doi: <https://doi.org/10.1016/j.pss.2011.01.012>
- 2292 Ziegler, J., & Manoyan, J. (1988). The stopping of ions in compounds. *Nu-*  
2293 *clear Instruments and Methods in Physics Research Section B: Beam In-*  
2294 *teractions with Materials and Atoms*, 35(3), 215-228. Retrieved from  
2295 <https://www.sciencedirect.com/science/article/pii/0168583X8890273X>  
2296 doi: [https://doi.org/10.1016/0168-583X\(88\)90273-X](https://doi.org/10.1016/0168-583X(88)90273-X)
- 2297 Zimmer, C., Khurana, K. K., & Kivelson, M. G. (2000). Subsurface Oceans on  
2298 Europa and Callisto: Constraints from Galileo Magnetometer Observations.  
2299 *Icarus*, 147(2), 329-347. doi: 10.1006/icar.2000.6456

Figure 1.

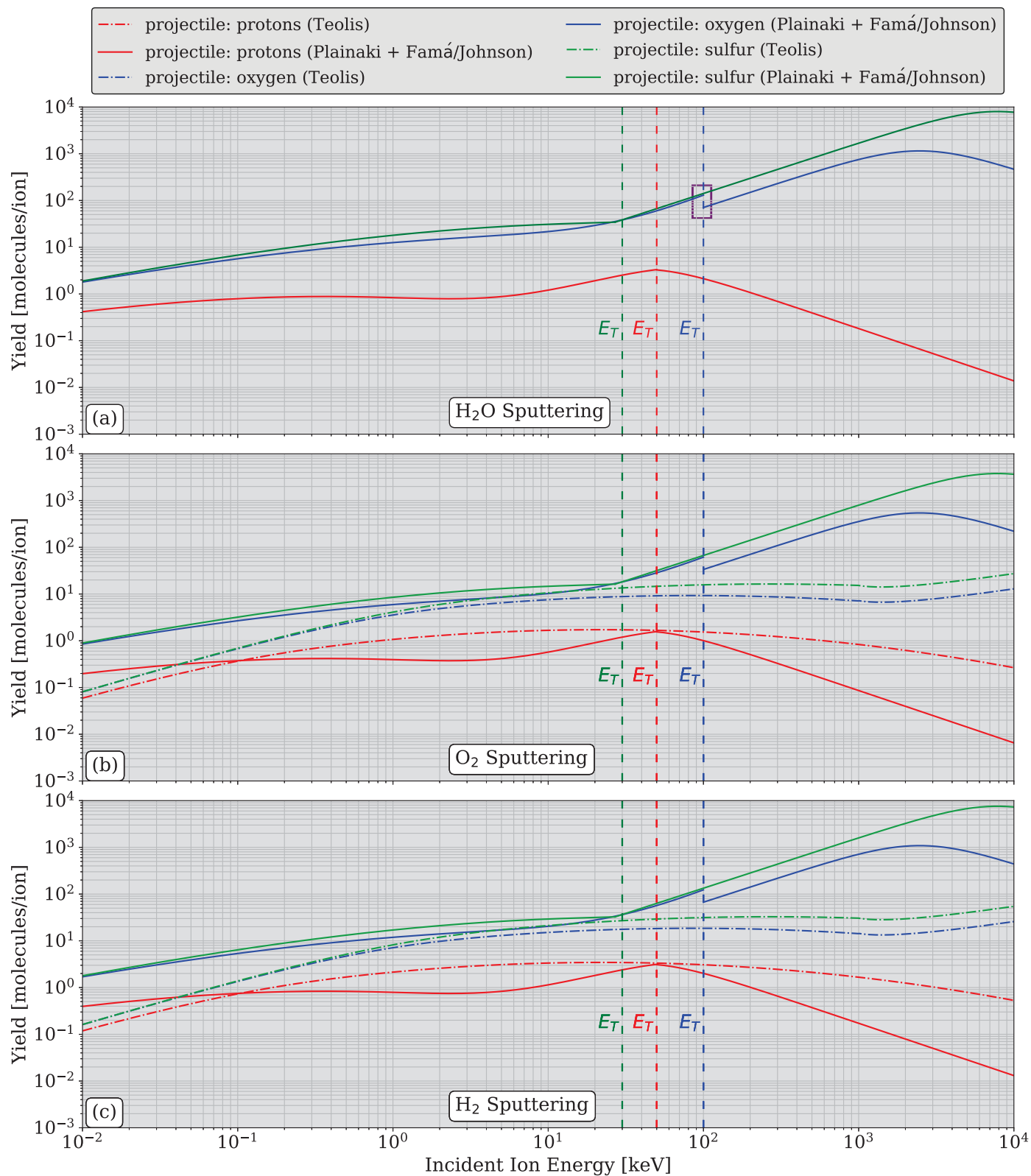


Figure 2.

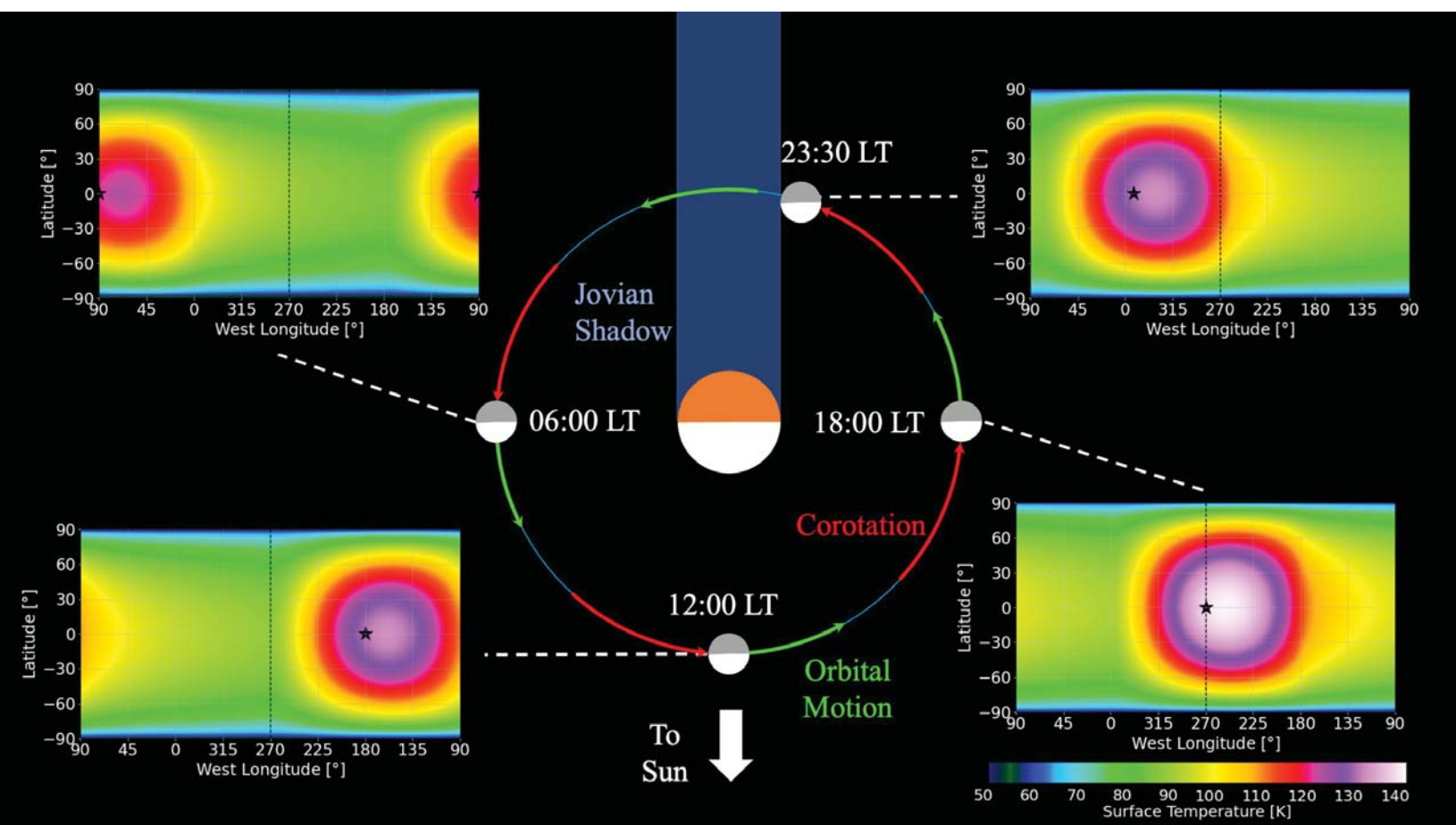


Figure 3.



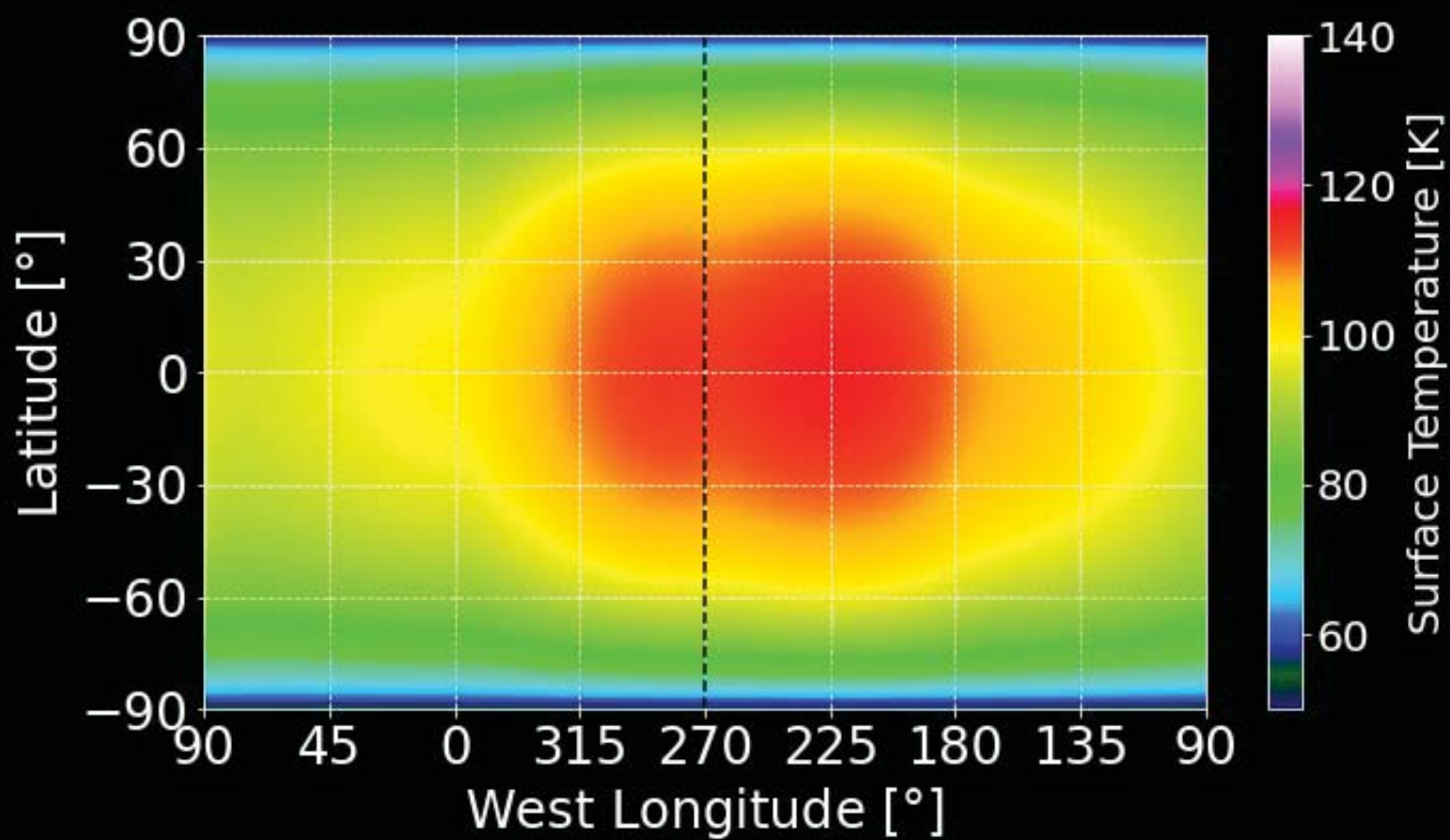


Figure 4.

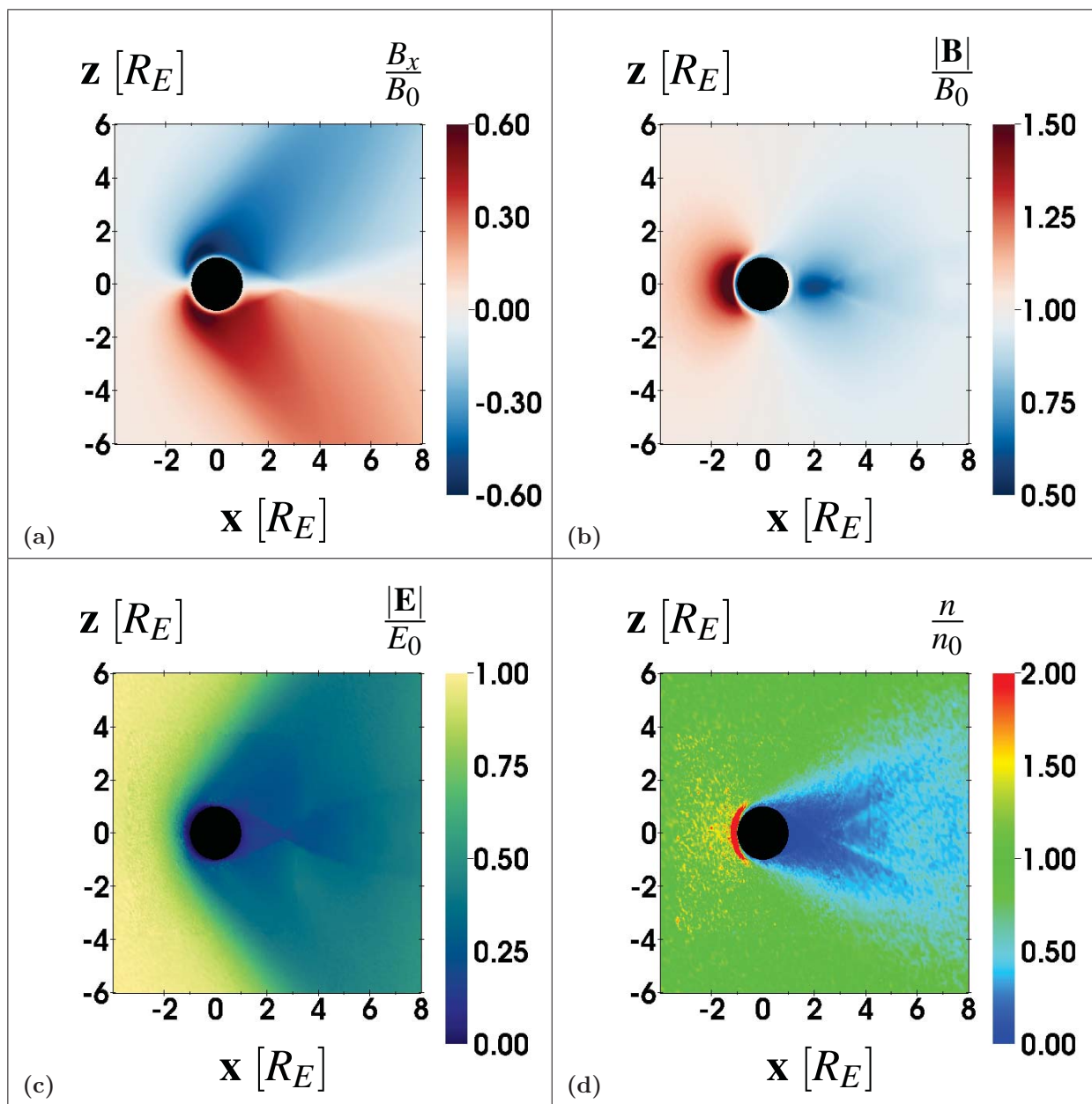


Figure 5.

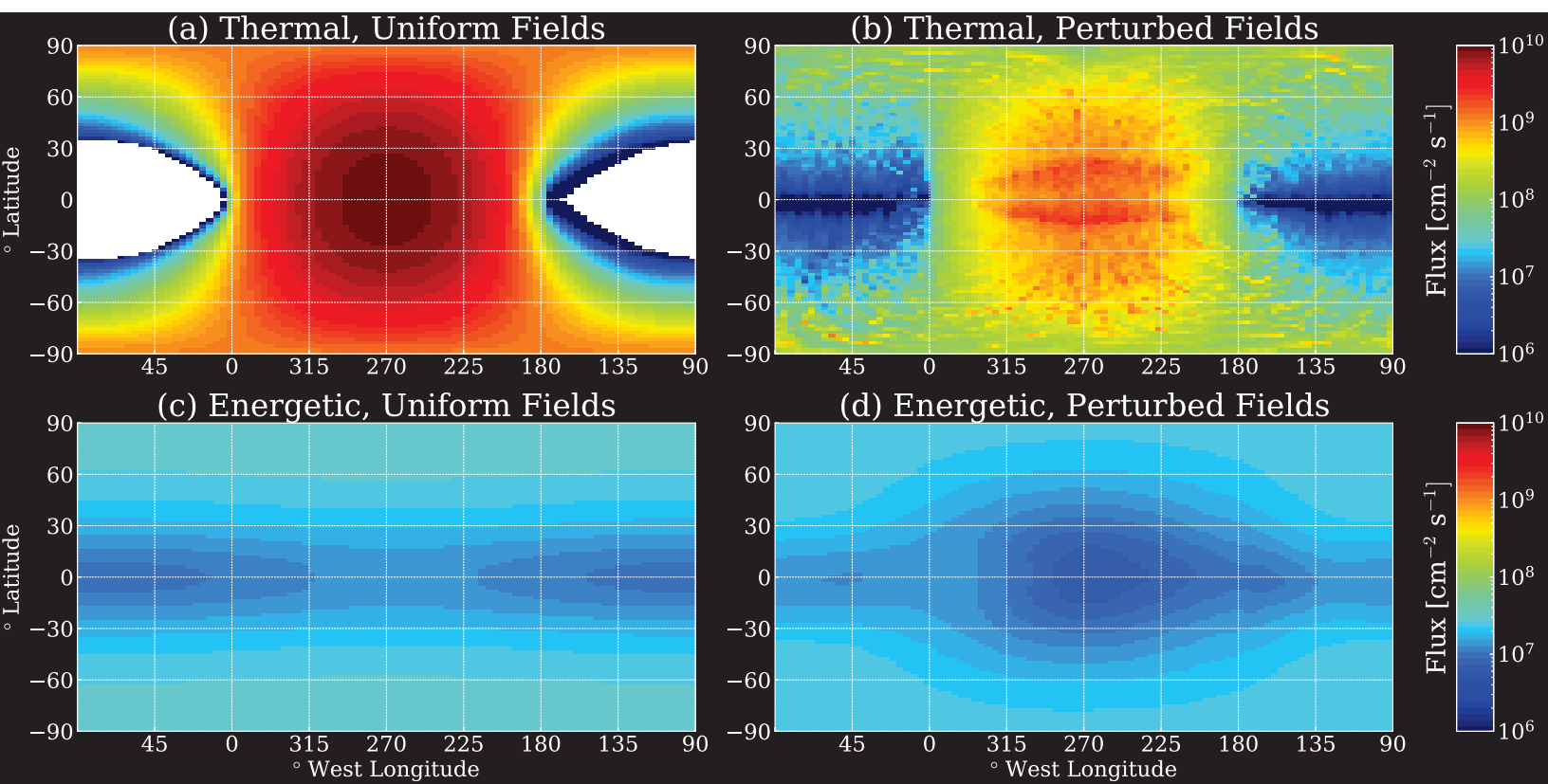


Figure 6.

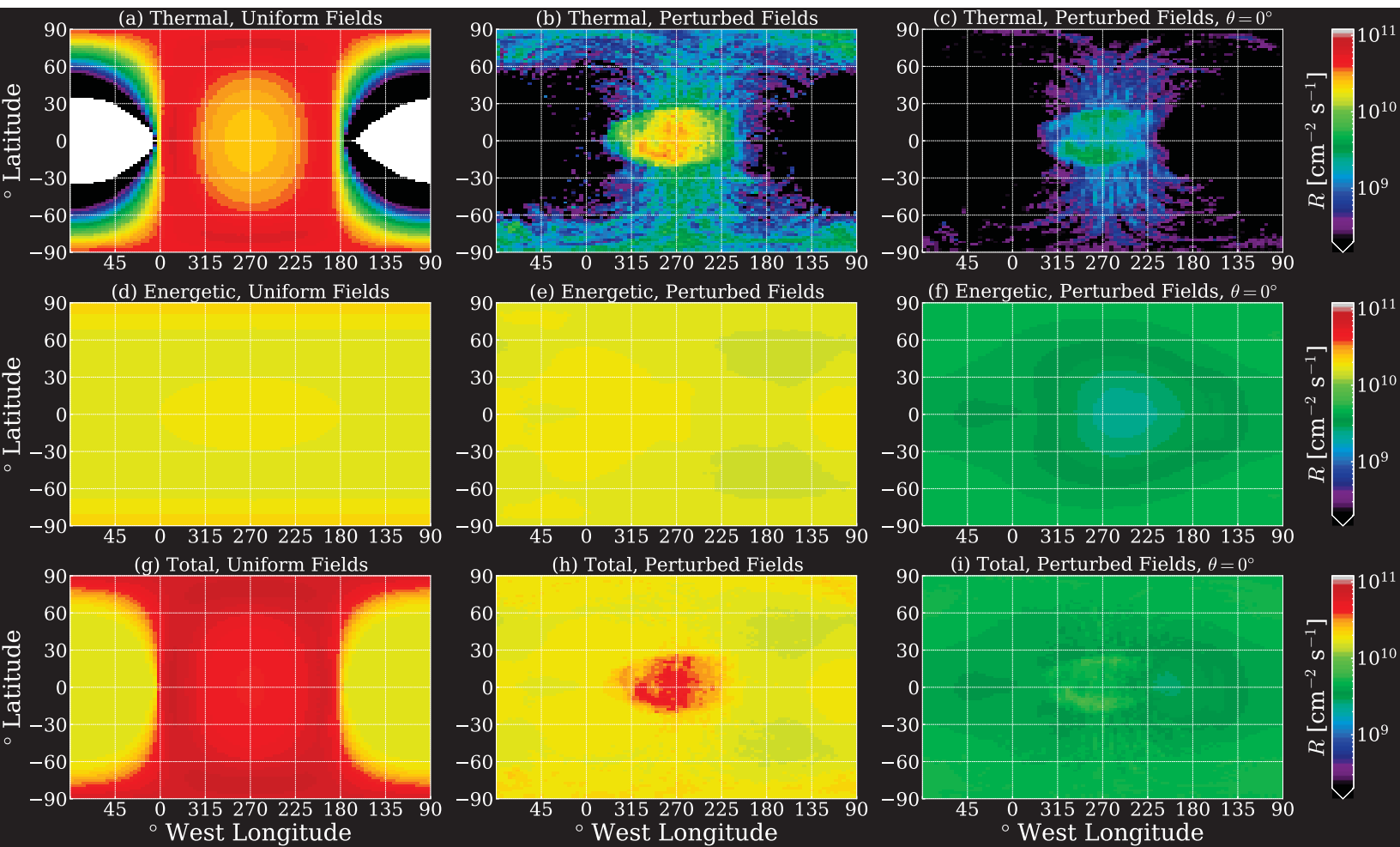


Figure 7.



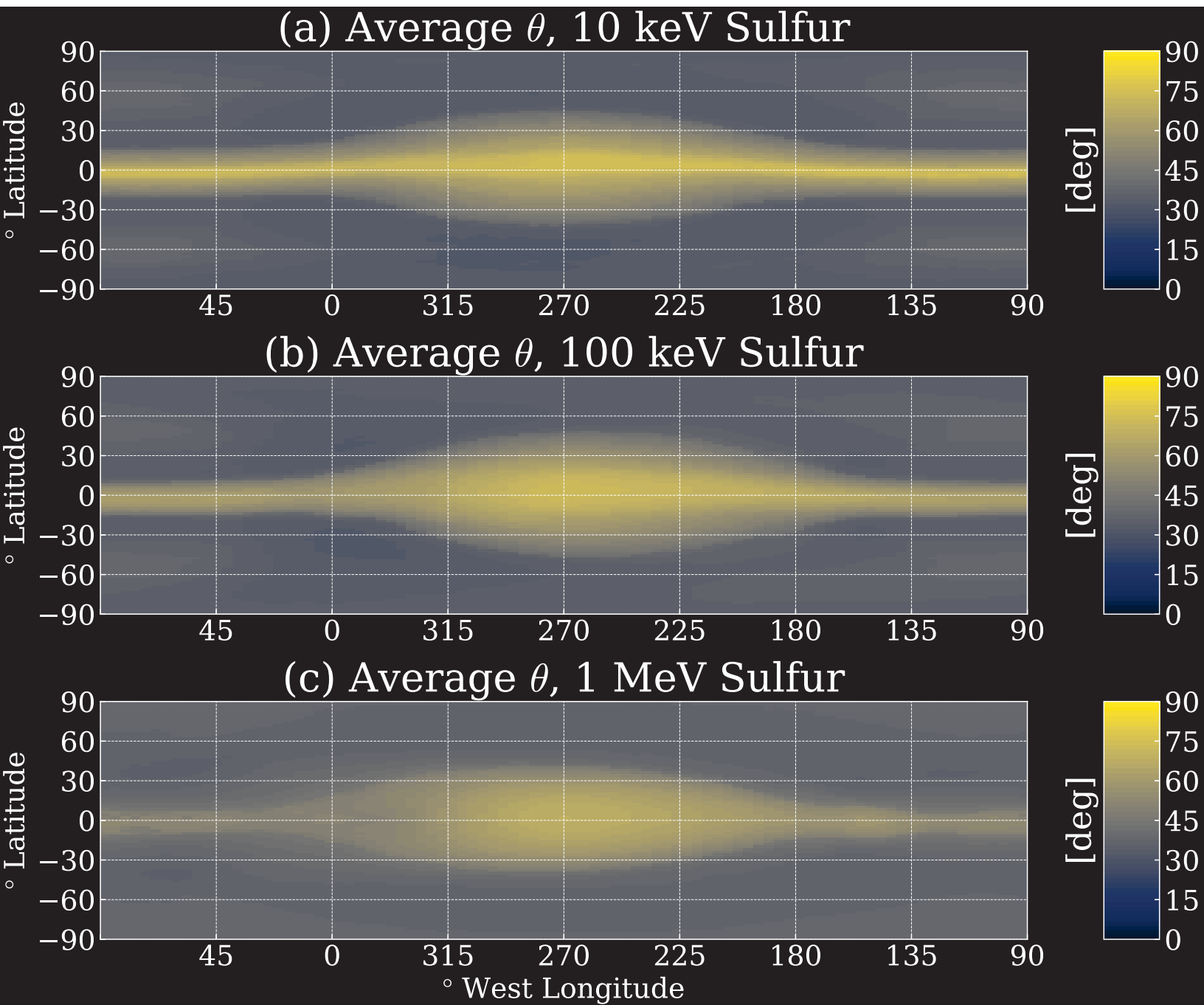


Figure 8.

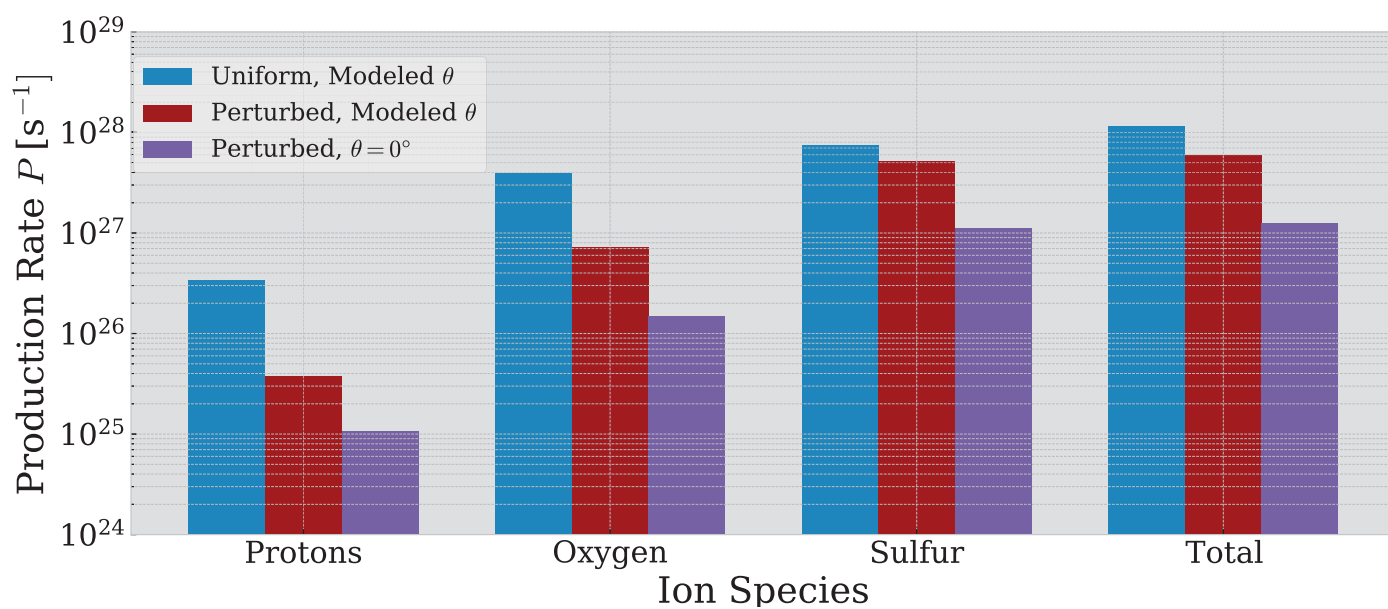


Figure 9.

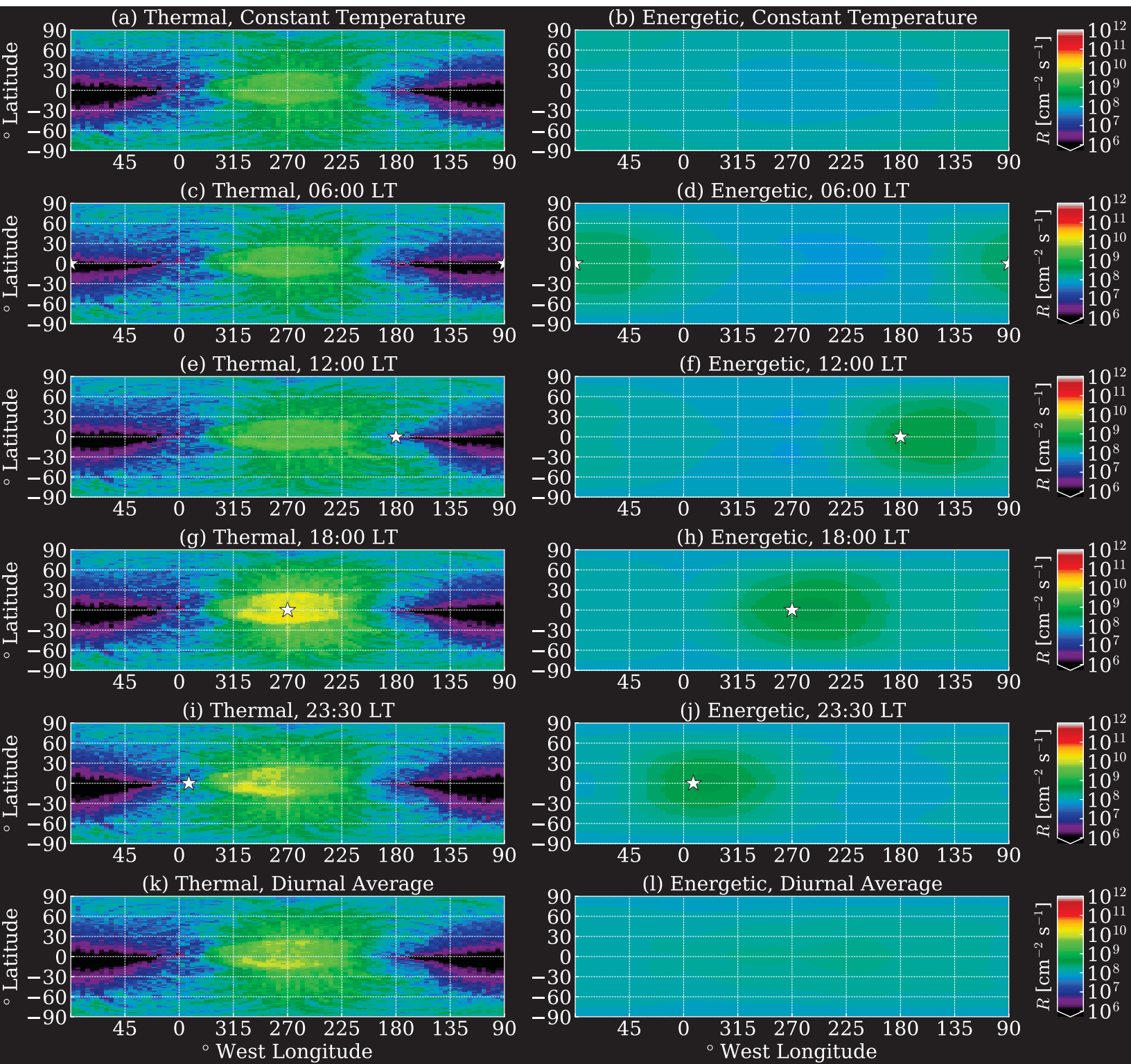


Figure 10.

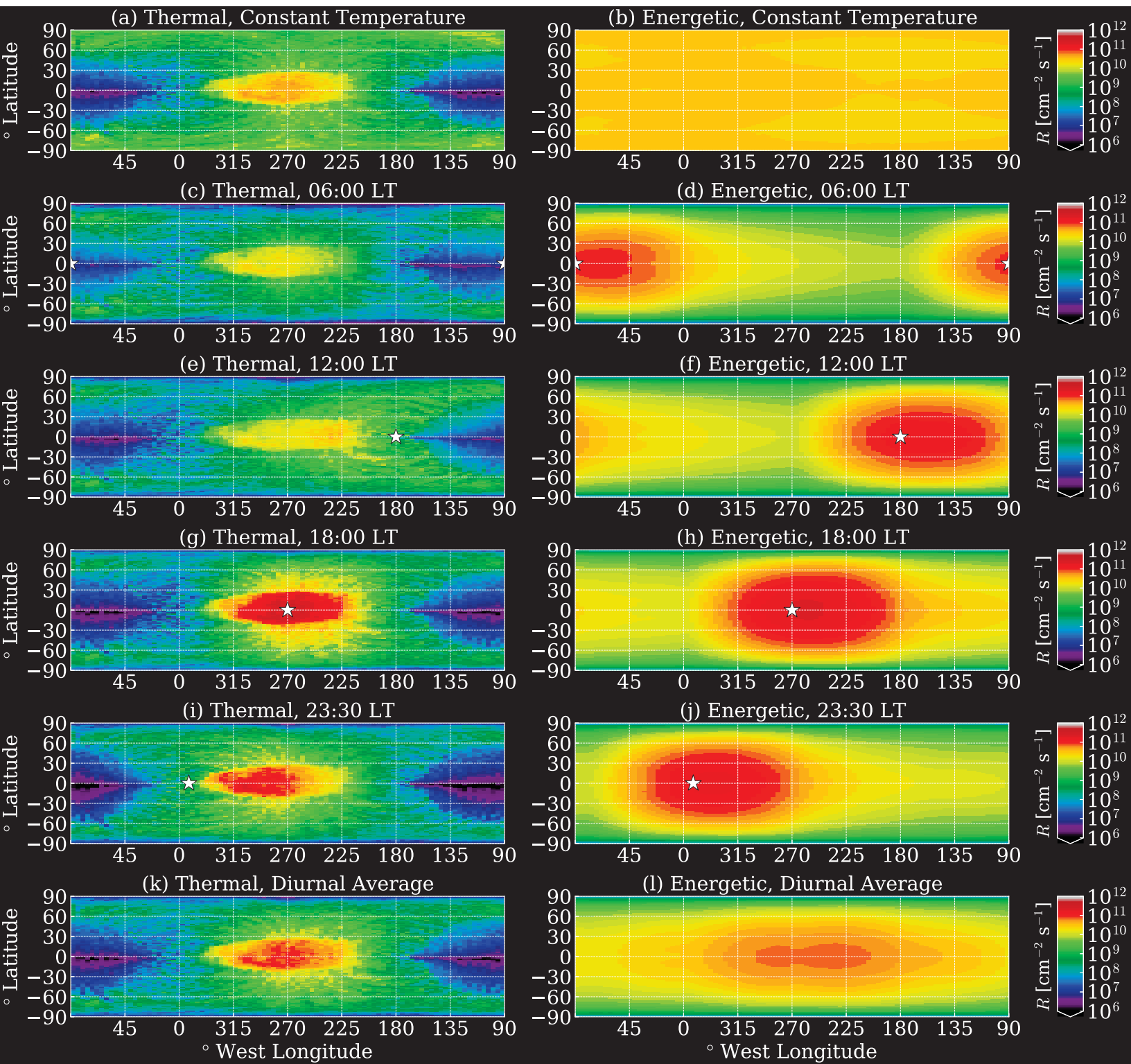


Figure 11.



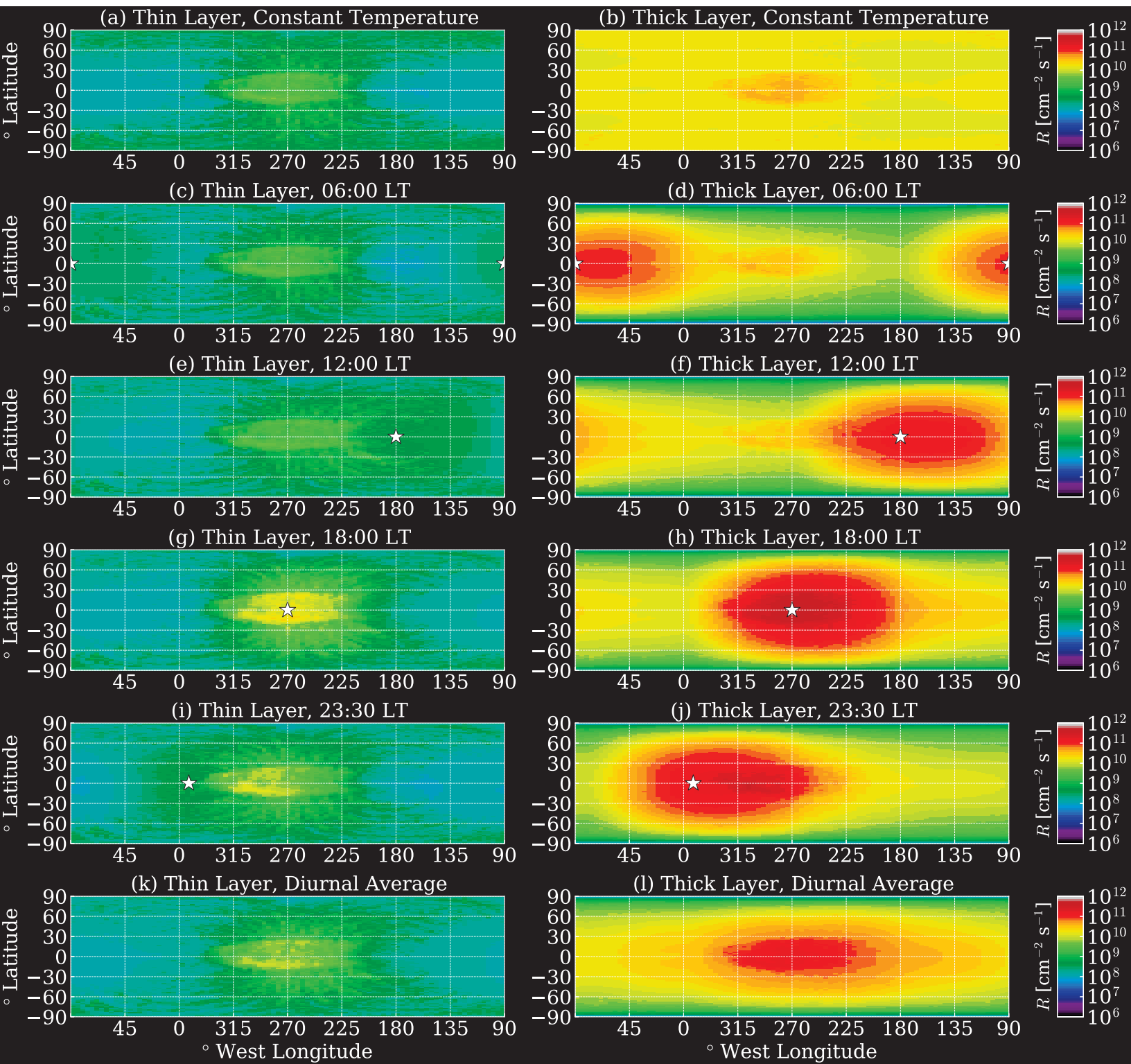
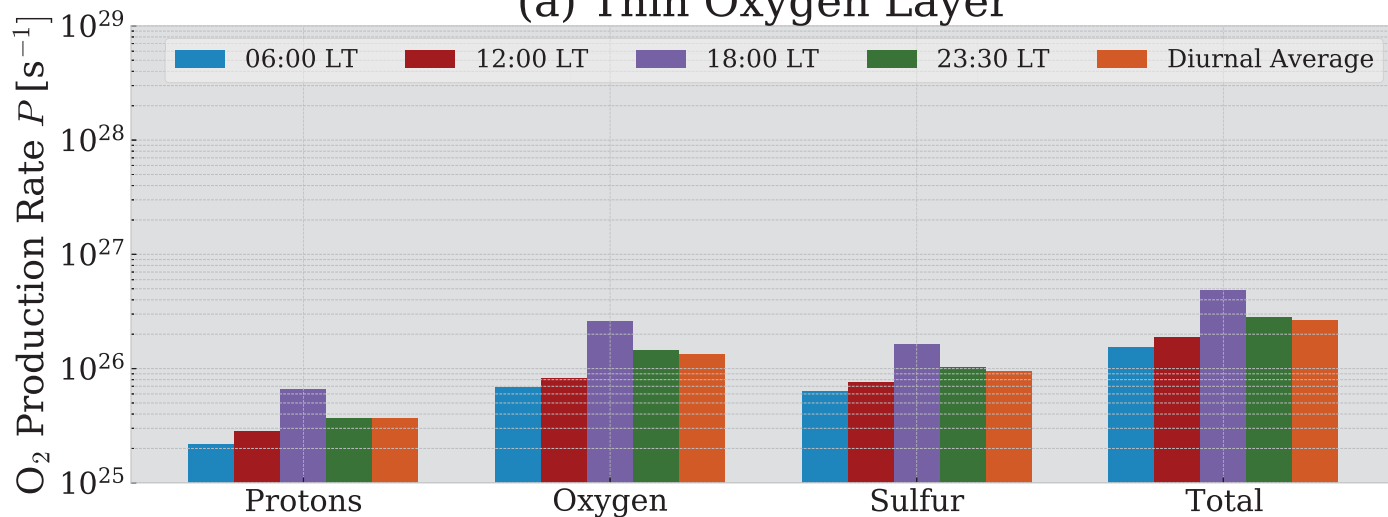


Figure 12.

(a) Thin Oxygen Layer



(b) Thick Oxygen Layer

